POLITECNICO DI TORINO

Collegio di Ingegneria Chimica e dei Materiali

Corso di Laurea Magistrale
in Ingegneria Chimica e dei Processi Sostenibili

Tesi di Laurea Magistrale

Lignin-based composite polymer electrolytes for potassium batteries

Supervisori
Prof. Federico Bella
Dott.ssa Sabrina Trano

Candidata
Giorgia Morone

Marzo 2022

Sommario

La richiesta energetica globale è in continuo aumento, e con essa lo sfruttamento dei combustibili fossili: l'inquinamento che deriva dalla combustione di questi ultimi sta causando intensi cambiamenti climatici e danni all'ambiente. La transizione verso fonti energetiche rinnovabili è fortemente necessaria per evitare scenari peggiori, ma presenta alcuni limiti, legati all'intrinseca intermittenza e imprevedibilità delle suddette fonti. Una promettente soluzione è rappresentata dall'utilizzo di sistemi di stoccaggio energetico (ESS), che permettono di immagazzinare l'energia nei momenti di massima produttività e di renderla disponibile in seguito.

Le batterie, le cui unità fondamentali sono le celle elettrochimiche (ElC), permettono di accumulare energia sotto forma chimica e di rilasciarla trasformandola in energia elettrica, tramite l'avvenimento di reazioni di ossidoriduzione. La singola ElC è composta da due elettrodi: all'anodo ha luogo la reazione di ossidazione, mentre al catodo avviene quella di riduzione. Il terzo componente fondamentale è l'elettrolita, che consente il trasporto di ioni negativi e positivi tra gli elettrodi e impedisce il passaggio di elettroni, il quale causerebbe il cortocircuito della cella. Una batteria o ElC è definita secondaria se può effettuare molti cicli di carica e scarica, comportandosi alternativamente come cella galvanica e come cella elettrolitica. Una cella galvanica [Figura 1] converte energia chimica in energia elettrica: in questa configurazione, l'anodo costituisce l'elettrodo negativo e il catodo quello positivo. Gli elettroni rilasciati all'anodo fluiscono verso il catodo attraverso il circuito esterno: ciò corrisponde alla fase di scarica di una batteria secondaria. Al contrario, la cella elettrolitica [Figura 1] rappresenta la fase di carica, durante la quale viene applicata una corrente esterna e gli elettroni si muovono verso l'elettrodo negativo. In questo caso, l'anodo è l'elettrodo positivo, mentre il catodo è negativo.
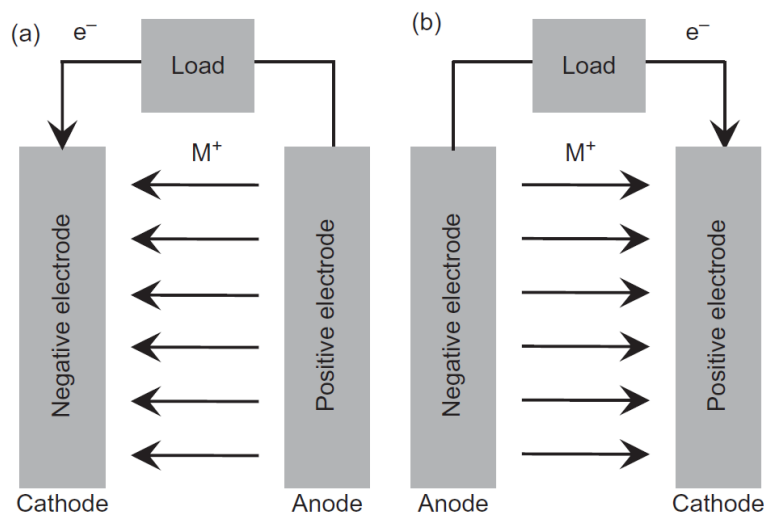

Figura 1: a) Cella elettrolitica, b) cella galvanica.

Tra i sistemi elettrochimici di stoccaggio energetico, le batterie litio-ione (LIB) rappresentano la tecnologia più studiata e utilizzata; grazie a numerosi aspetti positivi, queste batterie sono impiegate in molte applicazioni, quali i dispositivi elettronici portatili e i veicoli elettrici. A causa dell'elevato costo del litio, che costituisce solamente lo 0.0017% in peso della crosta terrestre e che presenta una disomogenea distribuzione su scala mondiale, è necessaria la ricerca di metalli alternativi: il più promettente candidato è il potassio. Questo metallo alcalino è molto più abbondante, costituendo l'1.5% in peso della crosta terrestre, e uniformemente distribuito; inoltre, permette di ottenere prestazioni non lontane da quelle del litio, possedendo un potenziale standard di riduzione di -2.93 V vs. SHE (litio: -3.04 V vs. SHE). Un ulteriore aspetto positivo è rappresentato dal minore raggio di Stokes del potassio, che permette di ottenere un trasporto ionico più rapido.

Le KIB, così come le LIB, sono batterie secondarie che si basano sul principio denominato "*rocking chair*" [Figura 2], secondo cui i cationi si spostano ripetutamente tra anodo e catodo, attraverso l'elettrolita, mentre gli elettroni fluiscono nel circuito esterno.
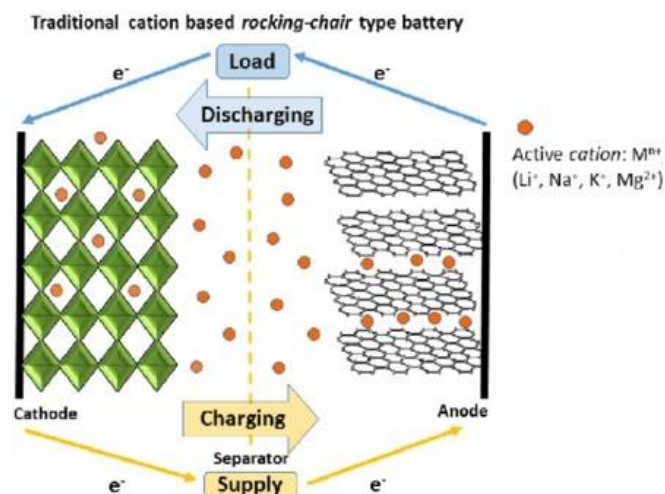

Figura 2: Rappresentazione schematica del principio "*rocking chair*".

Durante il processo di scarica, gli ioni K^+ sono rimossi dall'anodo, che ospita la reazione di ossidazione, e inseriti nel catodo, dove si combinano con gli elettroni provenienti dal circuito esterno con la reazione di riduzione. Il processo di carica è opposto: gli ioni K^+ si spostano dall'elettrodo positivo a quello negativo, a causa dell'applicazione di una corrente elettrica esterna.

I materiali anodici tipicamente utilizzati nelle KIB sono classificati in base alla tipologia di inserimento degli ioni K^+ e comprendono materiali a intercalazione, materiali a conversione, leghe e composti organici. Nei materiali catodici, gli ioni K^+ sono sottoposti solamente a intercalazione; essi comprendono ossidi di metalli di transizione a strati (TMO), esacianoferrati metallici (Blu di Prussia e materiali analoghi), composti polianionici e composti organici.

Gli elettroliti utilizzati nelle KIB sono classificati in due categorie principali: liquidi e solidi. Gli elettroliti liquidi possono essere ulteriormente suddivisi in acquosi, organici e ionici (IL), mentre gli elettroliti allo stato solido (SSE) includono i solidi inorganici e i solidi polimerici.

Generalmente, un elettrolita liquido è formato da un sale o da un insieme di sali, disciolti in uno o più solventi. I IL sono costituiti da una miscela di anioni inorganici o organici e cationi organici, che presentano forma liquida a temperatura ambiente; questi elettroliti sono caratterizzati da un'ampia finestra di stabilità elettrochimica (ESW) e da elevata stabilità termica, ma l'ingente costo e l'alta viscosità ne limitano l'impiego. Gli elettroliti organici sono composti da un sale, come KPF_6, $KClO_4$ o KBF_4, disciolto in uno o più solventi, quali etilene carbonato (EC), propilene carbonato (PC), dietilcarbonato (DEC), e molti altri. Questi elettroliti presentano molte caratteristiche positive, quali elevata conducibilità ionica, basso costo, bassa viscosità, ampia ESW e capacità di formare interfacce solide elettrodo/elettrolita (SEI *layer*) omogenee e stabili. Tuttavia, gli elettroliti organici sono caratterizzati da elevata infiammabilità e reattività nei confronti del potassio, pertanto non garantiscono un'adeguata sicurezza della KIB. I sali solitamente presenti negli elettroliti acquosi includono KNO_3, K_2SO_4, KCl e KOH; questi elettroliti liquidi possiedono elevata conducibilità ionica, basso costo e compatibilità ambientale, ma la ESW molto ristretta (0 - 1.23 V) ne limita fortemente le applicazioni.

L'utilizzo degli elettroliti liquidi nelle KIB è ostacolato dai problemi precedentemente elencati, perciò la ricerca si sta indirizzando verso gli SSE, che presentano molti aspetti positivi. Essi sono caratterizzati da non infiammabilità, stabilità termica e meccanica e compatibilità ambientale; inoltre, possono sopprimere la formazione dei dendriti, mostrano un'ampia ESW e inibiscono la dissoluzione degli elettrodi organici. Queste caratteristiche aumentano la sicurezza della batteria e le sue prestazioni elettrochimiche. Gli elettroliti solidi inorganici (ISE) presentano elevata conducibilità ionica, ma anche fragilità e rigidità, perciò la ricerca è maggiormente rivolta verso gli elettroliti polimerici (PE). Gli elettroliti solidi polimerici (SPE) sono generalmente composti da una matrice polimerica reticolata e da uno o più sali alcalini; la conducibilità ionica dipende fortemente dal grado di cristallinità della matrice, poiché il trasporto degli ioni avviene prevalentemente nelle zone amorfe. L'inserimento di nanoparticelle di *filler* ionici, non ionici od organici permette di diminuire la frazione cristallina, ottenendo elettroliti polimerici compositi (CPE). Parallelamente, è possibile sottoporre gli SPE a *swelling*, utilizzando liquidi organici o IL, con la formazione di elettroliti gel polimerici (GPE): in questo caso la conduzione ionica avviene principalmente nella fase liquida assorbita dalla matrice polimerica.

In questo lavoro di tesi sono stati analizzati e testati alcuni innovativi elettroliti polimerici gel-compositi (GCPE); essi sono costituiti da una matrice polimerica reticolata, che include policaprolattone di-metacrilato (PCLDMA), polietilenglicole (PEG) e ureido-pirimidinone metacrilato (UPy-MA); quest'ultimo conferisce proprietà di autoriparazione, grazie alla formazione di legami a idrogeno nelle zone danneggiate della membrana. Nella matrice è presente nanolignina Bretax come additivo: si tratta di un ligninsolfonato prodotto tramite il processo di estrazione denominato "processo al solfito". Le membrane sono sottoposte a *swelling* nell'elettrolita liquido organico a base di KPF_6 0.80 M in 1:1 EC:DEC, portando all'ottenimento di un gel. Le sei tipologie esaminate differiscono nel contenuto di nanolignina,

che varia tra 0 e 20% in peso, riferito alla massa del polimero PCLDMA. Nella Tabella 1 sono indicate le composizioni delle differenti membrane polimeriche composite (CPM).

Tabella 1: Acronimi e composizione delle CPM analizzate.

Acronimo	PEG (m/m$_{PCLDMA}$)	UPy-MA (m/m$_{PCLDMA}$)	Nanolignina Bretax (m/m$_{PCLDMA}$)
CPM0	10%	4%	0%
CPM3	10%	4%	3%
CPM5	10%	4%	5%
CPM7	10%	4%	7%
CPM10	10%	4%	10%
CPM20	10%	4%	20%

Le CPM sono state prodotte e fornite dal Politecnico di Milano. La preparazione prevede la miscelazione di opportune quantità dei tre polimeri costituenti, insieme a una soluzione di CHCl$_3$ contenente nanolignina Bretax, ottenuta tramite ultrasonicazione. È quindi addizionato un foto-iniziatore, che consente di effettuare il trattamento di UV-*curing*: in seguito alla deposizione della soluzione su una lastra di vetro, essa viene sottoposta a radiazioni UV che permettono l'avvenimento delle reazioni di reticolazione.

Le CPM sono state analizzate tramite calorimetria differenziale a scansione (DSC) ed è stata valutata la quantità di elettrolita liquido che esse possono incorporare (EUR). Successivamente sono state effettuate prove di tipo elettrochimico, quali voltammetria a scansione lineare (LSV), test di stabilità interfacciale, misurazione della conducibilità ionica, test di *plating and stripping*, ciclazione galvanostatica e test di autoriparazione.

Calorimetria differenziale a scansione

La DSC è una tecnica di analisi di tipo termico, in cui il materiale in esame e uno di riferimento vengono sottoposti a una variazione di temperatura controllata e viene misurata la differenza di flusso di calore tra i due campioni. La differenza di calore assorbito è correlata alle transizioni di fase del materiale in esame, le quali sono mostrate come picchi endotermici o esotermici su un termogramma DSC, dove il flusso di calore è riportato in funzione della temperatura. Questo test permette di valutare la tipologia e il grado di purezza dei materiali analizzati, e di determinare le loro proprietà termiche, come le temperature e le entalpie di transizione di fase.

L'analisi DSC ha permesso di valutare la temperatura di transizione vetrosa (T$_g$) e l'entalpia di cristallizzazione delle CPM. Sono state eseguite tre prove termiche tra -100 e 120 °C, con una velocità di riscaldamento di 20 °C min^{-1}; i dati ottenuti dalla terza prova sono mostrati in Figura 3. Come mostrato nell'immagine, l'incremento della concentrazione di lignina provoca un aumento della T$_g$, poiché elevate quantità di nanoparticelle di *filler* possono ridurre e

parzialmente ostacolare la mobilità delle catene polimeriche. Tuttavia, si manifesta una riduzione dell'entalpia di cristallizzazione: questo andamento suggerisce che la presenza di nanolignina causi un aumento della frazione amorfa della matrice, in quanto il riempitivo perturba la disposizione cristallina, tipica di alcune catene polimeriche. I valori di T_g e dell'entalpia specifica di cristallizzazione ($\Delta H/m_{campione}$) delle CPM analizzate sono riportati in Tabella `.
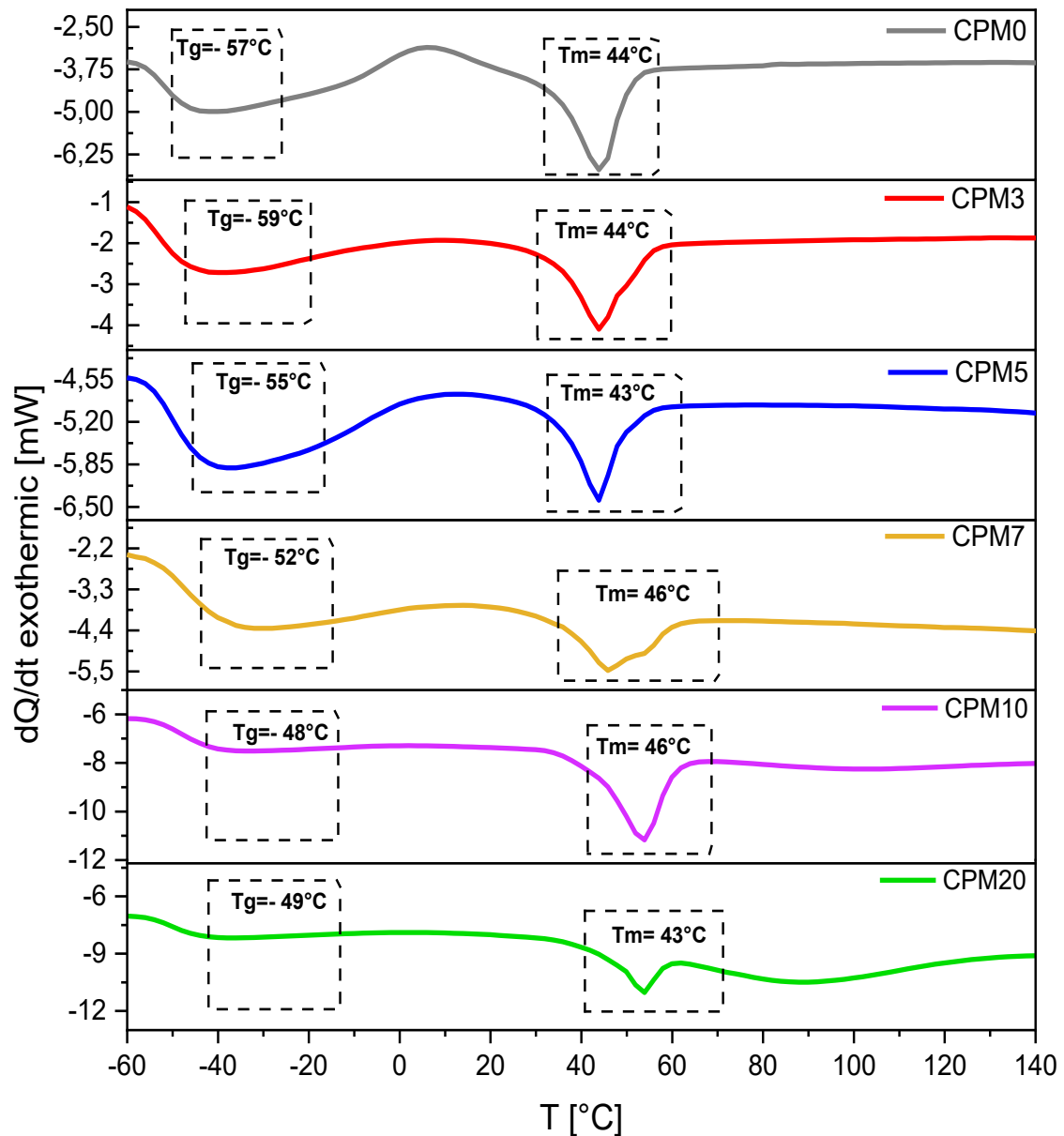

Figura 3: Grafico di DSC delle sei membrane analizzate.

Tabella 2: Valori di T_g e $\Delta H/m_{campione}$ delle CPM analizzate.

Acronimo	T_g [°C]	$\Delta H/m_{campione}$ [J/g]
CPM0	-57	-18
CPM3	-59	-10
CPM5	-55	-6
CPM7	-52	-7
CPM10	-48	-7
CPM20	-49	-3

Quantità di elettrolita incorporato

L'EUR rappresenta la quantità di elettrolita liquido che la CPM può assorbire durante il processo di *swelling*. La quantità di liquido assorbita dipende dalla porosità e dal grado di reticolazione della matrice polimerica, ossia dalla frazione di vuoto accessibile; essa determina la conducibilità ionica del GCPE, poiché il trasporto di ioni avviene principalmente nell'elettrolita liquido.

L'EUR è stato valutato utilizzando l'elettrolita liquido organico KPF_6 0.8 M in 1:1 EC:DEC. Le CPM sono state sottoposte a *swelling* in *glove box* e la loro variazione di massa è stata valutata a intervalli di 5 minuti. I dati ottenuti sono presentati in Figura 4, in cui l'EUR [%] è riportato rispetto al tempo [s]. Le sei membrane raggiungono un valore di EUR circa costante dopo 30 minuti di *swelling*. La CPM0 mostra la maggiore velocità di assorbimento e un valore di plateau di ≈125%, grazie alla struttura omogenea e dinamica, che consente di incorporare una grande quantità di liquido. Al contrario, con l'aggiunta di nanolignina, la capacità della membrana di assorbire il liquido subisce l'effetto positivo della riduzione della frazione cristallina e l'effetto negativo della limitazione dei movimenti delle catene polimeriche, insieme alla diminuzione del volume libero, già occupato dalle particelle composite. La CPM3 è caratterizzata dal comportamento peggiore, con un valore di EUR di plateau pari a ≈94%; la CPM7 rappresenta il miglior compromesso, mostrando i valori di EUR più elevati; tutte le altre membrane mostrano un valore di plateau simile, che è intermedio tra quelli di CPM0 e CPM3. I grafici delle CPM10 e CPM20 mostrano una pendenza inferiore rispetto alle CPM5 e CPM7, poiché il maggiore contenuto di lignina riduce la mobilità macromolecolare, a causa della formazione di interazioni intermolecolari; pertanto, anche la velocità di assorbimento del liquido risulta ridotta.
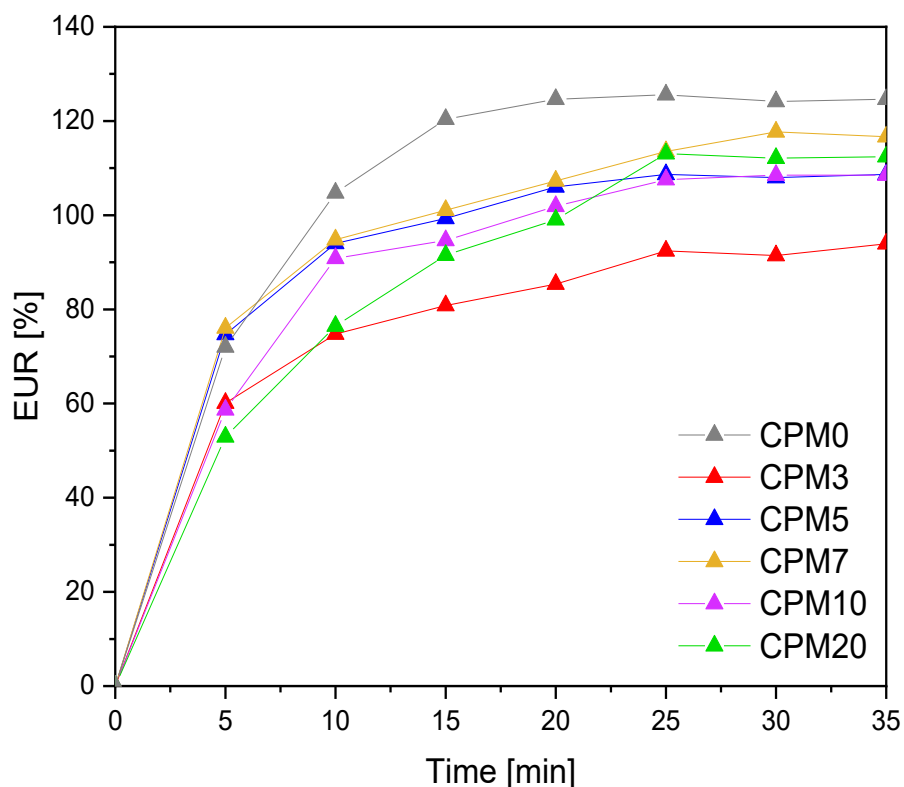
Figura 4: Quantità di elettrolita incorporato vs. tempo; confronto tra le sei membrane analizzate.

Voltammetria a scansione lineare

La prova elettrochimica LSV permette di valutare la ESW dei GCPE, utilizzando la configurazione di EL-cell, in cui sono presenti un elettrodo in potassio metallico e un pistone in acciaio inossidabile. Durante il test, il potenziale è stato variato linearmente tra 0 e 5 V tramite un potenziostato, con una velocità di scansione di 0.1 mV s^{-1}.

Il GCPE0 è stabile nell'intero intervallo di analisi, come mostrato in Figura 5, in cui la corrente si mantiene costante al valore di 0 A. I cinque GCPE contenenti lignina sono per lo più stabili nell'intervallo di potenziale di lavoro (tra 0.01 e 3 V), ma le curve mostrano valori di corrente diversi da zero intorno a 0.5 V. GPCE5, GPCE7, GPCE10 e GPCE20 sono caratterizzati da un picco di corrente alla tensione di ≈4.5 V: tale andamento rappresenta l'accadimento di reazioni indesiderate; queste ultime potrebbero essere dovute alla presenza di lignina, in quanto il picco non è presente nel grafico del GCPE0.
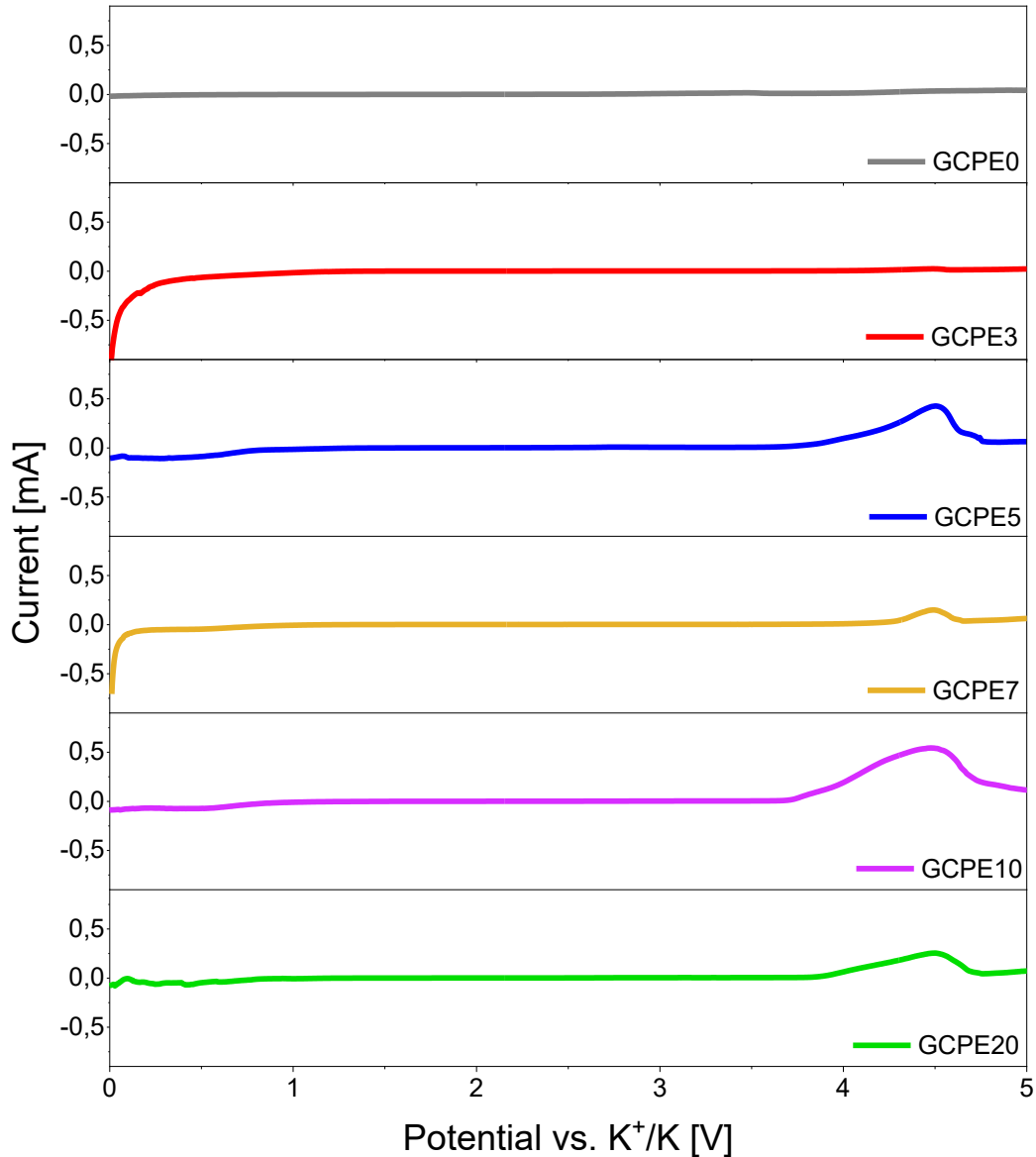
Figura 5: Voltammogrammi LSV delle sei membrane analizzate.

Conducibilità ionica

La conducibilità ionica dell'elettrolita può essere valutata attraverso un'analisi PEIS: in questo lavoro di tesi, la configurazione utilizzata è stata la EL-cell, in cui il GCPE è stato posto tra due elettrodi in acciaio inossidabile. La cella, collegata al potenziostato, è stata inserita in una camera climatica, al fine di valutare la dipendenza della conducibilità dalla temperatura; per ogni GCPE sono stati eseguiti sei test PEIS, a temperature costanti (10, 20, 30, 40, 50, 60 °C).

I sei elettroliti presentano simili andamenti di conducibilità ionica al variare della temperatura, come mostrato in Figura 6, in cui la conducibilità [S cm^{-1}] è rappresentata in funzione di 1000/T [K^{-1}]. Come previsto, il GCPE0 presenta la maggiore conducibilità nell'intero intervallo di temperatura, raggiungendo il valore di 1.59·10^{-3} S cm^{-1} a 60 °C. Il peggior conduttore ionico è rappresentato dal GCPE3, caratterizzato dal minor EUR; il comportamento migliora con l'aumento del contenuto di nanolignina e il GCPE20 raggiunge il valore di conducibilità di

$1.32 \cdot 10^{-3}$ S cm^{-1} a 60 °C. L'aumento della concentrazione di lignina riduce la cristallinità della matrice polimerica e aumenta l'EUR; entrambe queste variazioni migliorano la conducibilità ionica, che avviene principalmente nelle regioni amorfe e nella frazione liquida.
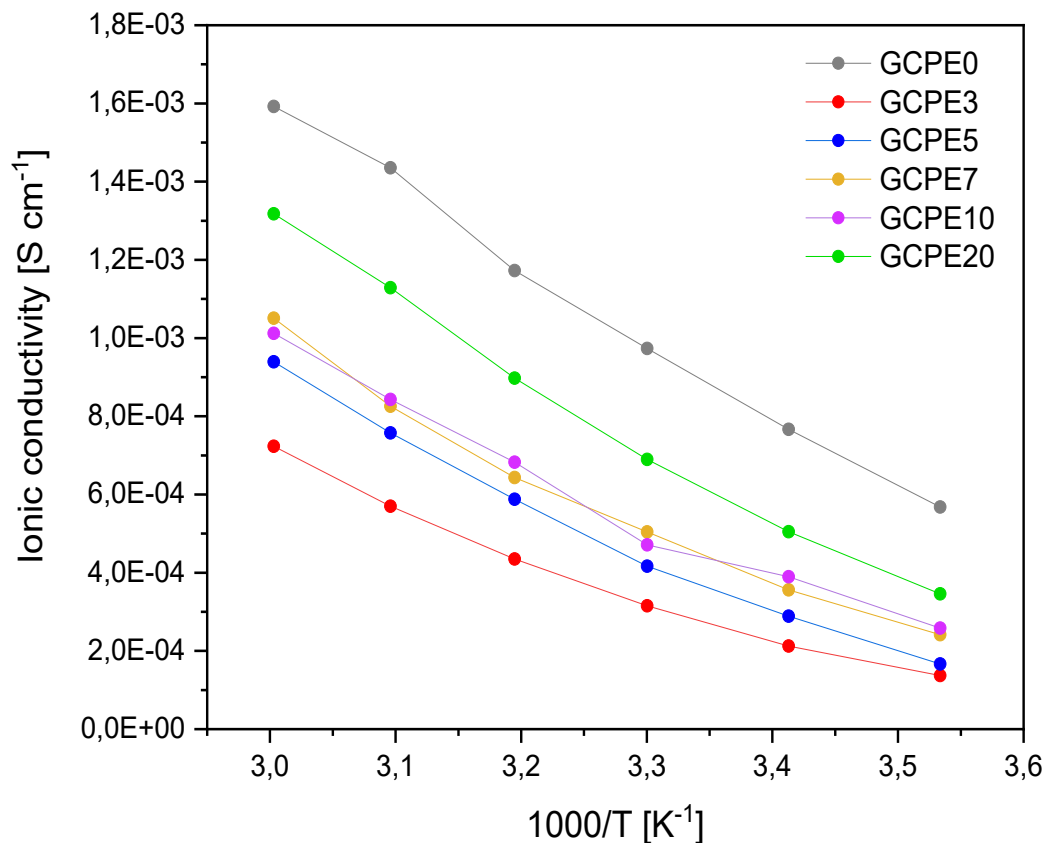
Figura 6: Conducibilità ionica vs. 1000/T; confronto tra le sei membrane analizzate.

Test di stabilità interfacciale

L'analisi di stabilità interfacciale è stata eseguita per valutare la stabilità dell'elettrolita nei confronti dell'elettrodo in potassio metallico, considerando un lungo periodo di tempo e mantenendo la cella al suo potenziale a circuito aperto (OCV). Le numerose prove PEIS sono state eseguite sui GCPE a distanza di 3/8 giorni; per quest'analisi è stata utilizzata la configurazione di *coin cell*, in cui l'elettrolita è stato posto tra due dischi in potassio metallico.

I GCPE analizzati mostrano un iniziale leggero aumento del valore di R$_s$, che rappresenta il verificarsi di reazioni indesiderate all'interno del *bulk* di elettrolita liquido; tuttavia, il valore diviene stabile dopo circa 20 giorni. Al contrario, tutti i GCPE mostrano un continuo aumento del valore di R$_{ct}$ nel tempo: questo andamento illustra un deterioramento della superficie del potassio metallico, che reagisce continuamente con l'elettrolita. Gli andamenti di R$_s$ e R$_{ct}$ evidenziano la presenza di reazioni tra il potassio metallico e l'elettrolita, le quali si verificano solamente in corrispondenza dell'interfaccia, mentre non hanno luogo nel *bulk* dell'elettrolita.

Test di *plating and stripping*

Il test di *plating and stripping* permette di valutare la capacità dell'interfaccia elettrolita-elettrodo di condurre ioni K^+ in modo omogeneo. Durante questa analisi, una densità di corrente costante è applicata per 1 h, quindi essa viene invertita e applicata per un'altra ora; la tensione di polarizzazione risultante è costantemente misurata e il test viene ripetuto per un numero predeterminato di cicli. Nella configurazione di EL-cell utilizzata, il GCPE è stato posto tra due dischi in potassio metallico.

Il test di *plating and stripping* è stato realizzato sui GCPE7, GCPE10 e GCPE20, poiché essi mostrano le migliori prestazioni complessive, con l'applicazione di una densità di corrente di 0.1 mA cm^{-2} per 70 cicli. Il GCPE7 mostra un moderato aumento di potenziale nel corso del tempo [Figura 7]; l'assenza di picchi esclude la formazione e la crescita di dendriti sulla superficie del potassio metallico. Come mostrato in Figura 8, il GCPE10 è caratterizzato da un forte aumento di potenziale nei primi cicli e da un improvviso decremento al ciclo 8: questo andamento potrebbe essere causato dalla formazione di uno strato SEI con spessore estremamente elevato, che impedisce il passaggio degli ioni, come dimostrato dalla forma rettangolare del grafico. I picchi presenti tra i cicli 17 e 21 rappresentano la possibile formazione di dendriti; tuttavia, essi non perforano la membrana e non provocano cortocircuito. Il GPCE20 presenta il miglior andamento di potenziale [Figura 9], caratterizzato da un valore iniziale molto basso e da un aumento limitato nell'intero test; pertanto, gli strati SEI risultano omogenei e stabili e assicurano un'ottima conduzione ionica.
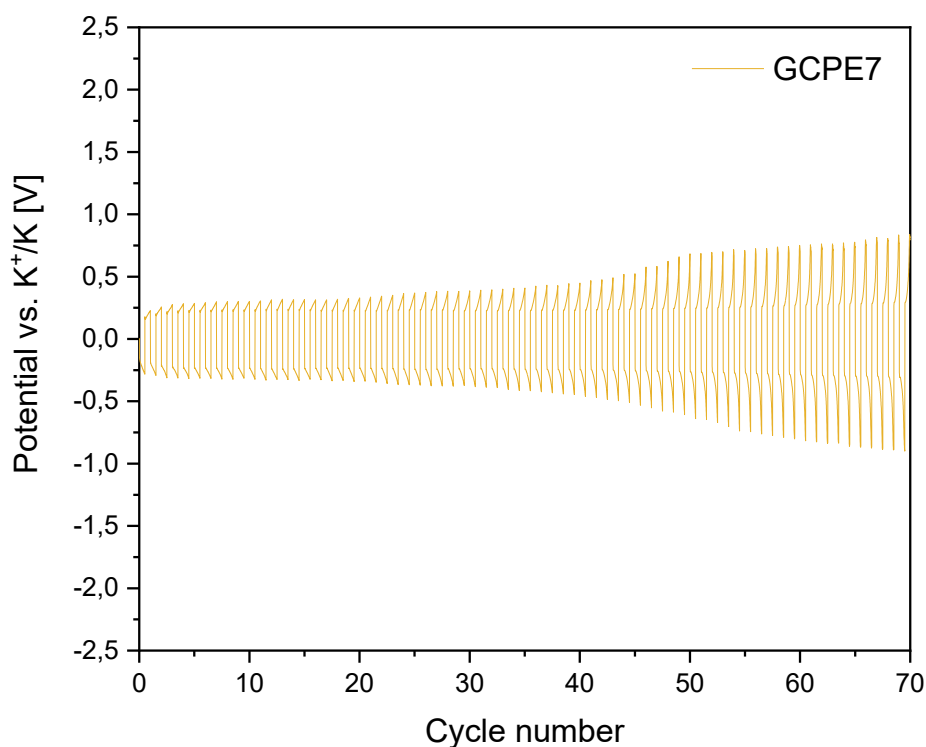
Figura 7: Grafico del test di *plating and stripping* per il GCPE7.
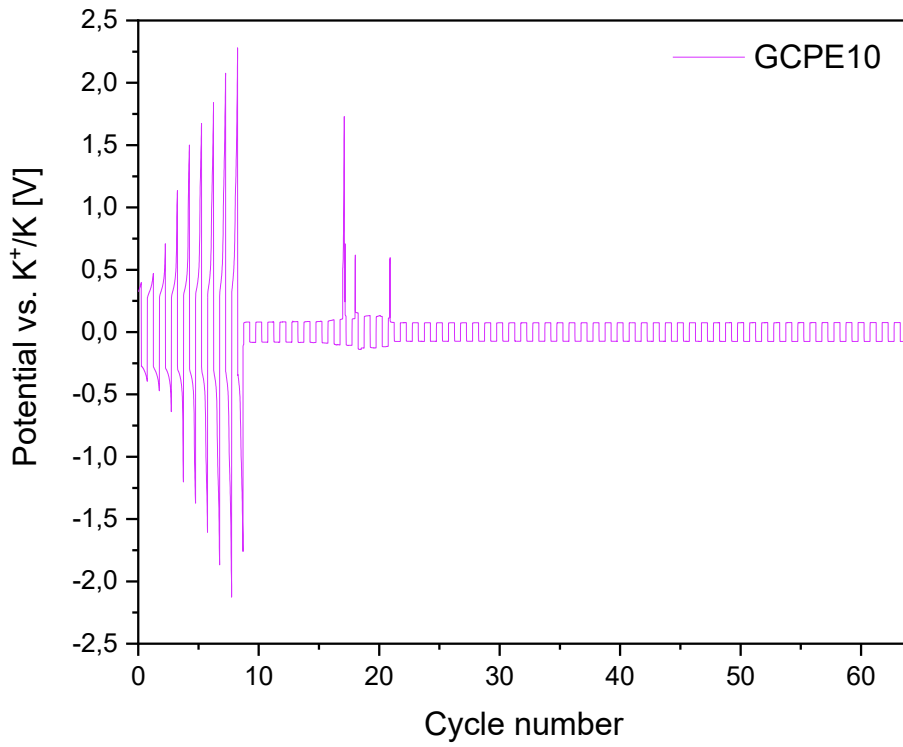
Figura 8: Grafico del test di *plating and stripping* per il GCPE10.
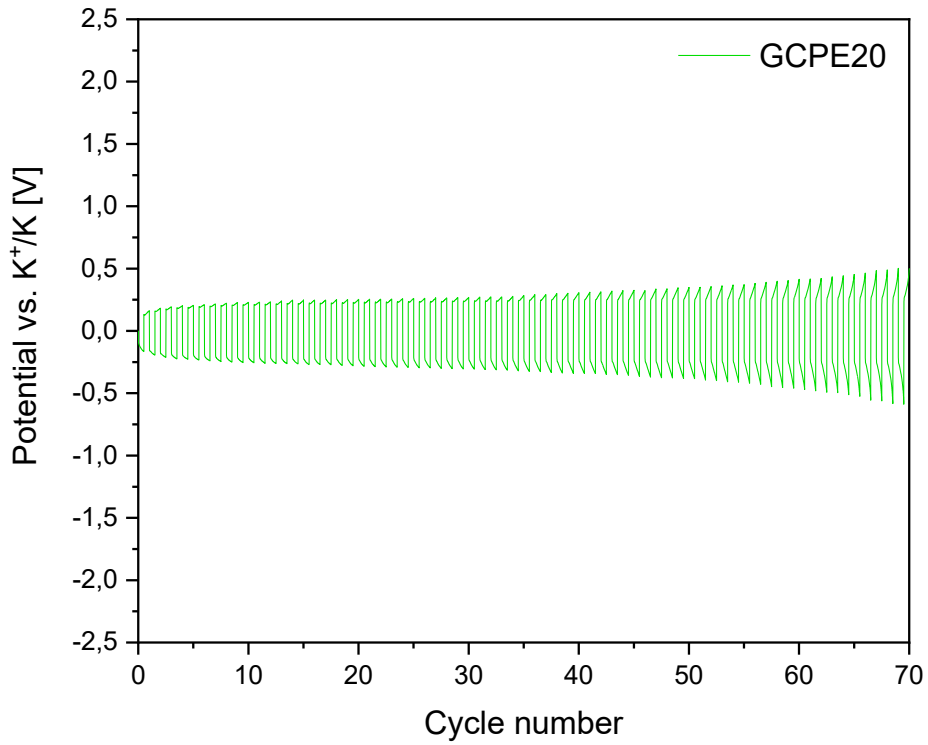

Figura 9: Grafico del test di *plating and stripping* per il GCPE20.

Ciclazione galvanostatica

La ciclazione galvanostatica è un test di carica/scarica eseguito da un ciclatore, il quale può applicare diverse correnti alla cella, aumentandone o diminuendone il potenziale. La corrente positiva definisce il processo di carica, durante il quale gli ioni K^+ si spostano dall'elettrodo positivo in carbonio Super P all'elettrodo negativo in potassio metallico. Il processo di scarica è opposto, ed è determinato dalla corrente negativa. Il potenziale risultante viene costantemente misurato e la sua variazione è consentita in un intervallo predeterminato; quando il potenziale raggiunge i valori limite, il ciclatore inverte la corrente. Durante l'analisi vengono inoltre misurate le capacità di carica (CC) e di scarica (DC), in quanto rappresentative delle prestazioni elettrochimiche della cella. Nel corso dei cicli, le capacità diminuiscono inevitabilmente, a causa della degradazione che riguarda sia gli elettrodi che l'elettrolita.

In questo lavoro di tesi, la ciclazione galvanostatica è stata eseguita dal ciclatore Arbin e i dati sono stati elaborati dal software MITS Pro. Nella configurazione di *coin cell* impiegata, il GCPE è stato posto tra un elettrodo in potassio metallico e un elettrodo in carbonio Super P. La ciclazione è stata eseguita con una corrente specifica di ±0.05 Ah g⁻¹ per i primi dieci cicli, mentre per i successivi il valore è stato aumentato a ±0.1 Ah g⁻¹. I GCPE mostrano una diminuzione molto elevata della capacità specifica durante i primi ≈10 cicli: questo andamento è sempre rilevabile in presenza di un elettrodo in carbonio Super P. Il GCPE0 presenta curve irregolari delle capacità di carica e scarica [Figura 10]: questo comportamento potrebbe essere dovuto alle scarse proprietà meccaniche, a causa delle quali esso non resiste adeguatamente ai cambiamenti di volume degli elettrodi e al flusso di ioni che attraversa la propria struttura. Questa ipotesi è stata ulteriormente supportata dal verificarsi di cortocircuito dopo ≈600 cicli.
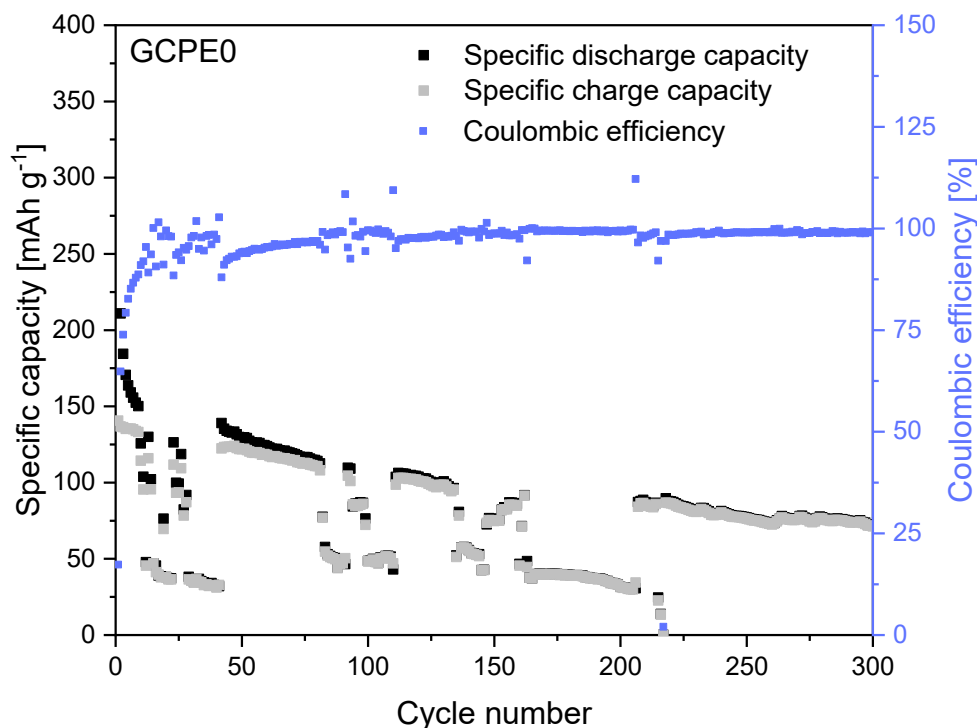

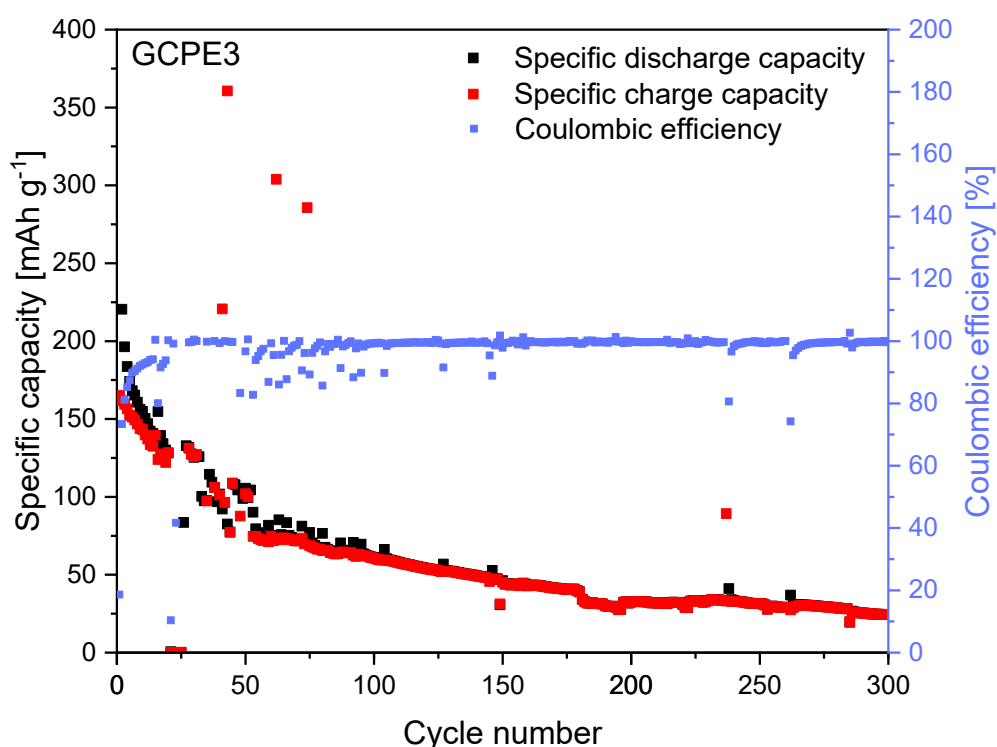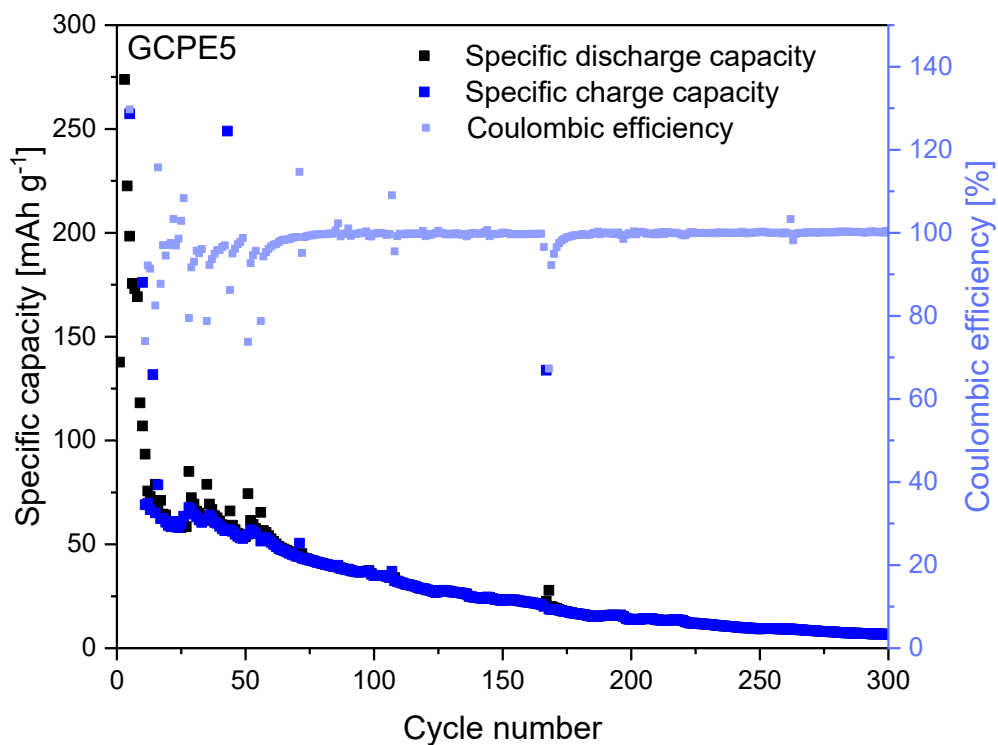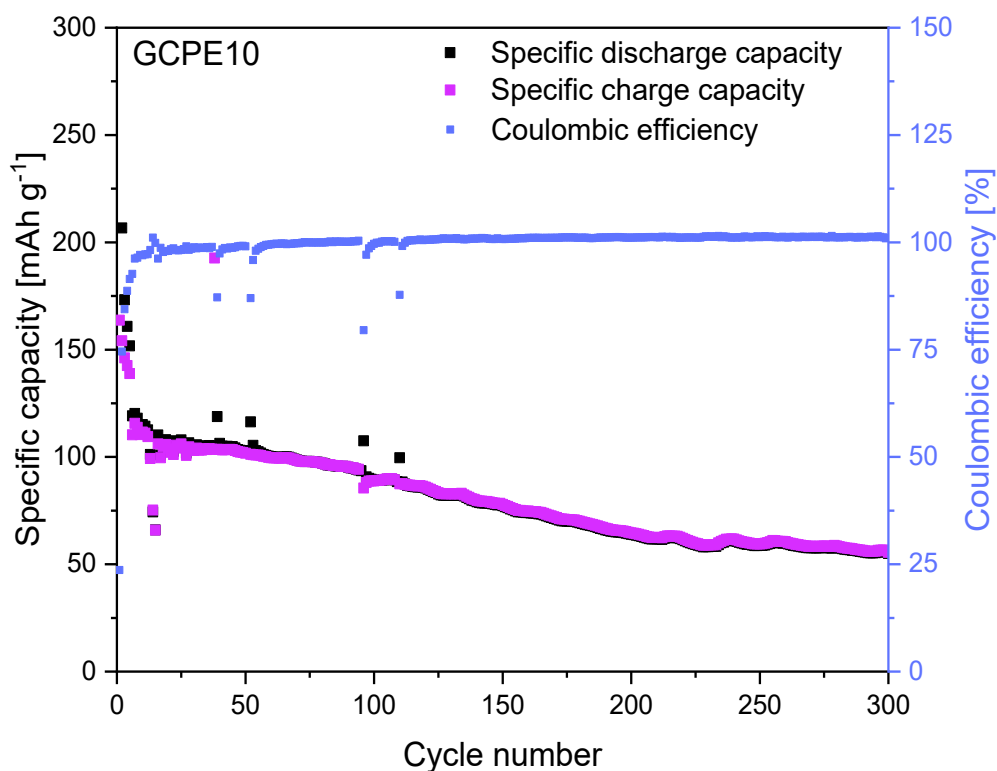**Figura 10**: Capacità specifiche di carica/scarica ed efficienza Coulombica vs. numero di cicli per il GCPE0.

Le capacità specifiche di carica e scarica mostrano un andamento iniziale irregolare per i GCPE3, GCPE5 e GCPE7, con una stabilizzazione dopo ≈50 cicli, quando anche l'efficienza Coulombica raggiunge il valore costante e ottimale di ≈99-100% [Figura 11, Figura 12, Figura 13]. Le fluttuazioni precedenti potrebbero essere dovute alle limitate proprietà meccaniche dei GCPE, che sono successivamente controbilanciate dalla formazione di strati SEI stabili. Le *coin cell* con GCPE3 e GCPE5 mostrano bassi valori di capacità specifiche di carica e scarica durante l'intero test, con modeste ritenzioni al 300° ciclo (33% per GCPE3 e 13% per GCPE5). La ritenzione è stata valutata considerando la capacità di carica specifica del primo ciclo stabile e quella del 300° ciclo. La cella con GCPE7 presenta valori di capacità specifica elevati, ma purtroppo ha subito cortocircuito dopo 160 cicli.

Figura 11: Capacità specifiche di carica/scarica ed efficienza Coulombica vs. numero di cicli per il GCPE3.

Figura 12: Capacità specifiche di carica/scarica ed efficienza Coulombica vs. numero di cicli per il GCPE5.
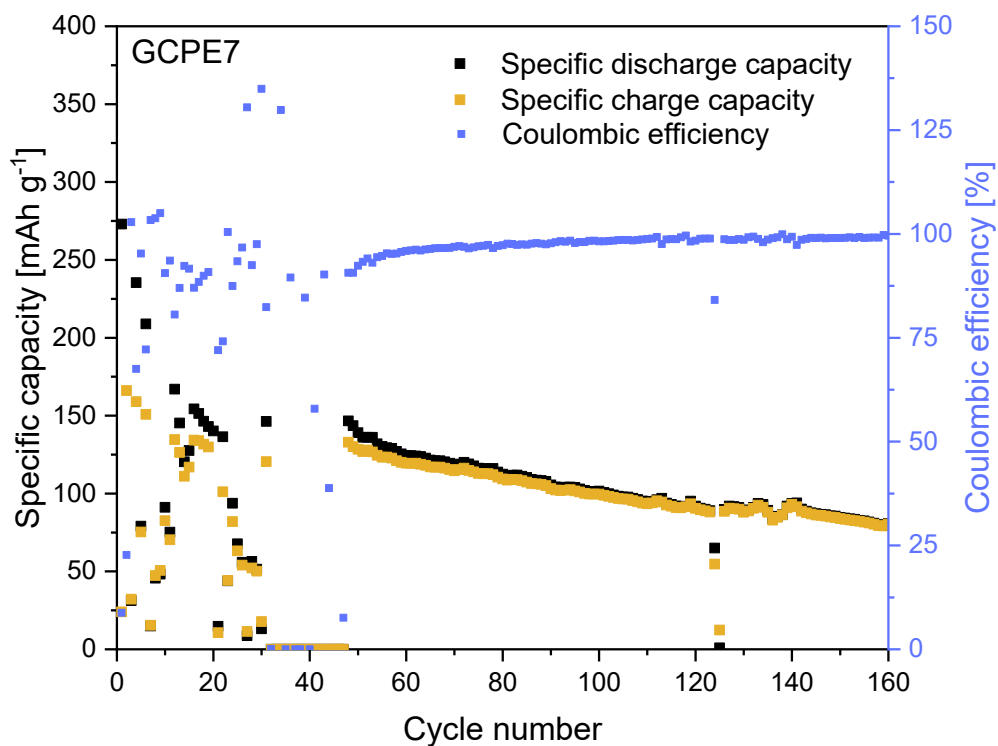
Figura 13: Capacità specifiche di carica/scarica ed efficienza Coulombica vs. numero di cicli per il GCPE7.

Le *coin cell* contenenti i GCPE10 e GCPE20 mostrano i migliori comportamenti [Figura 14, Figura 15], grazie all'elevata concentrazione di lignina, che migliora le proprietà meccaniche delle membrane, la conducibilità ionica e la stabilità degli strati SEI. L'andamento della capacità specifica si stabilizza a ≈25 cicli per il GCPE10, la cui cella presenta valori di capacità relativamente elevati e la massima ritenzione al 300° ciclo (53%). La *coin cell* contenente il GCPE20 mostra un'inferiore ritenzione a 300 cicli (44%), ma raggiunge valori di capacità specifica più elevati e presenta un'ottima stabilità sin dai primi cicli. Ottimali valori di efficienza Coulombica sono mostrati da entrambe le celle (≈100%).

Figura 14: Capacità specifiche di carica/scarica ed efficienza Coulombica vs. numero di cicli per il GCPE10.
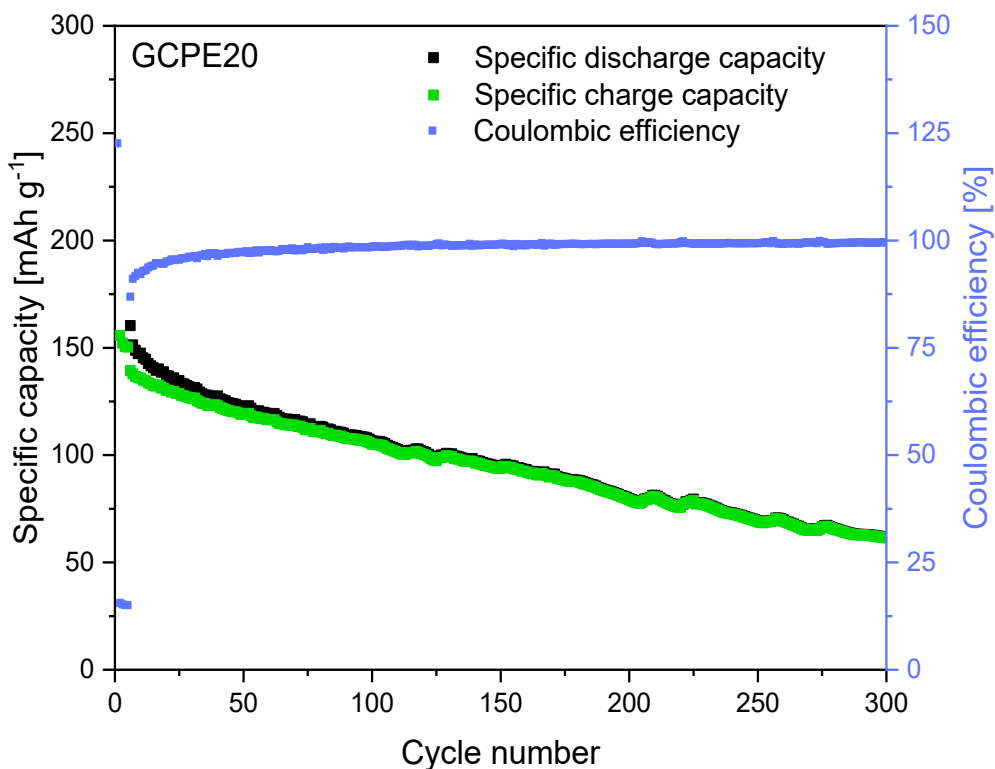
Figura 15: Capacità specifiche di carica/scarica ed efficienza Coulombica vs. numero di cicli per il GCPE20.

Il GPCE10 è stato ulteriormente analizzato tramite ciclazione galvanostatica, al fine di valutarne le proprietà di autoriparazione. In questo caso è stata utilizzata la configurazione di EL-cell, assemblata con un anodo in potassio metallico, l'elettrolita e un catodo in carbonio Super P. La cella è stata inizialmente sottoposta a 10 cicli di carica/scarica con una densità di corrente specifica di ±0.05 A g^{-1}; successivamente, essa è stata aperta e in seguito all'apertura è stato eseguito un piccolo taglio sulla membrana [Figura 16]. La cella è stata quindi richiusa e nuovamente sottoposta alla medesima ciclazione galvanostatica.
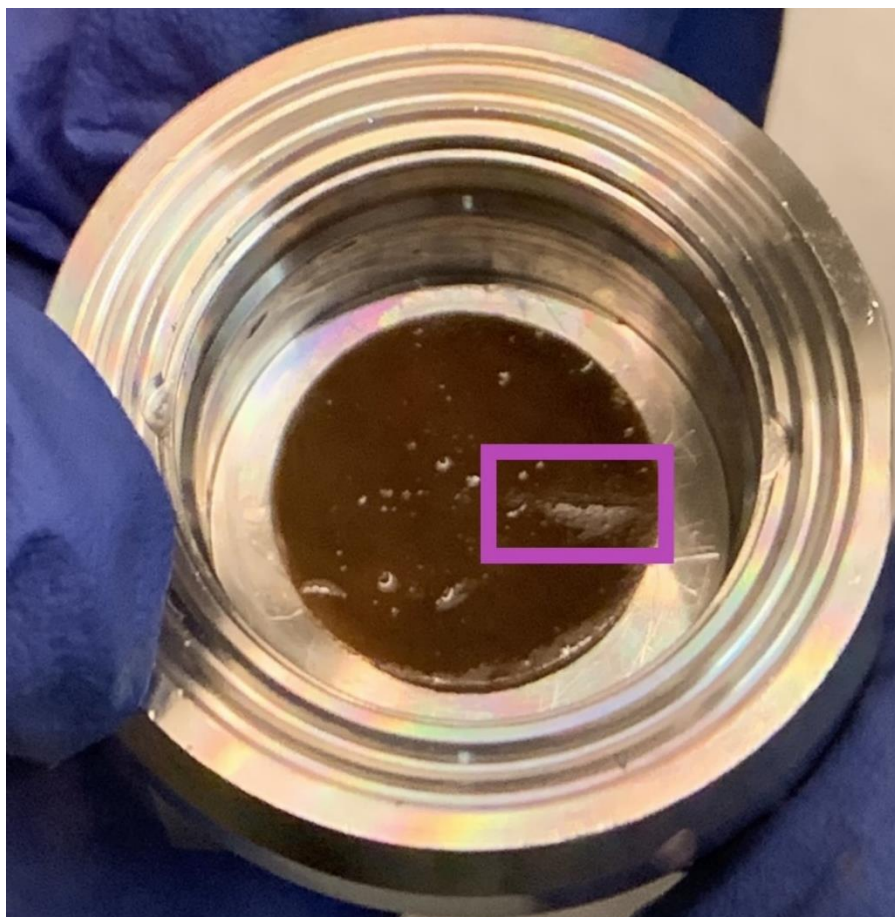
Figura 16: Taglio effettuato sulla GCPE10 dopo i 10 cicli iniziali di carica/scarica.

Le capacità specifiche di carica e scarica dei diversi cicli sono visualizzate in Figura 17. Tra i cicli 10 e 11 si registra una diminuzione netta della capacità specifica, corrispondente all'apertura della EL-cell e all'esecuzione del taglio. Nonostante il danno, la cella non ha subito cortocircuito; quest'ultimo sarebbe potuto avvenire in quanto gli ioni si muovono preferenzialmente attraverso le parti caratterizzate da una minore resistenza, come l'area di taglio. Una possibile spiegazione riguarda la capacità di autorigenerazione dell'UPy-MA: la formazione di legami a idrogeno potrebbe aver ridotto l'entità del danno e ripristinato parzialmente la stabilità della membrana.
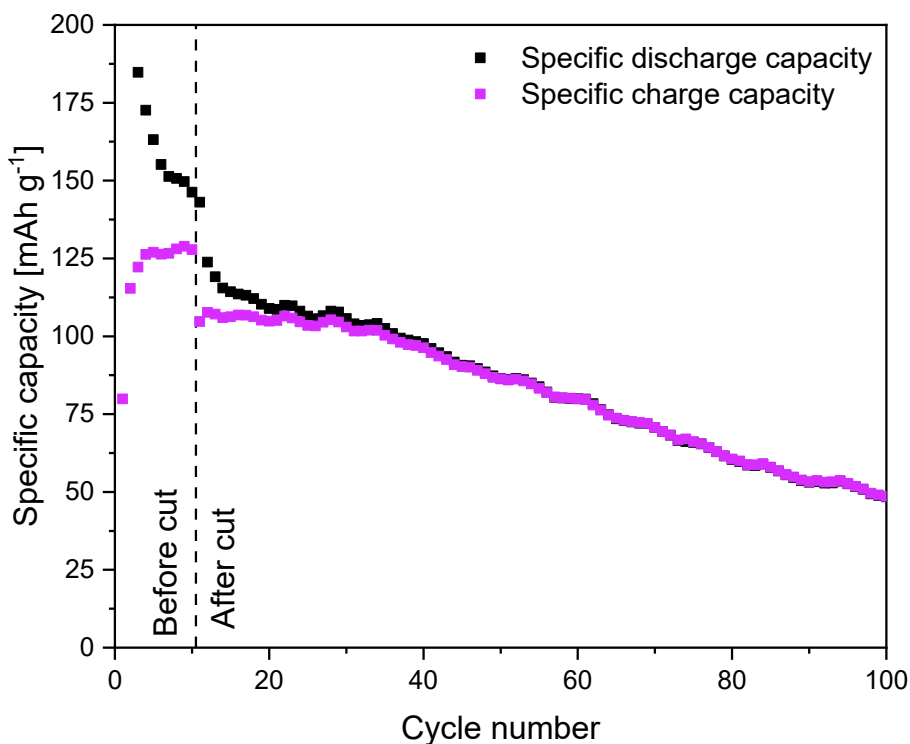
Figura 17: Capacità specifiche di carica/scarica vs. numero di cicli per il GCPE10, test di autoriparazione.

Conclusioni

Considerando il miglioramento generale delle proprietà dei GCPE all'aumentare del contenuto di nanolignina, l'analisi di membrane con concentrazioni di *filler* più elevate consentirà di identificare il valore che determina le prestazioni massime. In questa prospettiva, è necessario apportare dei miglioramenti nelle tecniche di produzione delle membrane, in quanto l'aumento della concentrazione di lignina peggiora la miscelazione e la dissoluzione dei componenti, il processo di reticolazione e la stesura della membrana. Sarà quindi possibile individuare una quantità massima di nanolignina, oltre la quale la reticolazione sarebbe ostacolata e che causerebbe eccessiva rigidità e fragilità della membrana.

Contents

Abstract

The global energy consumption is continuously increasing, together with several related issues. Fossil fuels represent the principal energetic sources, the main limits of which are the non-renewability and the pollution that derives from their exploitation: the consequences are evidently noticeable in the climate changes. The transition towards renewable energy sources is firmly necessary in order to avoid worse repercussions, but resources, such as solar and wind energies, are intrinsically intermittent and their trend and performance are unpredictable: for these reasons they cannot constantly satisfy the electric energy request. A feasible solution is represented by the use of energy storage systems, which can accumulate energy when the productivity is maximum and provide it afterwards. The lithium-ion technology is the most studied and developed one; it is employed in several applications, such as electric vehicles and portable electronic devices. Some drawbacks are unfortunately associated with this technology: lithium only represents the 0.0017% by weight of Earth crust, therefore it is highly expensive, and its geographical distribution is extremely localized, mostly in countries characterized by political instability.

Research is thus moving towards other battery technologies and it is particularly focused on potassium. Potassium-ion batteries (KIBs) are the main candidates to substitute lithium ones: this alkali metal constitutes the 1.5% by weight of Earth crust and its global distribution is relatively homogeneous. The standard reduction potential of K^+/K (-2.93 V vs. SHE) is similar to that of Li^+/Li (-3.04 V vs. SHE), therefore it allows to obtain performances close to those of lithium. A further advantage is represented by the small K^+ Stokes radius, despite its large ionic radius, which results in a higher transport rate in the electrolyte, if compared with Li^+ ions.

A fundamental target for KIBs development concerns the electrolytes: it is necessary to find cheap and eco-friendly materials, which can simultaneously increase the battery safety and its performances. In this thesis work, some novel gel-composite polymer electrolytes (GCPEs) were studied and tested: they consist of a lignin-composite polymer membrane (CPM), swelled in an organic liquid electrolyte. The membrane matrix consists of cross-linked and interpenetrated polycaprolactone di-methacrylate (PCLDMA), poly(ethylene glycol) (PEG) and ureido-pyrimidinone methacrylate (UPy-MA); the latter provides self-healing (SH) properties, through the formation of multiple hydrogen bonds in the membrane damaged areas. Bretax nanolignin is present in the matrix as composite filler and the membranes are swelled in the organic liquid electrolyte KPF_6 0.8 M in 1:1 EC:DEC, obtaining the gel form. The five examined types differ in the nanolignin content, which varies between 3 and 20% by weight, referred to the mass of PCLDMA.

The dry membranes were analyzed by differential scanning calorimetry and their electrolyte uptake ratio was evaluated. The performed electrochemical tests include linear sweep voltammetry, interfacial stability tests, ionic conductivity measurements, plating and stripping tests, galvanostatic cycling and SH tests. The configurations used for the analyses are the coin cell and the EL-cell, assembled in a glove box; for the galvanostatic cycling, a metallic potassium anode and a Super P carbon cathode were used. The results of the performed tests display an overall improvement in the GCPEs electrochemical performances with the increase in the nanolignin content. A higher lignin concentration allows to reduce the crystallinity of the

polymeric matrix, to improve its mechanical properties and to increase the electrolyte uptake ratio; as a consequence, the GCPE shows an increased ionic conductivity, the formation of more stable SEI layers and better cycling performances.

List of figures

List of tables

List of acronyms

BASE β-alumina solid electrolyte

BC Bacterial cellulose

BG Berlin Green

CAES Compressed air energy storage

CC Charge capacity

CE Counter electrode

CN Cyanide

CNF Cellulose nanofibril

CNT Carbon nanotube

COF Covalent organic framework

C_p Heat capacity

CPE Composite polymer electrolyte

CPM Composite polymer membrane

CPU Carboxylated polyurethane

DC Discharge capacity

DEC Diethyl carbonate

DEGDME Diethylene glycol dimethyl ether

DFEC Difluoroethylene carbonate

DMC Dimethyl carbonate

DMSO Dimethyl sulfoxide

DOL 1,3-dioxacyclopentane

DSC Differential scanning calorimetry

EB Electrochemical battery

EC Ethylene carbonate

EES Electrical energy storage

EIS Electrochemical impedance spectroscopy

ElC Electrochemical cell

EMC Ethyl-methyl carbonate

ESS Energy storage system

ESW Electrochemical stability window

EV Electric vehicle

FCC Face centered cubic

FEC Fluoroethylene carbonate

FES Flywheel energy storage

FSI⁻ Bis(fluorosulfonyl)imide

GEIS Galvanostatic electrochemical impedance spectroscopy

GIC Graphite intercalation compound

GPE Gel polymer electrolyte

HC Hard carbon

HCS-SC Hard carbon-soft carbon composite

HPF Hexafluoropropylene

HNT Halloysite nanotube

HOMO Highest occupied molecular orbital

IEM 2-isocyanatoethyl methacrylate

IL Ionic liquid

ISE Inorganic solid electrolyte

K_2PC Potassium 2,5-pyridinedicarboxylate

K_2TP Potassium terephthalate

KFSI Potassium bis(fluorosulfonyl)imide

KIB Potassium-ion battery

KTFSI Potassium bis(trifluoromethanesulfonyl)imide

LAB Lead-acid battery

LIB Lithium-ion battery

LSV Linear sweep voltammetry

LUMO Lowest unoccupied molecular orbital

MIS 6-Methyl isocytosine

MOF Metal-organic framework

NCC Nanocrystalline cellulose

NIB Sodium-ion battery

NSB Sodium-sulfur battery

OCV Open circuit voltage

PAA Polyacrylic acid

PAN Poly(acrylonitrile)

PB Prussian Blue

PBA Prussian Blue analogue

PC Propylene carbonate

PCL Polycaprolactone diol

PCLDMA Polycaprolactone di-methacrylate

PE Polymer electrolyte

PEC Poly(ethylene carbonate)

PEEK Poly(ether ether ketone)

PEG Poly(ethylene glycol)

PEGMA Poly(ethylene glycol) methyl ether methacrylate

PEIS Potentiostatic electrochemical impedance spectroscopy

PEO Poly(ethylene oxide)

PHS Pumped hydroelectricity storage

PMMA Poly(methyl methacrylate)

PPC Poly(propylene carbonate)

PTCDA 3,4,9,10-per-tetracarboxylic acid-dianhydride

PTFE Poly(tetrafluoroethylene)

PTMC Poly(trimethylene carbonate)

PVA Poly(vinyl alcohol)

PVDF Poly(vinylidene fluoride)

PVP Poly(vinyl pyrrolidone)

PW Prussian White

RE Reference electrode

SC Soft carbon

SEI Solid electrolyte interface

SH Self-healing

SHE Standard hydrogen electrode

SIPE Single-ion conducting polymer electrolyte

SMES Superconductive magnetic energy storage

Sn(oct)$_2$ Stannous octoate

SPE Solid polymer electrolyte

SR Supramolecular rubber

SSE Solid state electrolyte

TEGDME Triethylene glycol dimethyl ether

TEP Triethyl phosphate

$TFSI^-$ Bis(trifluoromethanesulfonyl)imide

T_c Crystalline phase formation temperature

T_d Degradation temperature

T_g Glass transition temperature

T_m Melting temperature

TMO Transition metal oxide

TPO-L Ethyl phenyl(2,4,6-trimethylbenzoyl)phosphinate

UPy Ureido-pyrimidinone

UPy-MA Ureido-pyrimidinone methacrylate

UV Ultraviolet

VC Vinylene carbonate

WE Working electrode

WIS Water-in-salt

1 Introduction

1.1 Energy consumption, global warming and climate change

The industrialization process has led to an extensive increase in energy consumption, which is mostly met by fossil fuels. The combustion of these substances, such as coal and oil, causes the production of various pollutants and greenhouse gases, *e.g.* carbon dioxide, methane, nitrous oxide, carbon black, etc. [1]. These products are responsible for the climate changes and for the global warming that we are experiencing and that we absolutely need to limit. CO_2 is the primary contributor to the temperature increase, as it is proven in Figure 1.1.

Figure 1.1: Yearly temperature compared to the twentieth-century average (red and blue bars) from 1880 to 2019, based on data from NOAA NCEI, plus atmospheric carbon dioxide concentrations (grey line): 1880-1958 from IAC, 1959-2019 from NOAA ESRL. Original graph by Dr. Howard Diamond (NOAA ARL) and adapted by NOAA Climate.gov [3].

The atmospheric concentration of carbon dioxide has continuously increased since the beginning of the 20th century, reaching the value of 411 ppm in 2019 [2]. The same trend is followed by the temperature: in the period 1970-2019, the data show an increase of the average value of ≈ 1.2 °C [3].

It is a shared opinion among scientists that climate will keep on changing during the future decades, even supposing a complete revolution in human society behavior. Some of the main effects are:

- changes in precipitations patterns;

- more droughts and heat waves;
- stronger and more intense hurricanes;
- sea level further rise;
- further ice melting at the Arctic;
- further temperature increase [4].

We can still act to contain these events, but we cannot completely avoid their occurrence anymore.

One way to limit the climate changes is to achieve an energy transition: Europe is moving towards this target with the European Green Deal, the main aim of which is to become the first climate-neutral continent by 2050, with no net emissions of greenhouse gases [5]. This is possible by performing a change in our energy sources, from fossil fuels to renewable ones. The transition has already begun, but it has not reached acceptable results yet, due to significant problems which characterize solar, wind, hydro and other renewable energy sources. They are intrinsically intermittent; their trend and performance are unpredictable: for these reasons they cannot constantly satisfy the electric energy request.

A feasible solution is represented by the use of energy storage systems (ESS): they can accumulate energy when the productivity is maximum and provide it afterwards. The ESS would enable to balance the supply and demand and to stabilize the whole energy grid. Furthermore, they would allow the transition from a strongly localized energy production, in big power plants, to a distributed one, with more and smaller power plants: a direct consequence would be the increase in the energy transport and distribution efficiency [6,7].

1.2 Electrical energy storage

Among the ESSs, electrical energy storage (EES) systems are able to convert electric energy into a different form, suitable for storage, and to release it back when it is required. The EES systems classification is based on the mechanism used to store the electricity:

- mechanical systems: pumped hydroelectricity storage (PHS), compressed air energy storage (CAES), flywheel energy storage (FES);
- electrical systems: superconductive magnetic energy storage (SMES), capacitors, supercapacitors;
- electrochemical systems: secondary electrochemical batteries (lead-acid batteries (LABs), nickel-based batteries, sodium-ion batteries (NIBs), lithium-ion batteries (LIBs), alkaline-ion batteries), flow batteries [6].

1.2.1 Electrochemical batteries (EBs)

The EB stores electricity in form of chemical energy. Primary batteries can only undergo one discharge and they cannot be recharged, therefore they must be disposed. Secondary batteries can perform several charge-discharge cycles and they are much more versatile than primary ones.

The basic unit of an EB is the electrochemical cell (ElC). In a battery, the ElCs can be connected in series or in parallel: in the first case, the EB voltage equals the sum of the single ElCs ones, while in the second configuration the EB current equals the sum of the single ElCs ones.

The chemical potential energy contained in the ElC can be transformed into and released as electric energy through redox reactions occurring in the cell itself. The ElC is composed of two electrodes: the anode hosts the oxidation reaction, while the cathode hosts the reduction one. The third main component is the electrolyte, the aim of which is to allow the transport of negative and positive ions between the electrodes, as well as to hinder the flow of electrons, that would cause short-circuit [8].

Galvanic cell

The ElC in the form of a galvanic cell converts chemical energy into electric energy: in this configuration, the anode is the negative electrode and the cathode is the positive one. The electrons released at the anode flow towards the cathode [Figure 1.2], and this corresponds to the discharging phase of a secondary battery.

Oxidation semi-reaction at the anode (negative electrode):

$$Me \rightarrow Me^{n+} + ne^- \quad (1.1)$$
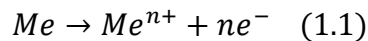
Reduction semi-reaction at the cathode (positive electrode):

$$X + ne^- \rightarrow X^{n-} \quad (1.2)$$
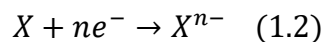
Overall reaction, sum of the anodic and of the cathodic ones:

$$Me + X \rightarrow Me^{n+} + X^{n-} \quad (1.3)$$
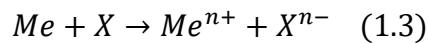
Electrolytic cell

The electrolytic cell represents the charging step of a secondary battery, during which an external current is applied and the electrons are forced to move back to the negative electrode. In this case, the anode is the positive electrode, while the cathode is negative [Figure 1.2].
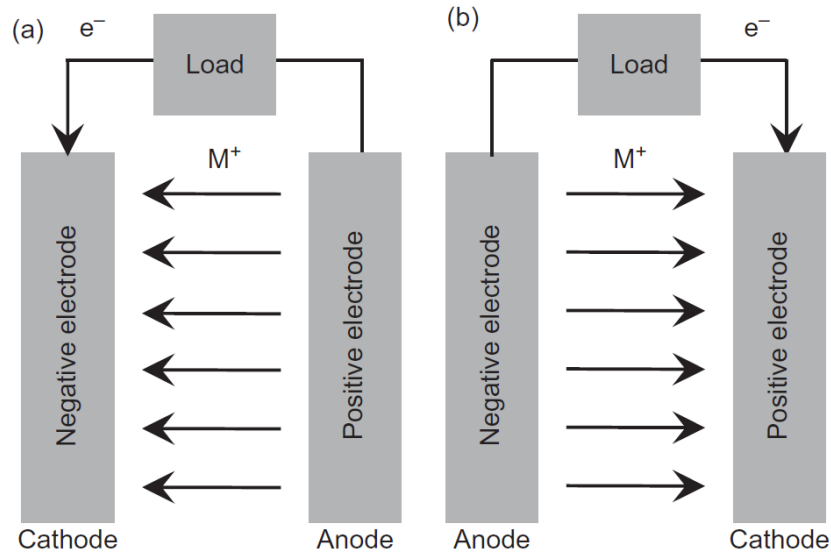
Figure 1.2: (a) Electrolytic cell, (b) galvanic cell [9].

1.3 Lithium-ion batteries (LIBs)

Among the electrochemical systems, LIBs represent the technology with the best performances. Their main characteristics include [10]:

- high energy and power density;
- low weight;
- absence of memory effect;
- relatively fast recharge;
- long cycle life;
- low self-discharge rate.

LIBs dominate the portable electronics sector, as power components of tablets, mobile phones and laptops, mostly thanks to their light weight and high energy and power density. In the last years, their production further increased with the huge development of electric vehicles (EVs), which are currently almost entirely powered by LIBs. The global demand for EV LIBs reached the capacity of 142.8 GWh in 2020 and it is estimated to grow up to 800 GWh in 2025 and to 6500 GWh in 2050 [Figure 1.3].
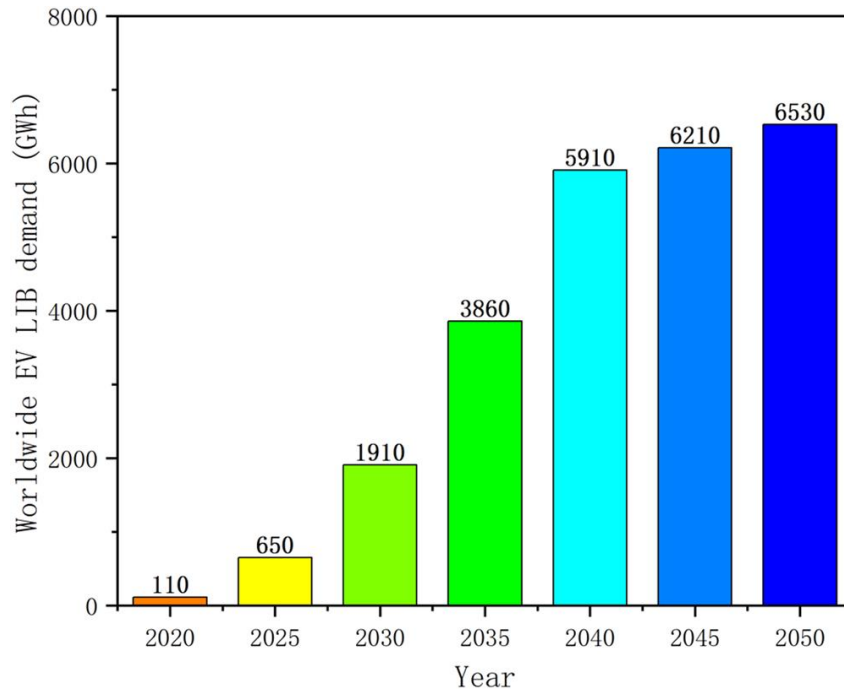
Figure 1.3: Global forecast demand for EV LIBs from 2020 to 2050 (in GWh) [11].

The extensive increase in LIBs implementation has highlighted several weaknesses and drawbacks. Lithium cost is continuously raising, due to its scarcity (it represents only the 0.0017% by weight of Earth crust) and its geographical distribution, which is extremely localized, mostly in countries characterized by political instability. Furthermore, the standard LIBs cathodes contain nickel and cobalt, which are even more expensive than lithium and make LIBs potentially dangerous for human health [12].

Considering the LIBs operating conditions, some safety issues must be taken into account. Improper use, accidents and defects can lead to undesired conditions, such as excessive heat production, that cannot be completely removed, and, as a result, increase of temperature. This situation generates parasitic reactions between the electrolyte and the electrodes, and the worst consequence is represented by thermal runaway, with the rupture of the battery and its explosion [13].

New battery technologies are necessary to overcome LIBs problems and to substitute them where this is possible.

2 Potassium-ion batteries (KIBs)

2.1 Comparative analysis of KIBs, LIBs and NIBs characteristics

KIBs and NIBs are the main candidates to replace LIBs. It is clear that the latter cannot be replaced in applications where high energy density and low weight are required at the same time [Figure 2.1], such as portable electronics and electric vehicles. Research and development are thus moving towards stationary storage, for which gravimetric density is not a fundamental requirement.
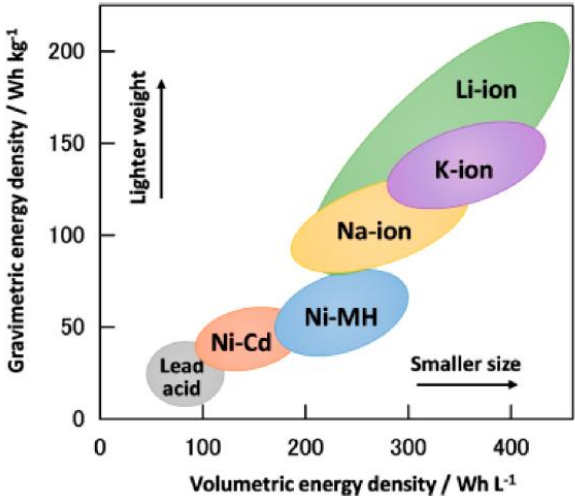
Figure 2.1: Gravimetric and volumetric energy densities of different EES systems [12].

LIBs, KIBs and NIBs have a common working principle, called "rocking chair": the alkaline positive ions move back and forth between the anode and the cathode, through the electrolyte, while the electrons always flow in the external circuit [Figure 2.2].
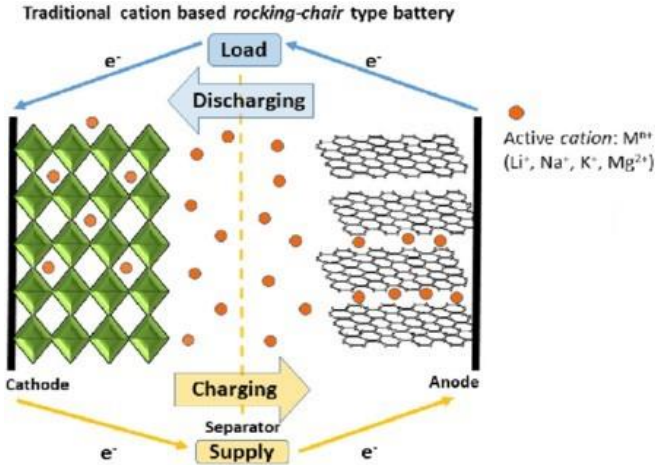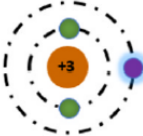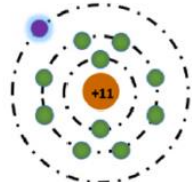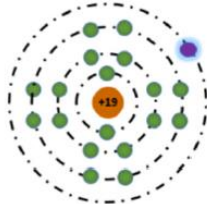
Figure 2.2: Schematic representation of the "rocking chair" working principle [14].

Potassium and sodium are far more abundant than lithium: they represent 1.5 wt% and 2.3 wt% of the Earth crust, respectively, with a relatively homogeneous global distribution. These features explain their lower cost, and hence the interest in their exploitation. The cost of a KIB can be further lowered substituting copper collectors with cheaper aluminum ones: this is possible because potassium, unlike lithium, does not form alloys with aluminum. The standard reduction potential of K^+/K (-2.93 V vs. standard hydrogen electrode [SHE]) is similar to that of Li^+/Li (-3.04 V vs. SHE) and more negative than that of Na^+/Na (-2.71 V vs. SHE), resulting in the possibility to obtain a higher energy density in KIBs than in NIBs. Potassium ions have the largest atomic radius and the weakest Lewis acidity and these characteristics lower their desolvation energy in carbonate solvents, resulting in a smaller Stokes radius if compared to Li^+ and Na^+. The main consequences are the higher diffusion coefficients of K^+ and the faster ionic transportation in organic electrolytes [15], which possibly allow high power systems. An overall comparison between the three alkaline metals is shown in Table 2.1.

Table 2.1: Comparison of lithium, sodium and potassium properties.

Properties	Lithium	Sodium	Potassium
Atomic structure			
Atomic number	3	11	19
Atomic mass	6.941	22989	39.098
Electronic configuration	[He] $2s^1$	[Ne] $3s^1$	[Ar] $4s^1$
Abundance in earth crust [wt%]	0.0017	2.3	1.5
Global distribution	Mostly in South America	Everywhere	Everywhere
E^0 vs. SHE [V]	-3.04	-2.71	-2.93
Atomic radius [Å]	145	180	220
Stokes radius [Å] in PC	4.8	4.6	3.6
Cost of carbonate [\$ ton^{-1}]	6500	200	1000
Cost of metals [\$ ton^{-1}]	100 000	3000	13 000

2.2 Potassium-ion batteries brief history

Research on KIBs started in 1954, when Rudorff and Schultze discovered the first potassium intercalation compound, based on graphite. The initial studies on the intercalation chemistry of K^+ ions took place in 1970s and 1980s, starting with Prussian Blue; until that moment, R&D was focused on Li^+ and Na^+, due to their smaller atomic radius and weight [15]. The first KIB prototype was designed only in 2004 by Ali Eftekhari, who employed a metallic potassium anode, a Prussian Blue cathode and an organic electrolyte (1 M KBF_4 in ethylene carbonate (EC):ethyl-methyl carbonate (EMC) 3:7). This cell shows some interesting advantages compared to LIBs and NIBs, such as simple design, cheap components materials and a cyclability of more than 500 reversible cycles [16]. In 2007, the Chinese company Stairsway Electronics commercialized the first portable media-player powered by a KIB, but they did not provide any information about the new product [17]. In the following years, battery research focused its efforts on LIBs and NIBs; then, in 2014 KIBs came again to R&D attention and the number of publications increased year after year [Figure 2.3]. Subsequently, 2015 represented the turning point for KIBs: Komaba et al. and Ji et al. demonstrated the electrochemical intercalation of K^+ ions in graphite, using KPF_6 dissolved in EC and diethyl carbonate (DEC) (0.8 M KPF_6 in EC:DEC 1:1) [18,19]. In the following years, many other intercalation anode materials were investigated, as well as alloying and conversion ones, and research also focused on suitable cathode materials and electrolytes. The current results confirm the KIBs potential to replace LIBs in several fields.
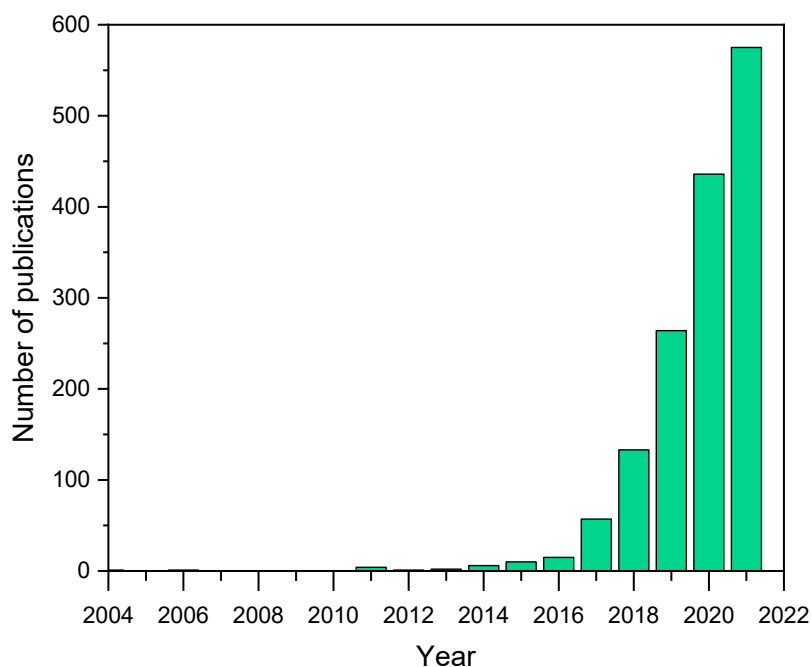
Figure 2.3: Number of publications on KIBs from 2004 to 2021 (obtained from Scopus).

2.3 Potassium-ion batteries configuration

The usual main components of a KIB are the anode, the cathode and the electrolyte. The two electrodes are separated by the electrolyte, the principal functions of which are to allow the transportation of ions and to hinder the flow of electrons, which would cause short-circuit. KIBs follow the "rocking chair" working principle [Figure 2.4], as previously mentioned. The reversible charge/discharge process is based on the alternative migration of K^+ ions from one electrode to the other, while the electrons flow in the external circuit. During the discharge process, K^+ ions de-intercalate from the anode, which hosts the oxidation reaction, and intercalate into the cathode, where they combine with the electrons coming from the external circuit and represent the reduction reaction. The charge process is the opposite one, with the K^+ ions moving from the positive electrode to the negative one, as a result of the application of an external electric current.
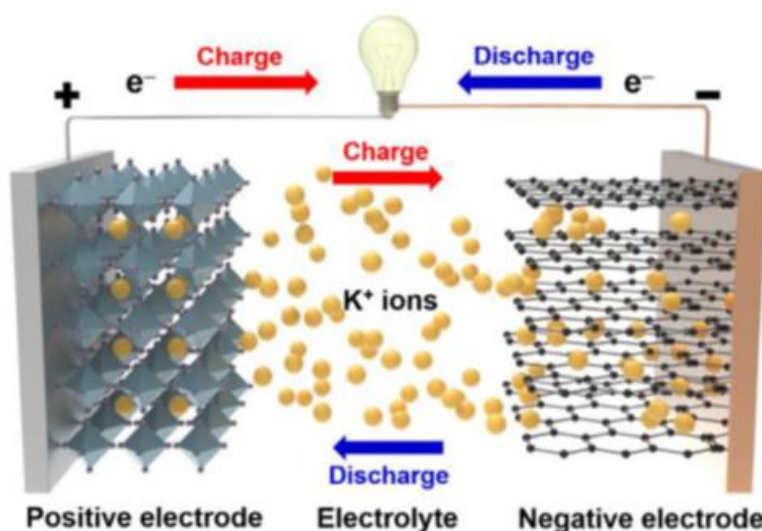
Figure 2.4: KIB standard configuration [20].

2.3.1 Anodic materials

The anodic material is a critical component in KIBs, as it determines the energy density, the cycle life and the voltage of the cell. Pure potassium metal has the highest energy density and specific capacity, but despite this it is not suitable for future commercial batteries: its main disadvantages are the high reactivity to water and oxygen and the growth of dendrites. Therefore, research is focusing on alternative materials, considering the larger radius of K^+ ions compared to lithium and sodium ones. This aspect leads to different interactions with the same anode: if employed in KIBs, each anodic material would show a lower capacity, a lower stability and larger volume variations during intercalation and deintercalation. Advanced structure design and mechanism studies are necessary to improve performances.

Based on the K^+ ions storage mechanism, the anodic materials are classified into four categories: intercalation materials, conversion materials, alloys and organic materials [21].

Intercalation compounds

Graphite

One of the most successful materials exploited for LIBs anodes is graphite, thanks to its several advantages, *i.e.* low cost, low volume variation during the intercalation/de-intercalation process, high specific capacity and stability. Hence, it represents a feasible anodic material also for KIBs, considering lithium and potassium similarities. The two alkali metal ions, indeed, are able to intercalate and de-intercalate from the graphite layered structure, forming graphite intercalation compounds (GICs). In 2015, Ji et al. and Komaba et al. discovered K^+ ion intercalation in graphite, with the formation of stage I KC_8 GIC. Subsequently, other potassium intercalation GICs were discovered, such as stage III KC_{36} and stage II KC_{24}; the stage number indicates the number of layers that separate two intercalated K^+ ions [Figure 2.5].
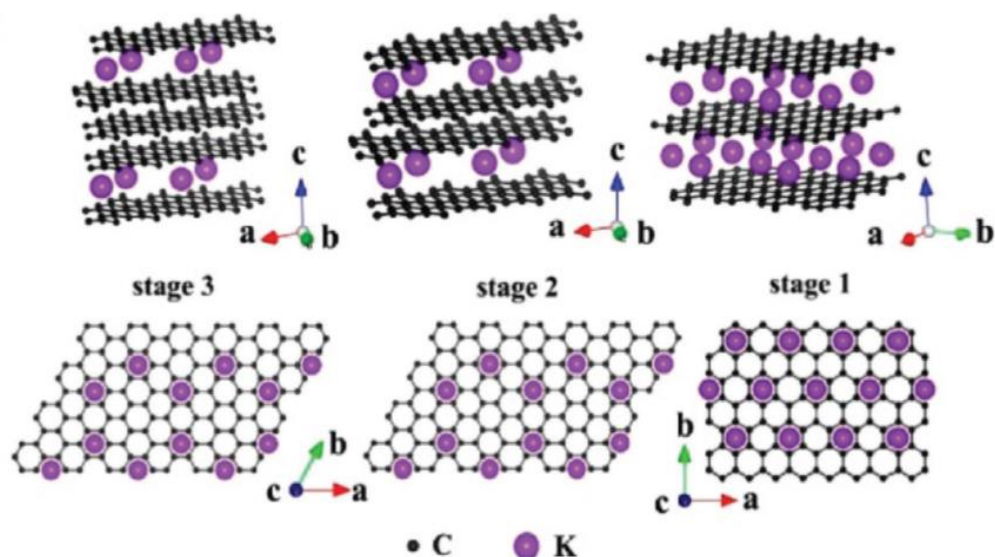
Figure 2.5: Structures of different K-GICs, side view (top row) and top view (bottom row) [22].

The different stages are formed during the potassiation process at specific voltage ranges: KC_{36} is first detected between 0.3-0.2 V, KC_{24} between 0.2-0.1 V and eventually KC_8 near 0.01 V. Considering K-extraction, stage II is not observed; KC_8 is directly converted into KC_{36} at ≈0.3 V and K-free graphite is obtained above 0.5 V. This behavior suggests the presence of some differences in the reaction mechanism during intercalation and de-intercalation [22].

The reversible capacity of graphite anodes has been evaluated using potassium metal as cathode and 0.8 M KPF_6 in EC:DEC 50:50 as electrolyte, at a C/40 rate: the obtained value of 273 mAh g^{-1} is close to the theoretical capacity of 279 mAh g^{-1} for the formation of KC_8. Unfortunately, the capacity considerably decreases with higher current rates [23]. Moreover, graphite is affected by a volume variation of more than 60% during the intercalation/de-intercalation process, that causes cycling instability [15]. The commercial application of graphite as KIBs anode requests some improvements, concerning the reduction of volume variations and the increase of active sites to improve specific capacity.

Amorphous carbons

Unlike graphite, amorphous carbons do not show a crystalline structure, but a disordered one. The presence of random graphite domains in an amorphous structure increases the ion conductivity and reduces the volume variations during the ions intercalation/de-intercalation process. Amorphous carbons include hard carbon (HC), soft carbon (SC), hard carbon-soft carbon composite (HCS-SC) and others. Most non-graphitic forms of carbon are characterized by high capacity and cycling stability, and the best performances are shown by the composite HCS-SC, which consists of 20 wt% SC distributed in a matrix-phase of HC microspheres.
An effective strategy to increase amorphous carbons capacity is heteroatom doping, particularly with nitrogen, sulfur and phosphorus [15,20].

Inorganic intercalation anodes

Another class of intercalation anodes is constituted by inorganic materials, the main advantages of which are a low potassiation potential, low cost and low toxicity. Among many compounds, the most representative ones are titanium-based oxides, such as $K_2Ti_8O_{17}$, $K_2Ti_4O_9$ and $K_2Ti_6O_{13}$. Inorganic intercalation anodes are promising anodes for KIBs, but their capacities are lower if compared with graphite and amorphous carbons. Nonetheless, their performances can be boosted by structural modification and defect addition [15].

Conversion compounds

Conversion anodes are based on reactions involving their lattice atomic species, that lead to the formation of one or more new compounds and to the hosting of the alkali metal.
The general reaction mechanism is described by the following equation:

$$M_xA_y + (yn)K^+ + (yn)e^- \leftrightarrow xM + yK_nA \quad (2.1)$$
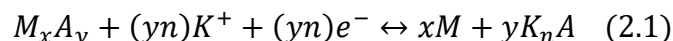
where M is a transition metal, X is a non-metal anion (O, S, F, *etc.*) and n is the anion oxidation state. Conversion anodes can be classified into different groups, based on the nature of the non-metal anion involved: oxides, phosphides and sulfides (selenides).
Most of the conversion anodes show a higher theoretical capacity if compared to intercalation materials, but several issues must be solved to allow the commercialization of conversion materials as KIBs anodes. They are characterized by low cycling stability, high polarization upon charge-discharge, huge volume variations and low values of Coulombic efficiency [24].

Alloying compounds

The elements of Groups IVA and VA (Si, P, Sn, Sb, Pb, *etc.*) are able to alloy with potassium, when a potential is applied. Alloys are reversibly generated during the charge process, when K^+ ions insert into the anode and form new compounds with its elements. The general reaction mechanism is described by the following equation:

$$xA + yK^+ + ye^- \leftrightarrow K_yA_x \quad (2.2)$$
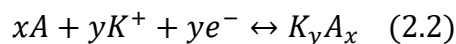
where A is the element that alloys with potassium and K_yA_x is the final alloying product.

This kind of anodes has raised interest in KIBs applications because of the low operating voltage and high theoretical specific capacity. As an example, K_3Sb, which is the final alloying product of Sb and K, used as anode material can provide a theoretical capacity of 660 mAh g^{-1}. The main drawback consists in the large volume variations that occur during the potassiation and de-potassiation: as consequences, the capacity decreases rapidly after some charge/discharge cycles and both the anode surface and the solid electrolyte interface (SEI) are subject to pulverization. Some innovative strategies to solve these problems include the use of new-designed nanostructures and of protective coatings for the anode surface [24].

Organic compounds

Some organic compounds have been recently highlighted as suitable anodic materials. They include simple organic molecules, metal-organic frameworks (MOF), covalent organic frameworks (COF) and polymers. They are mainly characterized by low cost, low weight, controllable properties, easy synthesis, non-toxicity and renewability.

Organic compounds molecules interact with Van Der Waals forces and they consequently have large inter-planar regions that can host big ions, such as potassium ones.

Recent studies analyzed potassium terephthalate (K_2TP) and potassium 2,5-pyridinedicarboxylate (K_2PC) as KIBs anodes: both these materials are para-aromatic dicarboxylate salts and they can reversibly host K^+ ions [Figure 2.6]. The specific capacities are 181 mAh g^{-1} for K_2TP and 190 mAh g^{-1} for K_2PC, respectively; the latter shows a better performance mainly because of the presence of the pyridine ring, which has a higher electron compatibility [25].
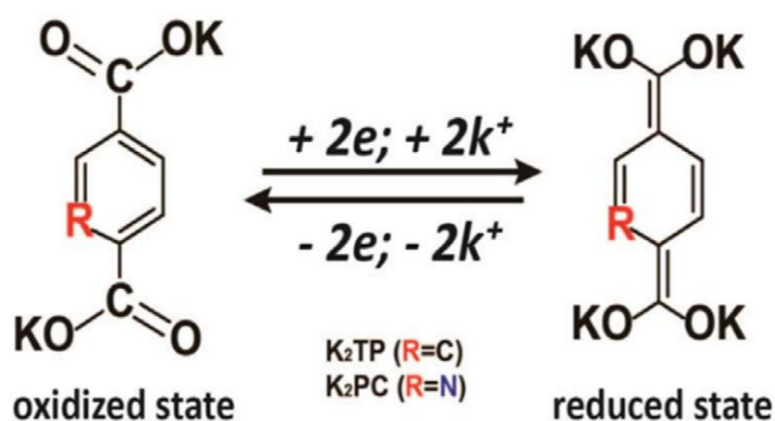
Figure 2.6: The electrochemical mechanism of K_2TP and K_2PC in KIBs [25].

Organic materials are promising anodes for KIBs, but further improvements must be achieved to allow their commercialization. The main drawbacks are currently the low conductivity and the high solubility in aprotic electrolytes.

2.3.2 Cathodic materials

The cathode determines the energy density of the cell. Unlike anodic materials, in which potassium can be stored with different mechanisms, in cathodes K^+ ions are only hosted through intercalation. The cathodic material must own large sites or spaces in its lattice, that can reversibly store potassium ions: these features are required to obtain high capacities and good cycle stability.

The research on cathodic materials is mainly addressed on four different categories: layered transition metal oxides (TMOs), metal hexacyanoferrates (Prussian Blue and analogs), polyanionic compounds and organic compounds.

Layered transition metal oxides (TMOs)

Layered TMOs have the general chemical formula A_xMO_2, where A represents the alkali metal (Li, Na, K) and M is a transition metal, such as Fe, Mn, Co, *etc.* The usual layered transition metal oxides notation includes a letter, that represents the alkali metal phase, such as edge-sharing octahedral (O) or face-sharing prismatic (P), and a number, that indicates the periodicity of the stack. According to their stacking order, these oxides are classified into three main groups: O3-type, P3-type and P2-type, as shown in Figure 2.7.
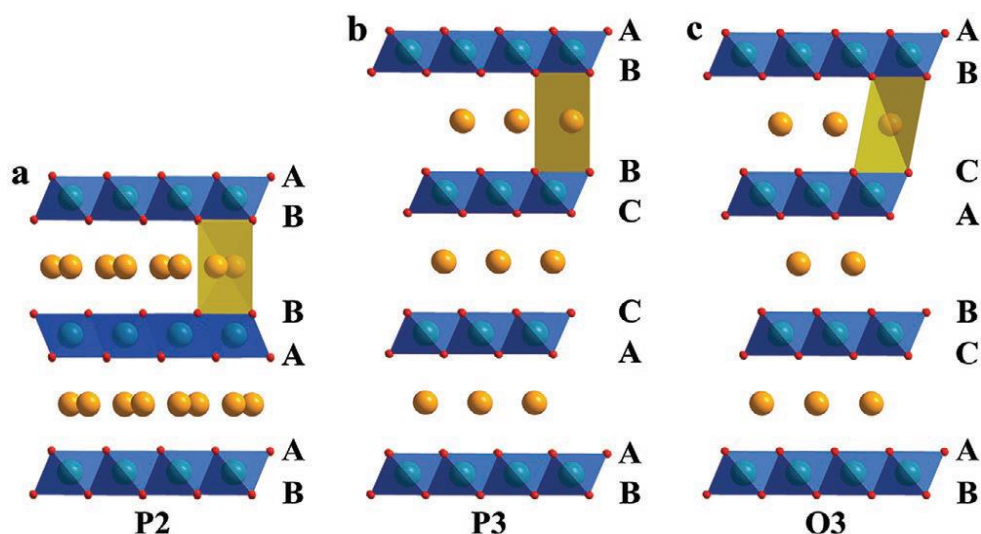
Figure 2.7: Schematic illustration of the crystal structures of P2, P3 and O3 layered TMOs [28].

The following equation describes the reaction mechanism of K^+ and TMOs:

$$K_{1-x}MO_2 + xK^+ + xe^- \leftrightarrow KMO_2 \quad (2.3)$$
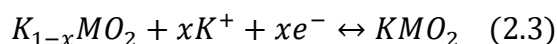
Layered TMOs are commonly used as LIBs and NIBs cathodes, due to their simple synthesis, high theoretical capacity and energy density, low cost. Recently, they have been proved to be suitable materials also for KIBs cathodes. Kim et al. synthesized a layered P3-type $K_{0.5}MnO_2$ that shows a stable capacity of ≈ 100 mAh g^{-1} [26], but the material is characterized by structure

transitions and volume changes during the K^+ ions intercalation and de-intercalation. The main consequences are irreversible framework deformations and rapid capacity fading. Some potential strategies to improve layered TMOs performances include doping, coating and the design of nano-porous structures [24, 27, 28].

Prussian Blue (PB) and analogs (PBAs)

Transition metal hexacyanoferrates include Prussian Blue (PB) and its analogs (PBAs), the structure of which is stable and owns a high number of active sites. Their general chemical formula is $A_xM[Fe(CN)_6] \cdot yH_2O$, where A represents the alkali metal and M is a transition metal (*e.g.* Mn, Fe, Co).

Typically, PB and its analogs possess a face centered cubic (FCC) crystal structure [Figure 2.8], in which the octahedral MN_6 and FeC_6 are alternatively linked together through the organic cyanide (CN) groups. The structure is a 3D open framework, with channels and large void spaces, that can host K^+ ions.
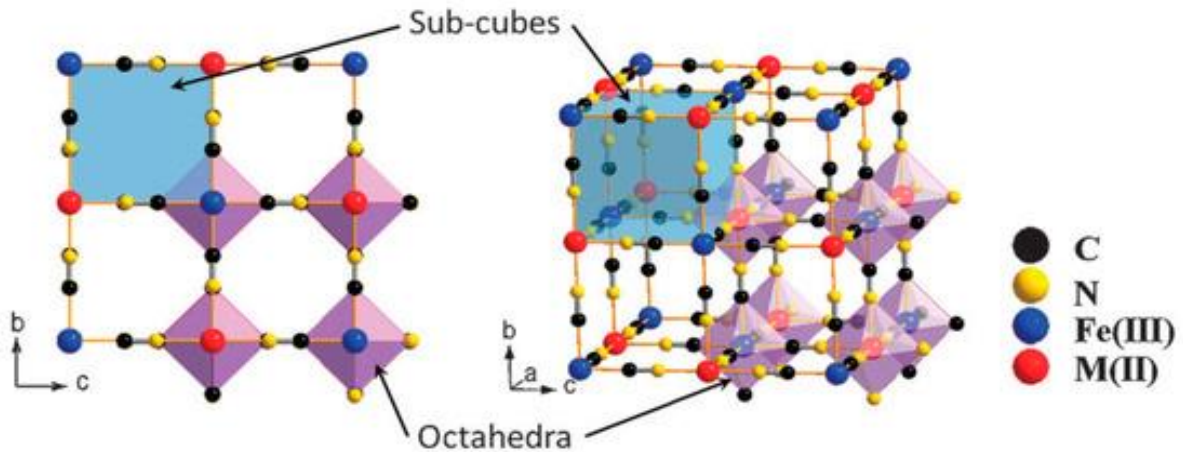
Figure 2.8: Schematic illustration of PBAs crystal structure [17].

Considering PB, the K^+ intercalation/de-intercalation process is described by the following equations:

$$K_2Fe^{II}[Fe^{II}(CN)_6] \, (PW) \leftrightarrow KFe^{III}[Fe^{II}(CN)_6] \, (PB) + K^+ + e^- \quad (2.4)$$

$$KFe^{III}[Fe^{II}(CN)_6] \, (PB) \leftrightarrow KFe^{III}[Fe^{III}(CN)_6] \, (BG) + K^+ + e^- \quad (2.5)$$
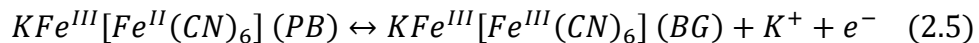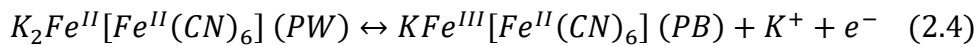
During the charge/discharge cycles, PB undergoes two different reactions: the oxidation into Berlin Green (BG) and the reduction into Prussian White (PW) [29]. The rigid PB cathode structure shows low volume changes during potassiation and de-potassiation, with high ions transportation rate, due to the presence of large channels, and very high cycling stability. Nevertheless, the commercialization requests the improvement of some issues, such as the hosting of undesired interstitial water and low conductivity [30].

Polyanionic compounds

Polyanionic compounds are promising cathodic materials: they possess a rigid and stable 3D framework, that hinders large volume and structure changes during the K^+ ions intercalation and de-intercalation process. Moreover, these materials show good cycle stability and ionic conductivity; they can deliver a high potential, up to 4.2 V *vs.* K^+/K, and they consequently display high energy densities [26].

Polyanionic materials are described by the general chemical formula $AM_x[(XO_4)]_y$, where A is an alkali metal, M is a transition metal (Fe, V, Ti, Mn, *etc.*) and X is the non-metal element, such as P, S and Si. The tetrahedron anion units $(XO_4)^{n-}$ are connected to the MO_x polyhedra with strong covalent bonds; they stabilize the lattice and form an open channel structure, that facilitates the diffusion of K^+ ions [29].

$LiFePO_4$ is one of the most successful cathodic polyanionic compounds for LIBs. Therefore, $KFePO_4$ has been taken in account as host for K^+ ions, as it shares a similar lattice structure with $LiFePO_4$. Recent research is also focusing on vanadium-based and titanium-based polyanionic compounds [28].

Organic compounds

Organic materials have been extensively used as alkali metal ion battery anodes, and some of them have also been reported as promising cathodic materials. Their main characteristics and drawbacks have been displayed in section 2.2.1, describing the application as KIBs anodic materials.

Recently, the organic pigment 3,4,9,10-per-tetracarboxylic acid-dianhydride (PTCDA) has been tested for KIBs by Chen et al., observing good cycle stability and capacity retention. The material shows a specific capacity of 131 mAh g^{-1} in the voltage range 1.5–3.5 V (*vs.* K^+/K) [22], with the hosting of two K^+ ions per PTCDA molecule [Figure 2.9].
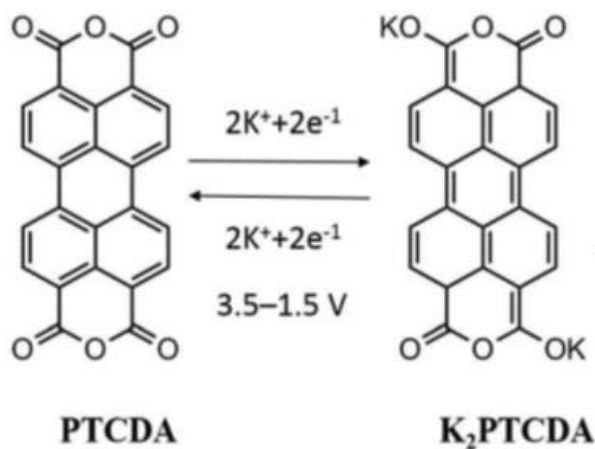
Figure 2.9: Schematic illustration of the structure and electrochemical mechanism of PTCDA [22].

2.3.3 Collectors

The electrode active material is deposited on a collector, that ensures mechanical support. Its main role is to promote the electrons flow into the external circuit; furthermore, collectors must possess a high corrosion resistance, low weight and good mechanical stability. Copper and aluminum can be employed as KIBs collectors, and the second one is preferred because of its cheapness. Aluminum cannot be used as anode collector in LIBs, since at low potential it alloys with lithium, unlike potassium.

3 Electrolytes

KIBs electrochemical performances are largely dependent on the electrolyte nature, and the electrodes show different behaviors if coupled with different electrolytes.

The main electrolyte aim is to connect the electrodes, allowing the ions transportation and hindering the electrons flow, avoiding short-circuits. Furthermore, the electrolyte is a critical component, as it determines several battery properties, such as internal resistance, thermal stability, deliverable energy density and cycle life. It also has a determining role in the formation and composition of the SEI layer.

KIBs electrolytes are classified into two main categories: liquid and solid. Liquid electrolytes can be further divided into aqueous, organic and ionic liquids (ILs), while solid state electrolytes (SSEs) include inorganic and polymeric ones. Each group possesses peculiar properties, as shown in Figure 3.1, that will be illustrated in sections 3.1 and 3.2.
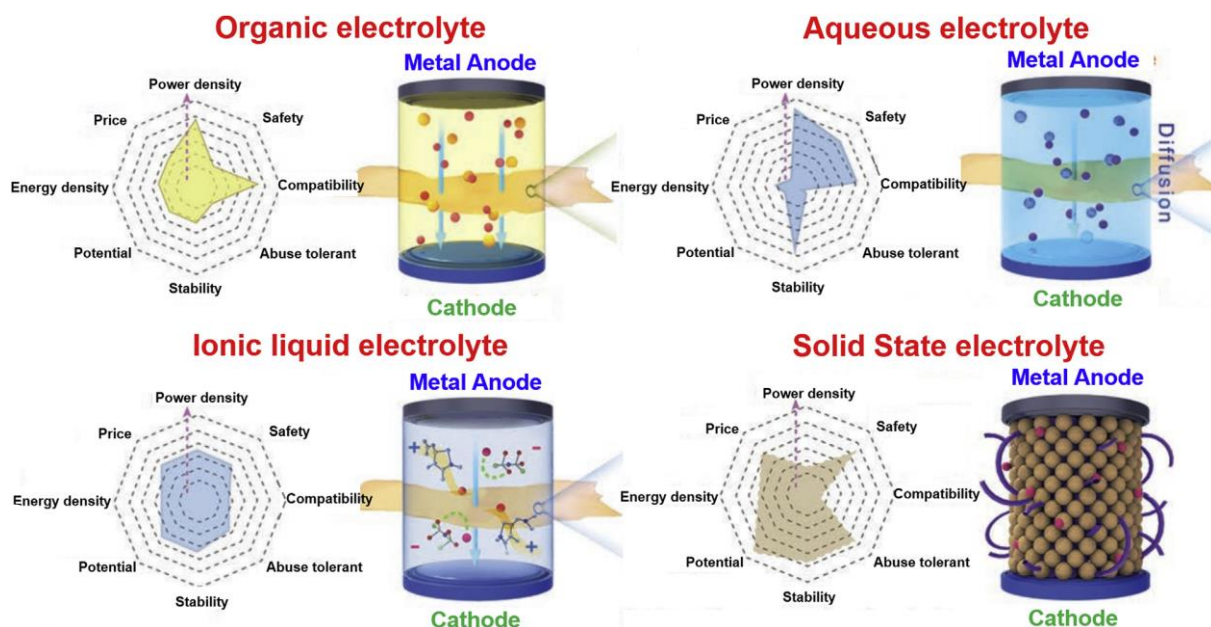
Figure 3.1: KIBs electrolytes properties and structures [32].

The key features that should be considered while selecting electrolytes for battery applications are:

- high ionic conductivity;
- electrochemical and chemical stability;
- adequate interface contact;
- high thermal stability;
- non-toxicity, eco-friendliness and low cost [Figure 3.2].
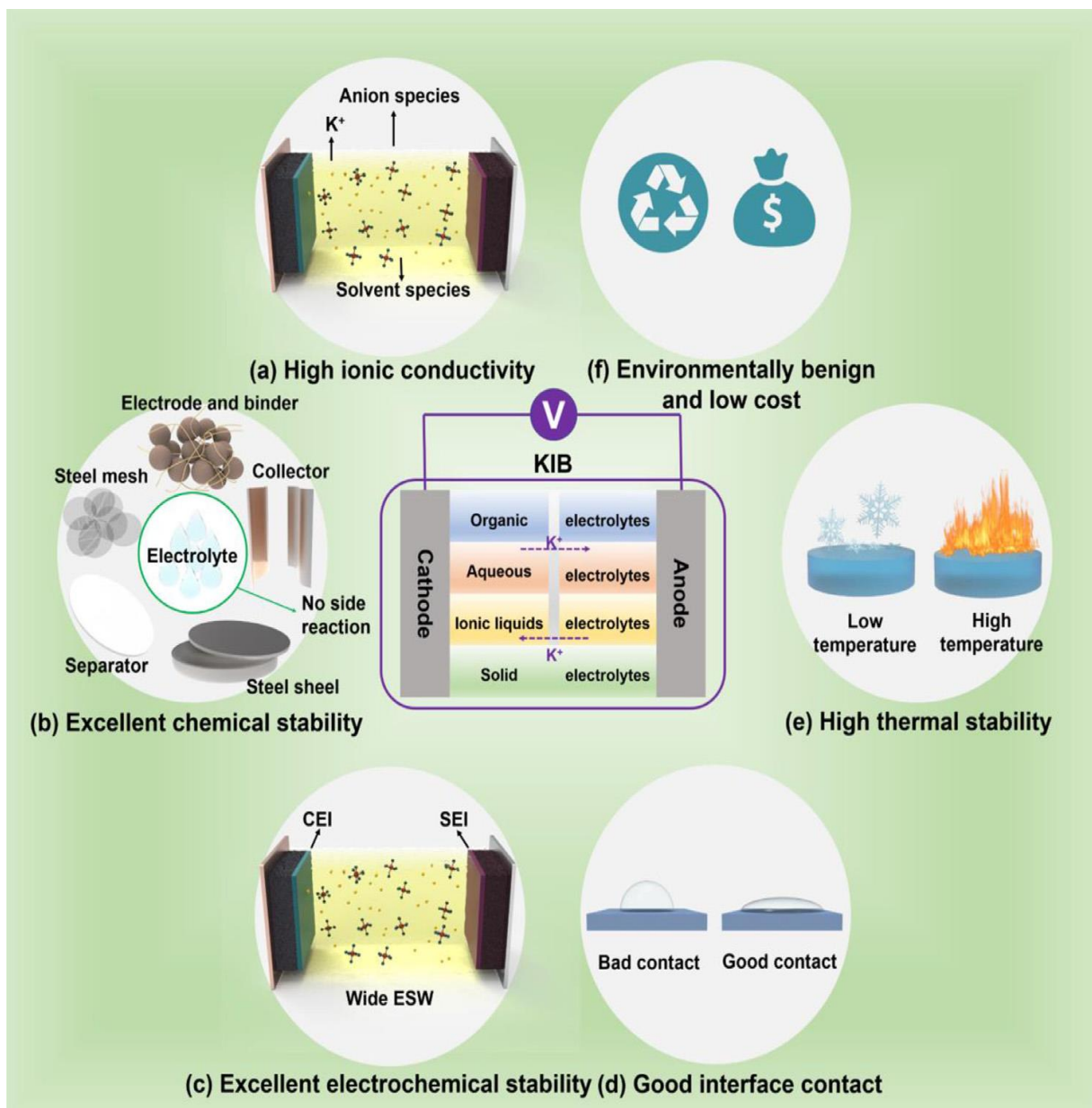
Figure 3.2: The main properties required for KIB electrolytes: (a) high ionic conductivity, (b) chemical stability, (c) electrochemical stability, (d) interface contact, (e) thermal stability (f) non-toxicity, eco-friendliness and low cost [20].

Ionic conductivity

A proper electrolyte is characterized by high ionic and low electronic conductivities. Considering liquid electrolytes, the ionic conductivity principally depends on the dissociation energy of the salt: compared to Li^+ and Na^+, K^+ ions show the lowest dissociation energy due to their larger ionic radius. A lower desolvation energy results in lower solubility into the solvent, but also in faster ionic transportation and hence in higher ionic conductivity.

Furthermore, the ionic conductivity follows a parabolic trend with the increase of the salt concentration into the solvent: it initially increases, due to the high free ions availability, then

it starts decreasing, because of electrostatic interference. Lastly, also viscosity influences the ionic conductivity: the latter is inversely proportional to the electrolyte viscosity.

Chemical and electrochemical stability

A proper KIB electrolyte should not react with any other cell component, *i.e.* it must be chemically stable and compatible with the other battery constituent materials. Furthermore, a wide electrochemical stability window (ESW) is a major requirement for a suitable electrolyte, since it allows to operate into a wider potential range, in order to obtain a high energy density. Furthermore, the formation of stable electrode/electrolyte interfaces can ensure a long cycle life for the battery. To conclude, the electrolyte stability voltage range must be larger than the battery working voltage range, to avoid undesired reactions.

Interface contact

An adequate interfacial contact between the electrodes and the electrolyte surfaces is mainly necessary to reduce the ionic transfer resistance. Moreover, a proper contact can guarantee a homogeneous SEI, which may prevent the dendrites nucleation. Good adhesion is usually obtained by liquid electrolytes, while solid electrolytes show poor contact and, hence, higher resistance. Even so, SPEs can work as dendrites suppressors: their high mechanical properties suppress the dendrites growth, which otherwise would cause short-circuits.

Thermal stability

Thermal stability is extremely important, considering that the electrolyte can be the most flammable part of the battery and hence it determines its safety. The thermal stability range is set by the electrolyte freezing and boiling points, and it must include the operating temperature range of the battery, in order to avoid huge volume changes, ruptures, leakages and explosions. Flame-retardant components or solvents can be utilized to further increase the battery safety; however, the decomposition of K salts usually happens at higher temperatures if compared to Li and Na salts [20].

3.1 Liquid electrolytes

A common liquid electrolyte is made up of a salt or a mixture of salts, dissolved in one or more suitable solvents. They must be compatible with each other and with both electrodes; the solution is decisive in determining the cell performances and behavior.

3.1.1 Ionic liquid (IL) electrolytes

IL electrolytes are promising KIBs electrolytes, mainly because of their capability to withstand high voltages and their wide ESW. In addition, they are characterized by high temperature stability, low flammability and volatility, high ionic conductivity; therefore, they can be

considered safer if compared to the most used organic electrolytes. The main disadvantages include high cost and high viscosity, but the last property can be improved by working at high temperatures [31].

ILs consist of a mixture of inorganic or organic anions and organic cations, that exhibit a liquid form at room temperature. Until now, ILs have been employed and tested as KIBs electrolytes only in a few studies, including imidazolium, pyrrolidinium, ammonium and sulfonium as cations, tetrafluoroborate (BF_4^-), bis(trifluoromethanesulfonyl)imide ($TFSI^-$) and bis(fluorosulfonyl)imide (FSI^-) as anions.

Nohira et al. investigated KFSI-Pyr_{13}FSI properties as IL electrolyte in KIBs. It exhibits an ionic conductivity of 4.8 mS cm^{-1} at a KFSI molar ratio of 0.20 at 298 K. In addition, it stands to higher potential values (5.72 V) if compared to the equivalent Na-IL (5.42 V) and Li-IL (5.48 V). Considering TFSI, Masese et al. tested KTFSI-Pyr_{13}TFSI: they detected an electrochemical window of more than 6 V, confirming the promising ILs application as high voltage electrolytes [20].

3.1.2 Aqueous electrolytes

Non-flammability is the aqueous electrolytes main feature, that nominates them as promising materials for grid applications. Aqueous electrolytes also show many other advantages, if compared to ILs and organic electrolytes: high conductivity, low cost, sustainability and eco-friendliness, stability in air. Furthermore, they are particularly suitable for organic electrodes, because of the low solubility of organic compounds in water-based solvents.

The usually employed solutes are potassium nitrate (KNO_3), potassium sulphate (K_2SO_4), potassium chloride (KCl) and potassium hydroxide (KOH). Considering standard salt concentrations, the principal drawback is represented by the narrow ESW, between 0 and 1.23 V: outside the stability range, water undergoes splitting into oxygen and hydrogen, with gas accumulation and safety issues.

Recently, a suitable solution was found with the so-called "*water-in-salt*" (WIS) electrolytes: they are characterized by an extremely high salt concentration, which avoids water dissociation from 0 V up to ≈3 V. The increase in concentration goes along with the cost increase, partially neutralizing the aqueous electrolytes low cost advantage. Future studies should be focused on more soluble and cheaper salts, and on additives able to stabilize water in a wider potential range [32].

3.1.3 Organic electrolytes

Organic electrolytes have been widely employed in LIBs due to their several favorable features, that make them promising electrolytes also for KIBs. They show high ionic conductivity, low cost and low viscosity; furthermore, they are compatible with many different electrode materials, proving to have a wide voltage stability window and to form stable SEI layers. Unfortunately, these electrolytes lack in safety, due to their high flammability and high

reactivity with metallic potassium. Research is thus moving towards the development of suitable flame-retardant additives and new non-flammable solvents [32].

As those employed in LIBs, organic liquid electrolytes are composed by:
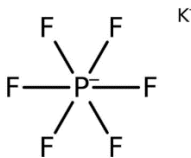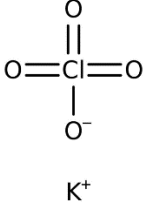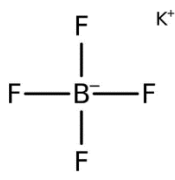
- one or more solvents, combined to obtain specific features and performances;
- one salt dissolved in the solvent (recently, also binary-salts have been tested);
- one or more additives, used to improve some critical characteristics.
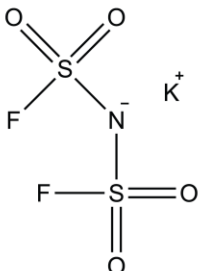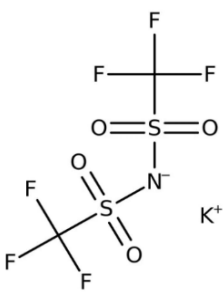
The electrolyte stability depends on the solvents and salts themselves, but also on their interaction, which affects, as a consequence, the whole battery performance.

Salts

The salt directly influences the electrochemical properties of the electrolyte. Potassium salts commonly employed in organic liquid electrolytes include KPF_6, $KClO_4$, KBF_4, potassium bis(fluorosulfonyl)imide (KFSI) and potassium bis(trifluoromethanesulfonyl)imide (KTFSI). The solubility in organic solvents is quite low for $KClO_4$ and KBF_4; for this reason, the research is focused on KPF_6, KFSI and KTFSI, that show higher solubilities and thus higher concentrations in organic solvents. Their main features are presented in Table 3.1.

Table 3.1: Physical and chemical properties of potassium salts for KIB organic electrolytes [20].

Salt	Chemical structure	Decomposition temperature [°C]	Conductivity [mS cm⁻¹]	Solubility	Cost	Toxicity
KPF_6		575	5.75	0.9 mol kg^{-1} in PC; 1.8 mol kg^{-1} in dimethoxy ethane (DME)	Low cost	Low toxicity
$KClO_4$		610	0.2	Hardly dissolved in PC	Low cost	High toxicity
KBF_4		530	1.1	Hardly dissolved in PC	High cost	High toxicity

KFSI	102	7.2	10 mol kg^{-1} in PC; 7.5 mol kg^{-1} in DME	High cost	Nontoxic
KTFSI	198-203	6.1	6 mol kg^{-1} in DME	High cost	Nontoxic

KPF_6-based electrolytes have been widely investigated in KIBs; they are characterized by high ionic conductivity and low cost, and PF_6^- anions own the capacity to passivate the aluminum collectors. Still, KPF_6 practical applications are possible by overcoming some limits: a general KPF_6-based electrolyte shows large irreversible capacity and low Coulombic efficiency, but some improvements have been achieved with appropriate solvent choices. Indeed, higher Coulombic efficiency and better cycling stability were obtained employing the solvent mixture EC:propylene carbonate (PC) instead of EC:DEC and EC:dimethyl carbonate (DMC), that show worse performances [32]. Another KPF_6 disadvantage is its high reactivity to water and oxygen, with the formation of toxic compounds such as HF, PF_5 and POF_3.

The imides KFSI and KTFSI have been proposed as KPF_6 replacement: they show higher conductivities in PC solvent, allow the formation of more stable SEI layers and hinder the growth of dendrites. Nevertheless, FSI^- and $TFSI^-$ anions cause aluminum corrosion, damaging the Al collectors at high voltages.

Recently, a binary-salts electrolyte was developed by Komaba et al.: it is based on the couple KPF_6-KFSI and it shows a higher ionic conductivity and higher capacities if compared to simple KPF_6-based electrolytes [20].
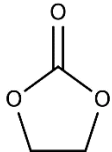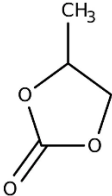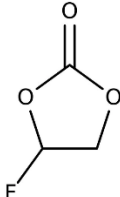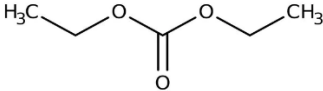
Solvents

The solvent is the second major component of an organic electrolyte and it strongly affects the cell performances. Organic solvents employed in LIBs and KIBs are mainly esters and ethers; their main features are shown in Table 3.2.
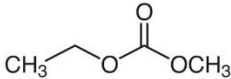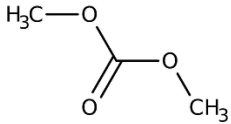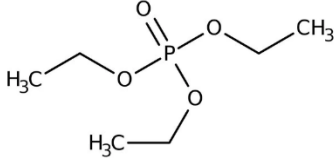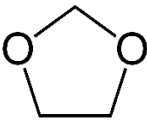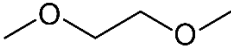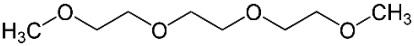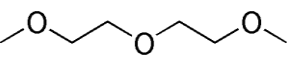
Ester-based solvents are linear or cyclic carbonates; they possess a high electrochemical stability and K-salts show high solubilities towards them. Some commonly used esters are the cyclic EC, PC and fluoroethylene carbonate (FEC), and the linear DEC, EMC, DMC and triethyl phosphate (TEP). Despite its tendency to cause an unstable SEI layer, the EC:DEC mixture remains one of the most studied solvents, thanks to its incredibly wide ESW.

Ether-based solvents show high ionic conductivities, they can reach higher salt concentrations if compared to esters and form stable SEI layers. They include the cyclic 1,3-dioxacyclopentane (DOL), the linear DME, triethylene glycol dimethyl ether (TEGDME) and diethylene glycol dimethyl ether (DEGDME). Among these solvents, DME is the most studied, because it leads to the formation of stable and robust SEI layers, which provide high Coulombic efficiency and electrodes protection.

Table 3.2: Physical and chemical properties of organic solvents [20].

Properties	Melting point [°C]	Melting point [°C]	Boiling point [°C]	Viscosity at 25 °C [cP]	Density at 25 °C [g mL^{-1}]
EC		36.4	248	2.10	1.32
PC		-48.8	242	2.53	1.20
FEC		18	249	2.35	1.45
DEC		-74.3	126	0.75	0.98

EMC		-53	110	0.65	1.01
DMC		4.6	91	0.59	1.07
TEP		-56.4	215	1.60	1.07
DOL		-95	75.6	0.60	1.06
DME		-58	84	0.46	0.87
TEGDME		-46	216	3.39	1.01
DEGDME		-64	162	1.06	0.94

Additives

Electrolyte additives are used in very small quantities in the electrolyte, effectively improving the battery performances and modifying specific properties, such as the SEI layer composition

and stability; they can also reduce the electrolyte viscosity, improve salts solubility and act as flame-retardant.

Many additives have been employed in LIBs and NIBs with excellent results; the most relevant is FEC, the influence of which has been recently studied also for KIBs. FEC was tested with EC:DEC, showing an increase in the Coulombic efficiency, especially with PBA cathodes; nevertheless, it favors the occurrence of side reactions that reduce the stability and cycle life of the battery [33]. Furthermore, FEC, but also difluoroethylene carbonate (DFEC) and vinylene carbonate (VC), were demonstrated to increase the battery polarization, and hence to worsen the plating and stripping process. Further studies could lead additive mixtures to achieve better results [20].

3.2 Solid state electrolytes (SSEs)

The use of liquid electrolytes as KIBs components for practical application is hindered by several issues, mainly related to the battery safety. Therefore, the research is shifting towards the new SSEs that are regarded as a suitable future replacement for liquid electrolytes, due to some relevant advantages. They are characterized by non-flammability, thermal and mechanical stability, environmental friendliness; furthermore, they can suppress the dendrites growth, while offering a wider ESW and hindering the organic electrodes dissolution. These features increase the battery safety and its electrochemical performances [34].

SSEs are primarily classified into inorganic solid electrolytes (ISEs) and polymer electrolytes (PEs). The PEs category includes solid polymer electrolytes (SPEs), gel polymer electrolytes (GPEs) and composite polymer electrolytes (CPEs).

3.2.1 Inorganic solid electrolytes (ISEs)

ISEs have been applied in sodium-sulfur batteries (NSBs) since the 1960s, due to their relatively high ionic conductivity at ambient temperature. Recently, Lu et al. developed a new β-alumina solid electrolyte (BASE) for potassium-sulfur batteries, based on the BASE already employed in NSBs, that requires high operative temperatures. The new ISE shows good performances at moderate temperatures, increasing the battery safety and decreasing the maintenance costs. The ionic conductivity of the K-BASE at 150 °C reaches the value of 0.01 S cm^{-1} and the battery shows high cycling stability and capacity retention [32]. The main ISEs drawback, due to their fragility and rigidity, consists in an inadequate interface contact with the electrodes, that results in poor battery performances.

3.2.2 Polymer electrolytes (PEs)

The interest in PEs for alkali-ion batteries has strongly grown in the last few years, together with the necessity to find a proper replacement for liquid electrolytes, being the latter responsible for serious safety issues, such as leakages, fires and explosions. The research

activity is mainly devoted to LIBs, due to their widely developed technology and huge demand, but nonetheless the challenge is also addressed towards KIBs.

PEs were discovered in 1973, when Fenton et al. dissolved alkali metal salts in poly(ethylene oxide) (PEO), forming conductive complexes. The material showed a temperature sensitive ionic conductivity, that also increased with the amorphous fraction increase [35]. Then, in 1975, Fusillades et al. created the first GPE, adding organic plasticizers to the polymer-salt matrix, and applied it in LIBs [36]; in the following years Armand et al. designed a PEO-based solid electrolyte. The subsequent progress was reached in 1988, when Skaarup et al. added particles of the fast ionic conductor Li_3N into a PEO-$LiCF_3SO_3$ matrix, obtaining the first CPE [37]. This new electrolyte showed an increased ionic conductivity if compared to standard PEO, but a significant conductivity improvement was achieved in 1989 by Wieczorek et al. They discovered that the addition of Al_2O_3, or other non-ionic fillers, increased the ionic conductivity of PEO-based electrolytes by more than one order of magnitude [38]. PEs chronological development is showed in Figure 3.3. The subsequent and current studies focus on overcoming the main SPEs, GPEs and CPEs limits. The state of the art of PEs for KIBs has not yet reached satisfying results, hence the available LIBs data are presented in the next paragraphs.
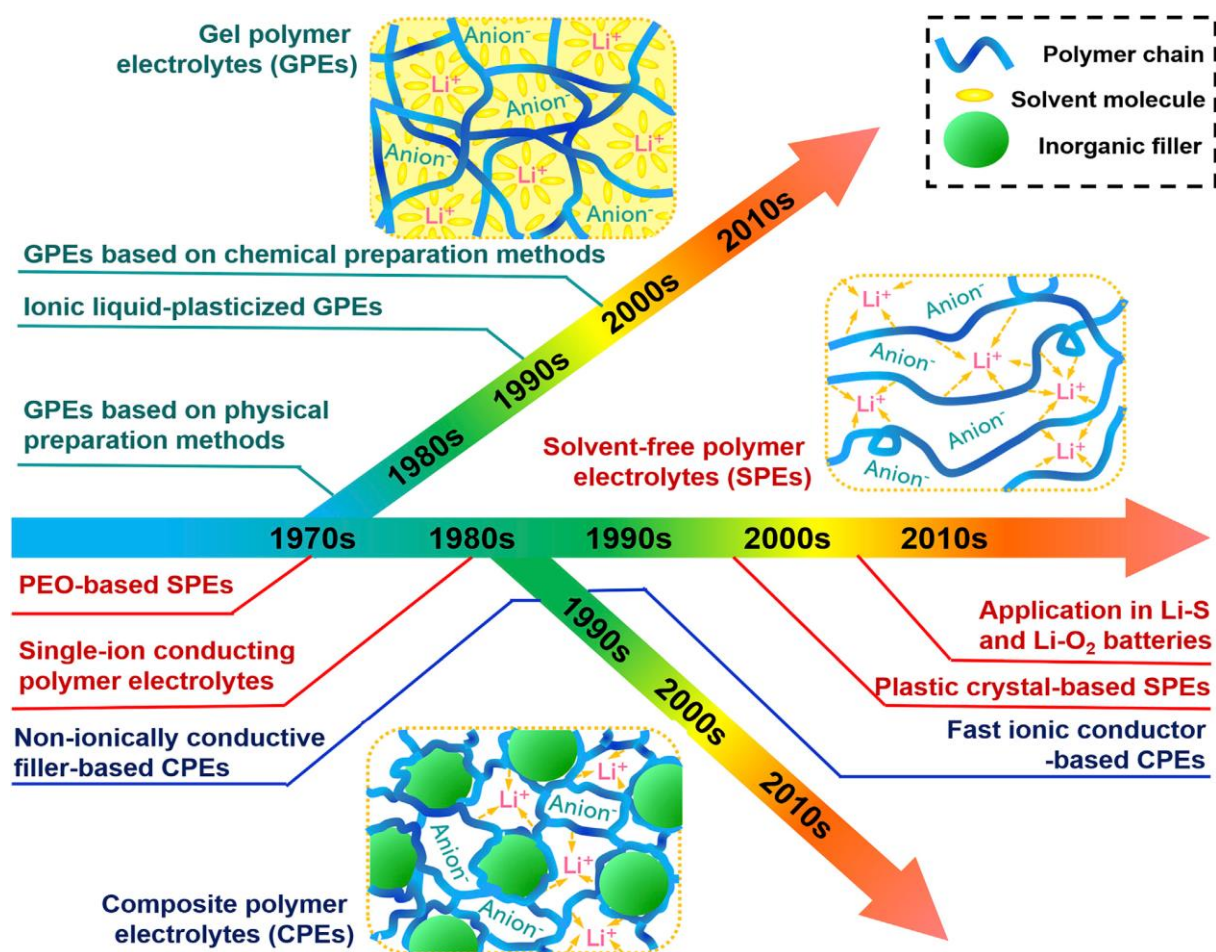
Figure 3.3: PEs chronological development [34].

A polymer electrolyte is usually a membrane, mainly composed of a cross-linked polymer matrix and one or more dissociated salts. PEO is the most frequently used polymeric matrix, but many other polymers have been employed for PEs, such as poly(vinylidene fluoride) (PVDF), poly(methyl methacrylate) (PMMA), poly(acrylonitrile) (PAN), poly(vinyl alcohol) (PVA) and poly(vinyl pyrrolidone) (PVP).

The membrane ionic and electronic conductivities are the most important features, as electrolytes must assure ions transport and hinder electrons one. Alkali ions transport occurs mostly in the polymer matrix amorphous regions, thanks to the large free volume between the polymeric chains and to their high mobility. In this framework, when an electric field is applied, ions transport takes place thanks to ion hopping between coordination sites on the polymer chains [Figure 3.4]. The latter represents the fundamental conduction mechanism in solid state PE. Reducing the matrix crystalline fraction allows to increase the chain segmental motion and thus the ionic conductivity: in SPEs, the growth of crystalline regions can be hindered by some structural modification mechanisms, such as cross-linking and copolymerization; in the obtained polymer matrix, an increase of amorphous phase can be achieved with filler inclusion obtaining CPEs; a further increment can be provided by plasticizers addiction, as for GPEs.

An ideal PE should possess some fundamental characteristics. High **thermal and chemical stabilities** are basic requirements for a safe and durable battery. The **ionic conductivity** should be higher than 10^{-4} S cm^{-1}, to assure good battery performances also at low temperatures; the **electronic conductivity** should be lower than 10^{-6} S cm^{-1}, in order to avoid self-discharge and short-circuits. The ionic conductivity is increased by low **crystallinity** and a low **glass transition temperature** (T_g), that involves higher polymer chains mobility. The **cationic transference number** (t^+) indicates the membrane efficiency in cations conduction and inefficiency in anions conduction, which is not useful for the charge storage mechanism. The t^+ should be close to unity, since it is evaluated as the ratio between the cationic conductivity and total conductivity. A wide **ESW** is fundamental to obtain a large voltage working range for the battery and to stabilize the electrolyte towards the electrodes. The membrane **elastic modulus** should overcome 6 GPa: in this way the electrolyte can withstand the electrodes volume changes occurring during the charge/discharge process and thinner membranes can be employed, decreasing the battery weight while suppressing the dendrite growth. Adequate **interface contact** and **compatibility** with the electrodes are necessary to reduce the cations transport resistance and to stabilize the whole battery. The last important features for a PE are **low toxicity**, **low cost** and **eco-friendliness**: these aspects are fundamental for production, commercialization and recycling, together with the reduction of pollutants emissions [39].

Solid polymer electrolytes (SPEs)

SPEs are generally composed by a polymer matrix and one or more alkali salts; their production methods include solvent casting, hot molding and extrusion. As previously explained, the cationic transport happens in the matrix amorphous regions, through ion hopping between coordination sites and through chain segmental motion [Figure 3.4]. Therefore, the SPEs ionic conductivity strongly depends on the crystallinity degree of the polymer matrix, on its ability to solvate alkali salts and on the presence of suitable coordination sites.
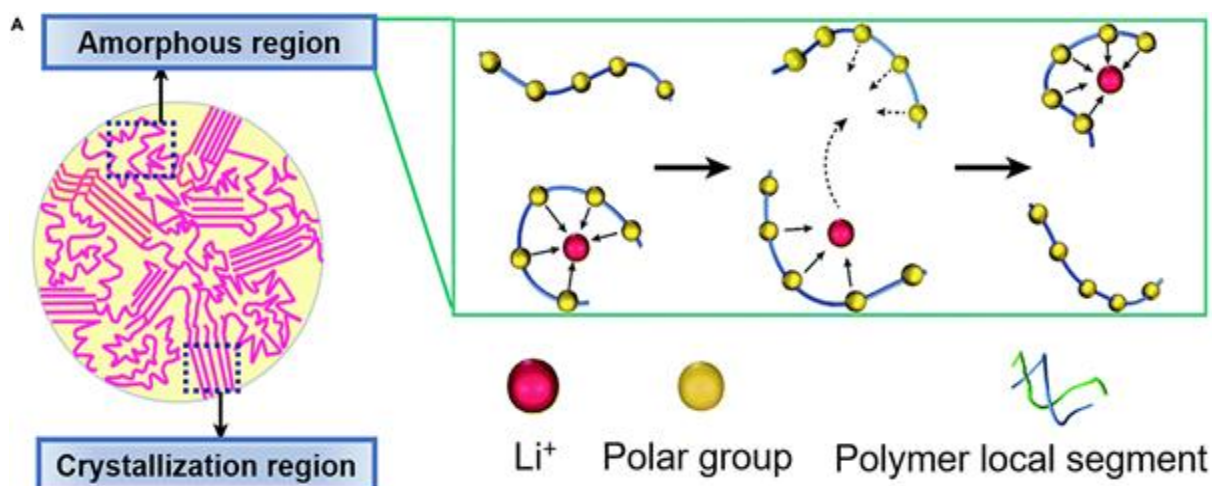
Figure 3.4: Schematic illustration of Li$^+$ ion transport mechanism in SPEs [34].

Many polar polymers have been employed as SPEs in LIBs, such as PEO, PVDF, PMMA and PAN [40]. Among them, PEO is the most studied for SPE polymer matrixes. PEO basic chemical structure (-CH$_2$-CH$_2$-O-) allows to efficiently solvate and host Li salts and, at the same time, Li$^+$ ions transport is favored by the flexible PEO framework. However, this polymer shows a narrow ESW and a crystalline nature at ambient temperature: as a consequence, the ionic conductivity is relatively low (10^{-6}-10^{-8} S cm^{-1}).

Researchers also addressed their efforts on other polymer categories, including polycarbonates, polyesters and polysiloxanes. Polycarbonates show a high dielectric constant, that increases alkali salts dissociation: for this reason, they can be used as side chains in aliphatic polymers, improving the ionic conductivity and the salts solubility. They include poly(ethylene carbonate) (PEC), poly(trimethylene carbonate) (PTMC) and poly(propylene carbonate) (PPC). Polyesters and polysiloxane are characterized by low T$_g$, therefore they are amorphous at room temperature and, thus, provide high ionic conductivities. However, the low T$_g$ significantly decreases the mechanical strength; cross-linking and copolymerization are suitable methods to solve this issue.

Some modifications can be applied to improve the low ionic conductivity that characterizes some SPEs membranes, in order to avoid high working temperatures (>60 °C).

The *polymer-in-salt electrolytes* consist of a small polymer quantity dissolved in a molten salt, the percentage concentration of which is usually more than 50 wt%. This kind of electrolytes was first developed by Angell et al. in 1993 [41] and in 2018 Chen et al. discovered that the ionic conductivity can be considerably increased with a salt percentage concentration between 75 wt% and 95 wt%. Nevertheless, polymer-in-salt systems show worse mechanical properties with the salt concentration increase: this drawback can be partially overcome with polymer framework modifications, such as cross-linking, copolymerization and grafting.

Conventional SPEs are defined bi-ionic conducting systems, as they allow the transport of both cations and anions. The electrodes and the electrolyte only exchange cations, while the anions

conduction is not necessary for the cell and it can cause concentration polarization and thus cell impedance increase. It is possible to hinder the anion conduction with *single-ion conducting polymer electrolytes* (SIPEs): in these SPEs, anions are covalently bonded or immobilized in the polymer framework. SIPEs t^+ number approaches unity, but at the same time these electrolytes show a severe reduction in the ionic conductivity, that can be improved only at high temperatures.

Gel polymer electrolytes (GPEs)

GPEs represent an intermediate class between liquid and solid electrolytes: they are made by the typical SPEs polymer matrix with dissolved salts and with the addition of liquid plasticizers, such as organic solvents or ILs. The presence of liquid plasticizers increases the membrane ionic conductivity, reaching values closer to liquid electrolytes at room temperature, and modifies the ions transport, as the conduction mainly occurs in the liquid phase rather than in the polymer matrix. The presence of a liquid plasticizer can promote the formation of stable SEI layers and increases the GPE flexibility; the latter assures a good electrode/electrolyte interface contact, it hinders the dendrites formation and withstands volume changes during the battery charge/discharge process. At the same time, the polymer matrix assures mechanical support and retains the liquid phase, which increases safety by avoiding leakages. These features get worse as the liquid fraction increases; some feasible solutions include blending, cross-linking and copolymerization.

GPEs can be classified into physical and chemical gels, considering their preparation method.

Physical gels are produced in two steps: firstly, a porous polymer framework is formed through the polymer dissolution in an organic solvent, that is subsequently evaporated. Then, the dry polymer is swollen with a solution of liquid plasticizers and alkaline salts. Some significant physical methods include conventional solution casting, inverted phase and electrospinning. Physical gels polymer chains only interact with weak physical bonds, such as electrostatic and hydrogen ones, without strong cross-linking: as a consequence, liquid leakages and safety issues are the main drawbacks.

Chemical gels are characterized by strong cross-linking, therefore they show higher mechanical and thermal stability, as well as less safety issues if compared to physical gels. The polymer monomers and the cross-linking initiator are dissolved in a liquid phase, that can be immobilized into the membrane matrix. The polymerization process can start with various methods, including thermal, radiation and electrochemical initiations, that define different chemical production processes [34,42].

Many different polymers have been used as GPEs matrixes in LIBs, such as PEO, PVDF, PVDF-hexafluoropropylene (HFP), PMMA and PAN. The commonly employed plasticizers are the organic solvent PC, EC, DMC, DEC, TEGDME and DME, as well as ILs.

PEO is also most studied polymer for GPEs. It can be used in LIBs thanks to its high compatibility with Li, but the plasticization with organic solvents decreases its mechanical properties. This drawback can be overcome by blending and cross-linking PEO with other polymers, such as PVDF and PAN, that strongly increase the mechanical strength. Li et al.

formulated a 1:5 PVDF/PEO cross-linked nanofibrous membrane, that showed a high ionic conductivity of $4.8 \cdot 10^{-3}$ S cm^{-1} at room temperature [43]. A PAN/PEO cross-linked copolymer was developed by Kuo et al. The new blend was named XANE and it showed high ionic conductivity ($\approx 8 \cdot 10^{-3}$ S cm^{-1}) and electrolyte uptake amount (425 wt%) [44].

PMMA, as well as PEO, is characterized by poor mechanical strength, therefore blending and copolymerization, but also nanofillers addition, are employed to obtain better performances. Nanofillers introduction can also improve the membrane electrochemical properties; for instance, Sharma et al. produced a PMMA polymer matrix with the addition of SiO$_2$ nanofibers as 10 wt%, obtaining an ionic conductivity of $2.56 \cdot 10^{-3}$ S cm^{-1} [45].

PAN-based membranes do not suffer from poor mechanical strength, but they show high reactivity towards Li and K. The introduction of nano-sized ceramic fillers, such as BaTiO$_3$, SiO$_2$ and Al$_2$O$_3$, stabilizes the membrane, increasing its compatibility towards alkali metal anodes.

PVDF and PVDF-HFP show mechanical strength and thermal stability, but they are characterized by low compatibility with most liquid electrolytes and thus by poor electrochemical performances. Blending, copolymerization and fillers addition are usually employed to overcome these drawbacks [46].

Environmental compatibility, sustainability and recyclability are fundamental requirements for electrolytes and batteries future developments, therefore bio-based and biodegradable polymers are promising alternatives to the common PEs. Only few studies have been performed, mainly concerning cellulose, as it is one of the most abundant natural polymers and it shows high thermal stability and good compatibility towards several electrolytes. Not only common cellulose has been tested as GPE polymer matrix, but also nanocrystalline cellulose (NCC), cellulose nanofibrils (CNF), bacterial cellulose (BC) and some cellulose derivatives. The ionic conductivity of the cellulose-based membranes can reach values up to 10^{-3} S cm^{-1}, together with satisfying mechanical and thermal stabilities [46]. Cellulose and other bio-based materials, such as lignin, silk, gelatin, agar, carrageenan and chitosan [Figure 3.5], can also be employed as fillers in CPEs, which are described in the following paragraph.
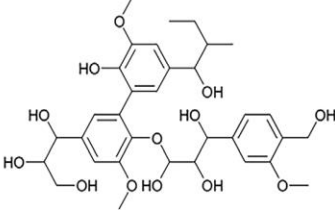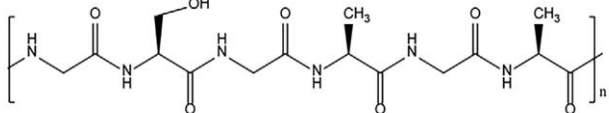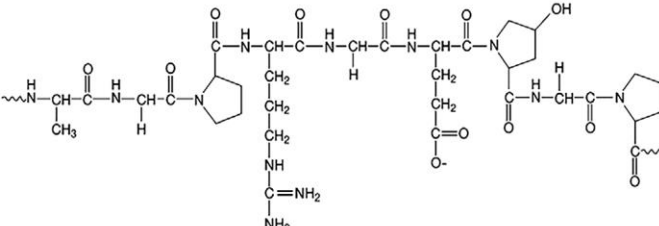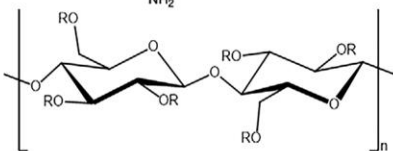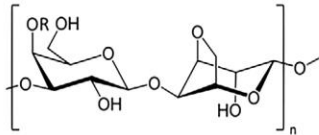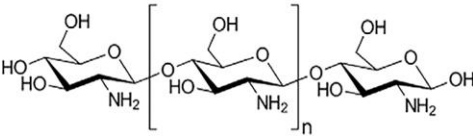
Figure 3.5: Most commonly used biopolymers for battery applications [47].

Composite polymer electrolytes (CPEs)

Besides copolymerization, blending and cross-linking, it is possible to improve GPEs and SPEs performances with inorganic fillers addition, obtaining CPEs. The commonly used fillers can be classified into two groups: the non-ionic conductive or inert fillers are usually ceramic powders, such as aluminum oxide (Al_2O_3), zirconium oxide (ZrO_2), titanium dioxide (TiO_2) and silicon dioxide (SiO_2); the ionic conductive or active fillers include NASICON and garnet oxides.

Inert fillers can be considered as solid plasticizers, as they increase the polymer matrix amorphous fraction and the chains mobility, therefore they improve the ionic conductivity; considering LIBs, Al_2O_3 and SiO_2 show the best results. The filler chemical nature and its surface groups strongly influence the CPE ionic conductivity and mechanical strength, but these properties also depend on the filler size and shape, as well as on its concentration within the

matrix. The conductivity is subject to the highest increase with the smallest filler particles, as they offer the highest surface area. For instance, considering a PEO-based CPE, filler nanoparticles sized from 10 μm to 10–20 nm can increase the ionic conductivity by one order of magnitude. The inert fillers can be classified according to their shape, into 0D particles, 1D wires, 2D sheets and 3D networks. The 0D nanoparticles moderately improve the alkali ions transport through the matrix, and therefore the ionic conductivity; a higher improvement is obtained with 1D nanowires and a further enhancement can be reached with aligned nanowires, that create preferential conduction pathways [Figure 3.6]. Furthermore, a high filler concentration increases the CPE mechanical strength and it improves dendrites suppression, but it also lowers the ionic conductivity [48].
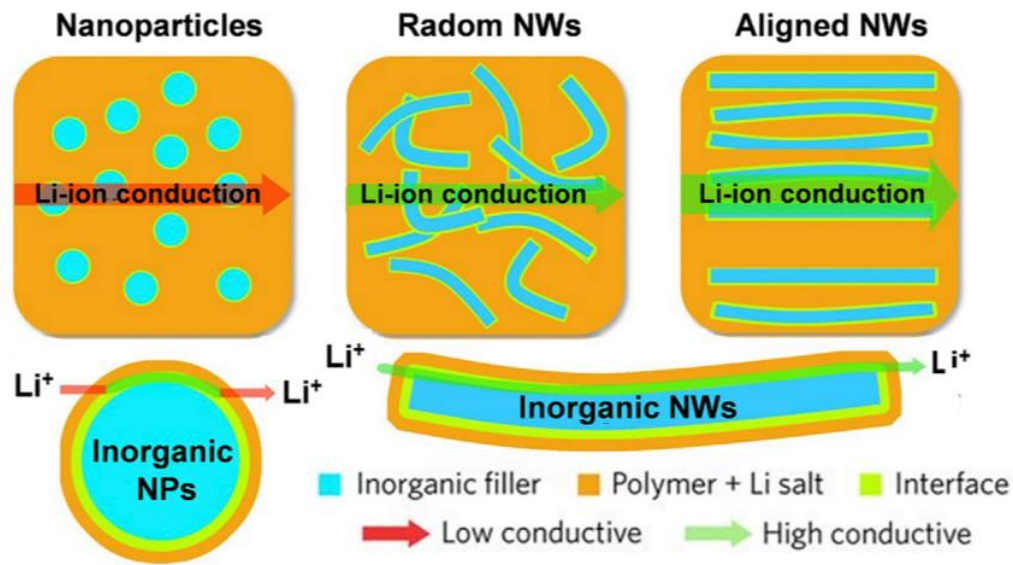
Figure 3.6: Li-ion conducting pathways in CPEs with nanoparticles (NPs), random nanowires (NWs) and aligned nanowires [34].

Active fillers effects on CPEs are not well defined. The number of studies on these materials is constantly increasing, but the results are frequently contradictory. For instance, some works report an ionic conductivity increase in CPEs containing active fillers, while others describe insignificant or negative effects on the electrolyte conductivity. Further research study is required to reach more reliable and systematic results [48].

As previously stated, some bio-based and organic materials are regarded as promising CPE fillers and a few studies have already been realized, with both LIBs and KIBs. The most interesting materials include nanocellulose, carbon nanotubes (CNTs), halloysite nanotubes (HNTs) and lignin.

3.3 Lignin

Plant and wood biomass is the most abundant renewable resource on Earth, and its three main components are cellulose, hemicellulose and lignin. Cellulose is usually the biomass main constituent, while the lignin content can vary between 15% and 40%, based on the lignocellulosic source. Lignin shows two different forms: native lignin only exists in the lignocellulose structure, while technical lignin results from extraction processes. Native lignin is part of the plant cell walls, combined with cellulose and hemicellulose, and it provides rigidity and mechanical support. It shows a complex polymer structure, that contains methoxyl groups, phenolic hydroxyl groups and terminal aldehyde groups. Lignin production in plants occurs through enzyme-mediated dehydrogenative radical polymerization, with the formation and cross-linking of three main monomeric units: p-hydroxyphenyl (H-unit), guaiacyl (G-unit) and syringyl (S-unit), that derive from paracoumaryl alcohol, coniferyl alcohol and sinapyl alcohol respectively [Figure 3.7] [49].
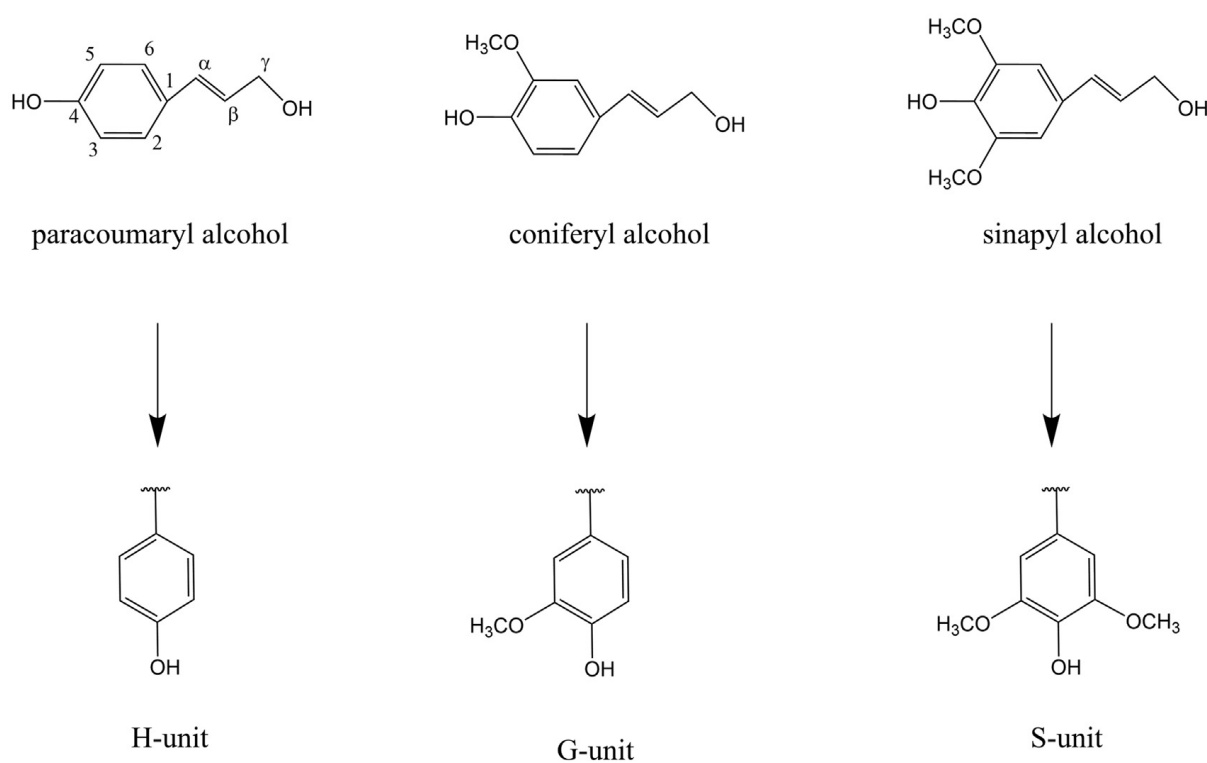
Figure 3.7: Lignin precursors and monomeric units [50].

The three monomeric units can be linked with different chemical bonds, such as aryl ether (α-O-4 and β-O-4), phenylcoumaran (β-5), biphenyl (5-5), diaryl ether (4-O-5) and diarylpropane (β-1) [Figure 3.8]. The monomeric units and functional groups relative amounts, as well as the bonds nature, which define the chemical, physical and morphological properties of the biomass, vary among different plants.
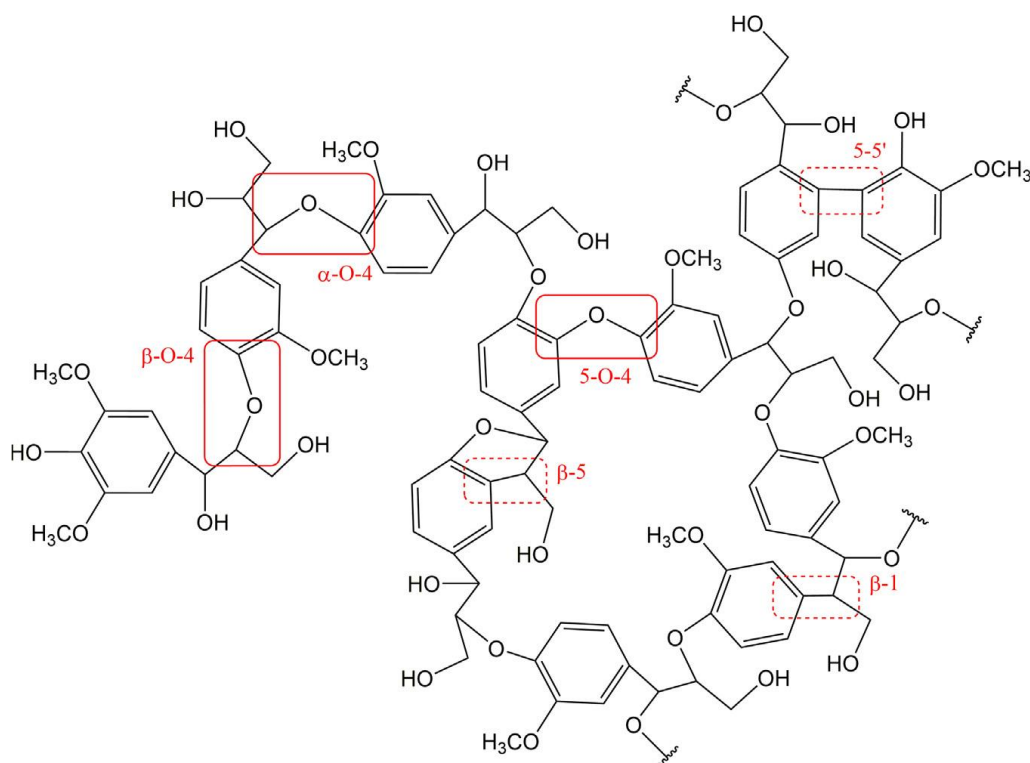
Figure 3.8: Typical lignin molecule linkages [50].

Technical lignin can be obtained as a by-product of paper pulping process; it is usually treated as a waste material, primarily for energy generation through combustion. Recently, it has been highlighted as a promising renewable source of aromatics for the production of high performance, low cost and environmentally friendly polymer materials. Nevertheless, only a restricted fraction of the annually produced lignin is currently exploited for high value applications: further studies are firmly necessary to overcome some drawbacks, such as low reactivity and difficulty in extraction.

The most relevant technical lignins are kraft lignin, lignosulfonates and organosolv lignin. They differ in structure and characteristics, as they derive from different extraction and purification processes.

Kraft lignin is produced by Kraft pulping, which is the most used processes for wood delignification in the paper industry. The biomass is treated with a basic solution of sodium hydroxide (NaOH) and sodium hydrosulphide (NaHS) at high temperature (150-170 °C), causing α-O-4 and β-O-4 bonds cleavage. The obtained small lignin fragments are then recovered through ultrafiltration or precipitation, that occurs thanks to black liquor acidification up to pH 5 or lower. Kraft lignin is still mainly used as energy source, due to its hydrophobic and inert nature.

Lignosulfonates are obtained from the sulfite process, which is similar to the Kraft one, but can be carried out at different pH values: acid bisulfite process with a pH between 1–2, bisulfite process with a pH between 3–5, neutral sulfite process with a pH between 5–7 and alkaline sulfite process with pH between 9–13. The lignin decomposition occurs with the cleavage of α-

O-4 and β-O-4 bonds, at a temperature from 140 to 160 °C. The lignosulfonates recovery is usually performed through ultrafiltration. The obtained technical lignin fragments possess sulfonic groups attached to the aliphatic chain and are highly soluble in water.

Organosolv lignin derives from the organosolv process, in which the lignin extraction is performed by organic solvents, such as ethanol, formic acid, methanol, acetic acid and acetone, at a temperature between 150 and 170 °C. The following recovery is obtained through flash distillation or acid precipitation. The characteristics of the lignin fragments strongly depend on the solvent nature, but the most important organosolv lignin feature is its high purity: unlike kraft lignin and lignosulfonates, it does not contain sulfur and thus it is directly suitable for high-value applications. Its main drawbacks include low molecular weight and high hydrophobicity [49,50,51].

Lignin and its derivatives have been recently highlighted as promising materials for battery applications: they would decrease the battery cost and improve its sustainability and recyclability. All of these lignins exhibit a variety of properties, which may be favorable for different purposes; thus they can be used in electrochemical systems for different components and applications. For instance, lignosulfonate provides sulfur doping agents and can be employed as fillers in CPEs. Hydrolyzed lignin has been used as cathodic material and organosolv lignin as anodic material, while kraft lignin can be employed in cathodes or PEs. Furthermore, all lignins are often used as precursors for carbon materials, such as carbon nanofibers and porous carbon [52].

Recently, lignin has been studied as GPE component. Gong et al. synthesized the first lignin-based GPE: the electrolyte membrane was fabricated with lignin and distilled water only, and it was then soaked in an EC/DEC/DMC organic electrolyte. The obtained GPE showed an ionic conductivity of $3.73 \cdot 10^{-3}$ S cm^{-1}, high electrochemical and thermal stability, as well as a good compatibility with Li metal [53]. Liu et al. developed a biodegradable GPE lignin-based membrane for LIBs: it was produced synthesizing PVP on a lignin matrix, then the membrane was swollen in a liquid electrolyte, as a common GPE. The new lignin-based electrolyte showed remarkable mechanical, electrochemical and thermal stability, and a high ionic conductivity of $2.52 \cdot 10^{-3}$ S cm^{-1}. These results prove that these lignin-based GPEs can be employed as novel electrolytes for high-performance, low-cost and environment-friendly LIBs [54].

3.4 Self-healing (SH)

A SH material has the ability to restore its original structure and properties after a damage, as naturally happens in the biological systems. EESs would highly benefit from the use of electrode materials or solid electrolytes that are able to repair themselves, with the elimination of damages, ruptures and cracks that could lead to battery degradation and failure, but also to short-circuit, leakages and explosions. Furthermore, the use of components with SH properties would increase the battery durability and reliability, and it would simultaneously decrease the wastes and the electrochemical energy cost [55].

The SH materials are mainly classified into extrinsic and intrinsic. The extrinsic ones display their self-repair ability through the release of healing agents, which must be added to the matrix

during the material production. These substances are stored into small capsules, pipes or channels, which break and release their content when the hosting material undergoes damages and localized mechanical stress. The released agents physically fulfill the fractures or they chemically react with the broken interfaces, restoring the original structure. The main drawbacks of these materials are the difficult production processes and the SH agents consumption, which does not allow to repeatedly repair the same area. The intrinsic SH materials are mainly polymers and they are able to form reversible dynamic bonds between their chains. When a damage occurs, these relatively weak interactions are broken, but they can reform and hence repair the fracture. The reversible dynamic interactions can be covalent and non-covalent; the first ones include disulfide bonds, imine bonds, Diels–Alder reactions, olefine bonds and borate ester bonds. The non-covalent bonds include electrostatic interactions, host–guest interactions, crystallization, hydrophobic interactions and hydrogen bonds. The intrinsic SH materials display several favorable properties: they can repeatedly self-heal the same region; they display a simple production process; they do not need external agents to perform self-repair. Nevertheless, some external conditions can promote the SH, such as heating, light and catalysts addition [55,56]. The structures and the repair mechanisms of intrinsic and extrinsic SH materials are showed in Figure 3.9.
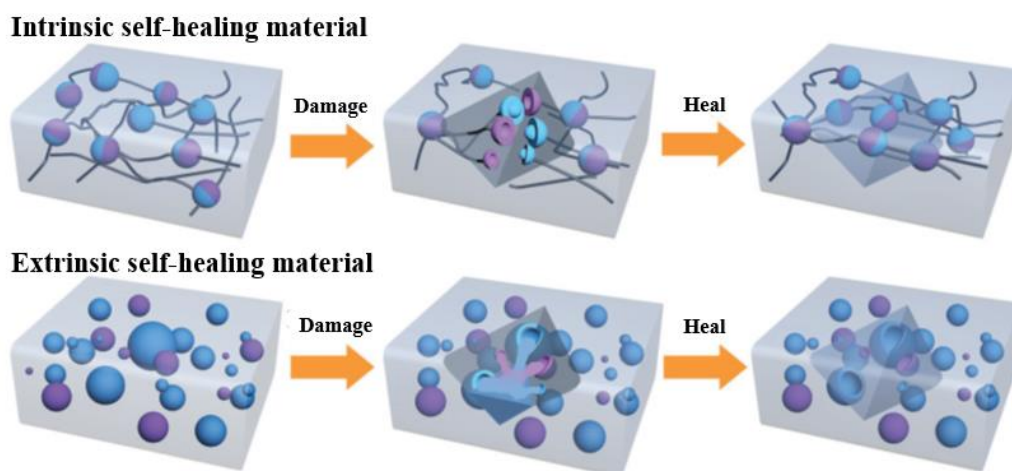
Figure 3.9: SH intrinsic/extrinsic materials structures and mechanisms.

The intrinsic SH materials that form hydrogen bonds are the most promising for EESs and mainly for batteries applications; these materials include supramolecular rubber (SR), ureido pyrimidinone (UPy)-based polymers, carboxylated polyurethane (CPU), polyacrylic acid (PAA) and others. Recently, UPy-based polymers have raised great interest, due to their ability to form quadruple hydrogen bonds. The UPy moieties can be added in a large variety of polymer chains as side groups, providing SH properties. For instance, Xue et al. [57] developed a SH polymer electrolyte through the copolymerization of ureido-pyrimidinone methacrylate (UPy-MA) and poly(ethylene glycol) methyl ether methacrylate (PEGMA). The material showed a high stretchability and the ability to spontaneously reform quadruple hydrogen bonds when two fractured surfaces were reconnected. Furthermore, the electrolyte was tested into LIBs: it

displayed a wide ESW and a moderate ionic conductivity, and it was able to maintain a high specific capacity after an intentionally performed cut. Further studies are necessary to improve the ionic conductivity and to expand UPy-based polymer electrolytes application to KIBs, as they could self-repair the damages caused by the electrodes volume changes and by the formation and growth of dendrites [56,58].

3.5 Solid electrolyte interface (SEI) layer

The SEI layer is a passivation layer resulting from reductive decomposition reactions occurring at the interface between the alkaline anode and the electrolyte components. It is named after its features of a solid electrolyte with high electronic resistivity. However, as each electrolyte, some properties are mandatory for the safe work of the battery:

- high ionic conductivity, in order to avoid ions diffusion resistance;
- adequate thickness, to hinder electrons transfer towards the electrolyte;
- mechanical stability, to withstand potential volume changes during the plating and stripping process;
- structural, thermal and chemical stability, that improve the cycle life and the battery electrochemical properties.

Goodenough et al. discovered that the SEI formation depends on the relative values of the electrode and electrolyte energy levels. Considering the electrolyte, the ESW represents its energy gap enclosed by the voltages of the highest occupied molecular orbital (E_{HOMO}) and the lowest unoccupied molecular orbital (E_{LUMO}). The electrochemical potentials of the cathode and the anode are μ_C and μ_A, respectively. If $\mu_A > E_{LUMO}$, electrons are spontaneously transferred from the anode to the electrolyte, that undergoes reduction and forms the SEI layer on the anodic surface. If $\mu_C < E_{HOMO}$, the electrolyte is oxidized and the products deposit on the cathode surface [Figure 3.10] [59].
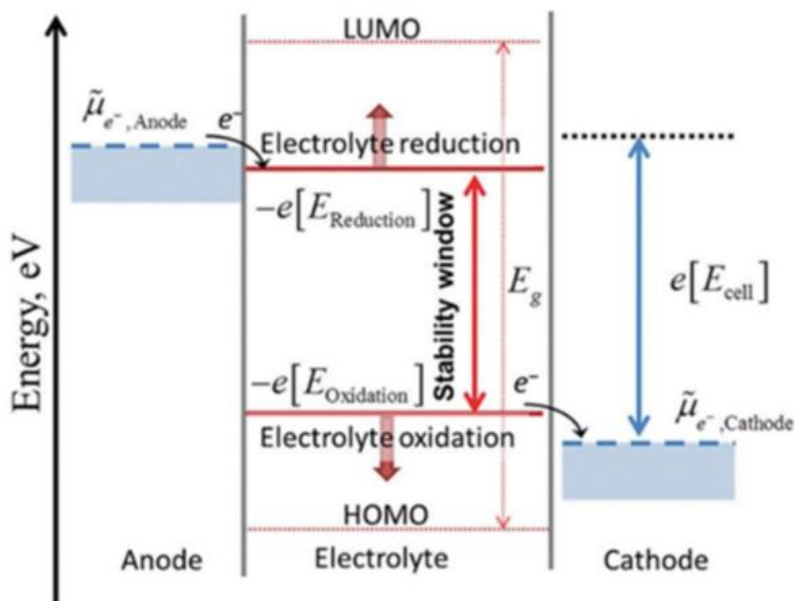
Figure 3.10: Schematic illustration of the energy states of the electrodes and of the electrolyte, leading to the formation of the SEI layers [59].

SEI layers have been extensively analyzed in LIBs, including the formation mechanism, the stability and the ion transfer properties; conversely, considering KIBs and NIBs, only a few studies have been performed, mostly about the SEI composition, morphology and structure. More efforts are needed to understand KIBs and NIBs SEI layer properties and hence their influence on the battery performances. However, the performed studies have shown considerable differences between LIBs, NIBs and KIBs chemistries and SEI layers. Moshkovich et al. demonstrated that the SEI layer stability depends on its surface species solubility into the electrolyte [60]; the latter is further related to the alkali ions Lewis acidity, where the order is $Li^+ > Na^+ > K^+$. A stronger Lewis acid firmly interacts with solvents and negatively charged species and, as a consequence, its salts solubility is higher. Nevertheless, Na^+ ions showed the highest value and, hence, the most instable interfaces, as Li components strong bonds form stable polymerized and cross-linked SEI layers. Additionally, NIBs and KIBs SEI layers display lower ionic conductivities if compared to LIBs ones, as demonstrated by Hess et al. [61]; electrochemical impedance spectroscopy (EIS) measurements revealed an increase in the interface resistance (*i.e.*, 45 Ω - Li, 244 Ω - Na, 2771 Ω - K) and displayed the necessity to improve KIBs SEI layers electrochemical properties.

The KIB SEI layer generally includes both organic and inorganic molecules. The K-organic compounds are described by the general chemical formulas RO-COOK and RO-K, where R is an alkyl group; they derive from the decomposition of the solvent and from the decomposition of potassium salts. The inorganic species show a wide variety, based on the electrodes and electrolyte nature, as well as on the voltage working range; some examples include KF, K_2CO_3, $KHCO_3$, K_2O, K_2S, K_2SO_4, K_2SO_3, KPF_6, KFSI, phosphates and N-containing products [20].

4 Instruments, materials preparation and characterization techniques

The experimental work was performed in the Electrochemistry Group laboratories at DISAT department. This chapter firstly illustrates the instruments and materials used to manufacture the electrodes and the electrolyte, and to assemble them in the coin cell and EL-cell configurations. Subsequently, the performed characterization tests are described.

4.1 Instruments

4.1.1 Ball mill

The ball mill MM400 Retsch allows to grind and homogenize slurries through the application of cyclic oscillations. An Eppendorf tube, in which the primary slurry is contained together with a few zirconia spheres, is placed in one of the two ball mill grinding jars, while the second jar acts as counterweight [Figure 4.1]. The oscillatory movement can be regulated by varying the frequency and the operation time. The ball mill was used to homogenize the Super P slurry.

Figure 4.1: Ball mill MM400 Retsch.

4.1.2 Automatic film applicator

The automatic film applicator is used to cast thin slurry layers, with a thickness of some micrometers, on a metallic collector sheet. The applicator is made up of a glass plate and a moving traverse [Figure 4.2], which causes the advance of the Doctor Blade instrument with a speed rate between 50 and 150 mm s^{-1}. The layer thickness can be regulated varying the Doctor Blade height and the speed rate. The automatic film applicator was employed to lay the Super P slurry on a copper sheet.

Figure 4.2: Automatic film applicator.

4.1.3 Manual disc cutter

The manual cutter was used to cut discs with a diameter of 15 mm. The discs were obtained from a copper sheet, on which the Super P slurry had been deposited, and they were employed as electrodes in different cell configurations. The cutter structure consists of a lever and a piston [Figure 4.3], which moves down through a circular opening and allows to realize highly precise cuts.

Figure 4.3: Manual disc cutter.

4.1.4 Buchi glass oven

The glass oven is employed to remove impurities, solvents and water from samples, through the concomitant application of high temperatures and vacuum. The device is made up of an external glass tube, protected by a metallic case, in which a second glass tube can be inserted. The second tube can be opened and filled with the materials to be treated; it consists of two parts, that are coupled and sealed thanks to a screw and gasket closure. The used model is a

Buchi Glass Oven B-585 [Figure 4.4], that can be manually set and also includes some preset programs. The inner tube upper part owns a screw junction connected to a vacuum pump, which, during the operation, can maintain low pressure, up to 5 mbar, in the device; the lower part is heated up by some resistances. The polymer membranes and the Super P carbon black electrodes were treated in the glass oven before their insertion into the glove box, in order to remove moisture and eventual impurities.

Figure 4.4: Buchi glass oven B-585.

4.1.6 Laboratory oven

The laboratory oven has multiple applications, such as the drying of carbon-coated copper sheets and the moisture removal from instruments that are intended to be brought into the glove box. The model used is a Memmert Universal oven UF55 [Figure 4.5], with a setting temperature range between 20 and 300 °C.

Figure 4.5: Memmert Universal oven UF55.

4.1.5 Laboratory fume hood

The fume hood is used to remove and exhaust hazardous substances, that could be released into the laboratory. For instance, it was employed for potassium metal disposal and to favor the carbon black Super P layer drying [Figure 4.6].

Figure 4.6: Laboratory fume hood.

4.1.7 Glove box

The glove box is a sealed compartment, equipped with two butyl rubber gloves, that allows the operator to work in a controlled atmosphere. The chamber is filled with an inert gas, such as argon, and the oxygen and water levels are kept very low, in this case below 0.5 ppm. Materials and instruments from the external environment are introduced into the glove box through a small or a big ante-chamber; during each insertion, it is necessary to perform a washing process in the ante-chamber, consisting of three repeated cycles of evacuation and argon refill. The glove box was used to produce the liquid electrolyte and to assemble the cells, because of potassium metal high reactivity towards oxygen and water. The used model is a MBraun Labmaster Pro [Figure 4.7].

Figure 4.7: Glove box MBraun Labmaster Pro.

4.1.8 Crimper

The crimper is used to seal coin cells, after their assembly into the glove box. The sealing pressure can be manually regulated by the operator [Figure 4.8].

Figure 4.8: Crimper.

4.1.9 Cycler

The Arbin cyclers [Figure 4.9] are used to perform galvanostatic cycling on the cells, with the application of specific currents or voltages, as determined in the program that the operator must set before each test. The obtained data are processed through the Arbin software MITS Pro and they can be exported into Microsoft Excel. The cyclers possess 8 or 16 channels, where the cells can be simultaneously tested.
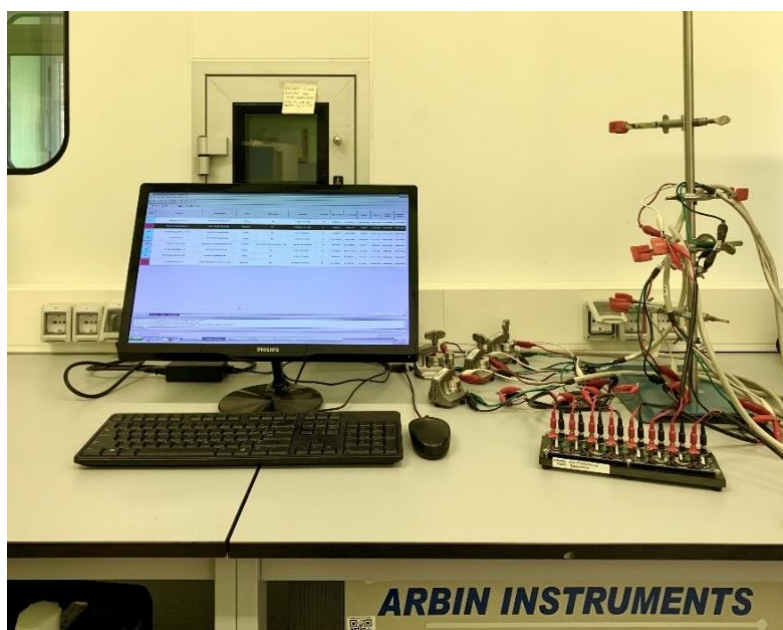
Figure 4.9: Arbin cycler.

4.1.10 Potentiostat

The potentiostat is a multichannel electrochemical workstation, that can apply specific currents or voltages to electrochemically characterize the cells. It is used to perform electrochemical impedance spectroscopy (EIS), linear sweep voltammetry (LSV) and plating and stripping tests; the obtained data are processed by the software EC-lab. The used model is a Biologic VSP3-e potentiostat [Figure 4.10].
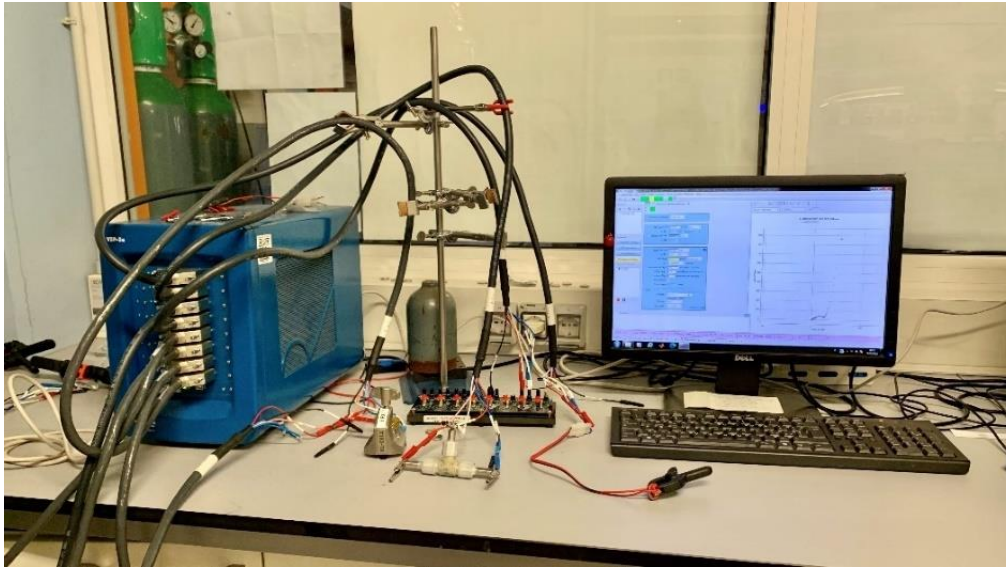
Figure 4.10: Biologic VSP3-e potentiostat.

4.1.11 Climate chamber

The climate chamber can artificially reproduce environmental conditions, with specific humidity and temperature, in order to observe different materials reactions to these conditions. The model used is a Binder MKF 56 [Figure 4.11], that can vary the temperature between -40 and 180 °C, coupled with a Biologic VSP3-e potentiostat. The climate chamber was used to perform ionic conductivity tests on the polymer electrolytes, at different temperatures.

Figure 4.11: Climate chamber.

4.1.12 Digital micrometer

The digital micrometer is employed to measure the polymer electrolyte thickness. The used model is a Mitutoyo Absolute ID-C112XBS [Figure 4.12], with a resolution of 1 μm.

Figure 4.12: Digital micrometer.

4.2 Materials preparation

4.2.1 Super P

The carbon black Super P electrode, casted on a copper collector, was used as cathode in the coin cell and EL-cell configurations. Super P is a HC material; it possesses a porous amorphous framework with a large specific surface and a high structural stability, that hinders high volume variations during the K^+ ions intercalation and de-intercalation process. The resulting disordered carbon lattice provides a superior number of pathways for the ion diffusion, thus increasing the energy density, but also the irreversible capacity. The latter is relevant only during the first charge/discharge cycles of the cell when the high specific surface of the amorphous framework is reacting with the liquid electrolyte and the SEI layer is forming.

Preparation

The Super P slurry was prepared in an Eppendorf tube, with the following composition: 80 wt% of Super P and 20 wt% of PVDF. A balance was used to weight 0.08 g of Super P powder, that was carefully crushed in a mortar, in order to pulverize the agglomerated particles. At the same time, 0.25 g of a solution of 8 wt% of PVDF in N-methyl-2-pyrrolidone (NMP) solvent, that corresponds to 0.02 g of PVDF, were weighted and transferred in the Eppendorf tube, together with the Super P powder and two zirconia spheres. The slurry viscosity was reduced with the addition of 800 μL of pure NMP, then the tube was placed in a ball mill for 15 min at a 30 Hz frequency. The homogenized slurry was layered on a copper sheet, that was previously placed on the automatic film applicator. A Doctor Blade instrument, set at 200 μm, was moved by the applicator traverse, at a speed rate of 50 mm s^{-1}, in order to obtain a homogeneous thickness. The laid slurry was dried for 24 h at a temperature of 50 °C in the laboratory oven, then it was cut with the manual cutter, obtaining discs with a diameter of 15 mm. Lastly, the electrodes were treated in the Buchi glass oven for 4 h at a temperature of 120 °C and then they were stored in the glove box.

4.2.2 Liquid electrolyte

A liquid organic electrolyte was used to swell the membranes, obtaining composite GPEs. It is a solution of KPF_6 0.8 M in 1:1 EC:DEC.

Preparation

The salts and solvents storage and the liquid electrolyte preparation are performed in the glove box. The 1:1 EC:DEC solution was prepared by mixing 50 mL of EC and 50 mL of DEC. The EC is solid at ambient temperature; for this reason, it was previously heated up to a temperature of 80 °C in order to completely melt it. A 1.4725 g mass of KPF_6 was weighted and transferred into a 10 mL flask, then the EC:DEC solution was added, reaching a total volume of 10 mL. After the insertion of a magnetic bar into the flask, the latter was placed on a magnetic stirrer

for about 24 h and then the solution was filtered with folded filter paper, to eliminate the undissolved salt.

4.2.3 Polymer electrolyte

The polymer membranes were supplied by Politecnico di Milano. The dry membranes are defined as composite polymer membranes (CPMs), in which Bretax nanolignin is present as organic filler; before the insertion into the electrochemical cells, the CPMs are swollen with the organic liquid electrolyte described in paragraph 4.2.2, becoming gel-composite polymer electrolytes (GCPEs).

The polymer matrix consists of a cross-linked and interpenetrated membrane with a fixed composition of polycaprolactone di-methacrylate (PCLDMA), polyethylene glycol (PEG or PEO) and ureido-pyrimidinone methacrylate (UPy-MA), while the nanolignin mass ratio with respect to the PCLDMA is varied, *i.e.* 0, 3, 5, 7, 10, 20% $m_{nanolignin}/m_{PCLDMA}$. Table 4.1 displays the different CPMs and it clarifies their composition.

Table 4.1: Acronyms and compositions of the synthesized CPMs.

Acronym	PEG 2000 (wt% vs. m_{PCLDMA})	UPy-MA (wt% vs. m_{PCLDMA})	Bretax nanolignin (wt% vs. m_{PCLDMA})
CPM0	10%	4%	0%
CPM3	10%	4%	3%
CPM5	10%	4%	5%
CPM7	10%	4%	7%
CPM10	10%	4%	10%
CPM20	10%	4%	20%

PCLDMA derives from the methacrylation of polycaprolactone diol (PCL), performed by 2-isocyanatoethyl methacrylate (IEM) and catalyzed by stannous octoate (Sn(oct)$_2$) [Figure 4.13]. PCLDMA was used as cross-linker agent, together with UPy-MA, to obtain the host matrix of the CPM by ultraviolet (UV)-curing.
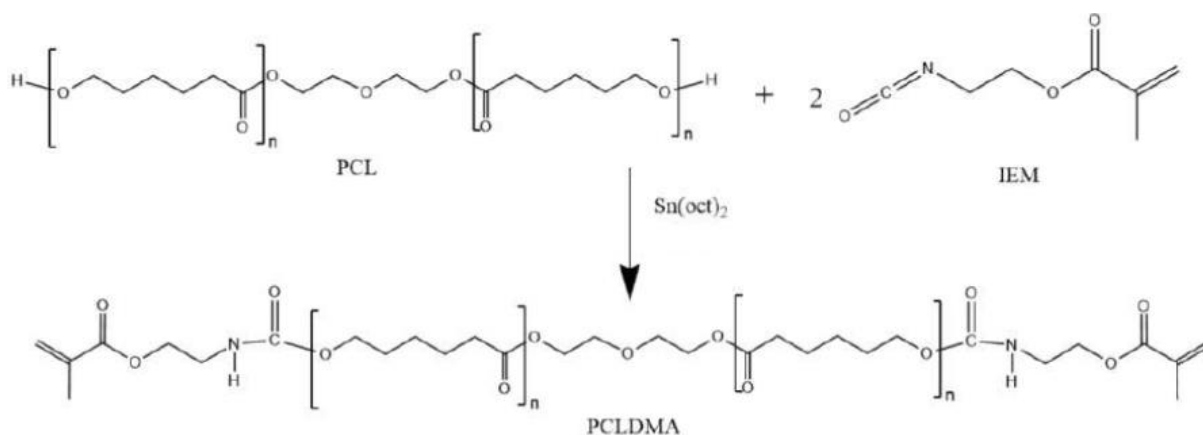
Figure 4.13: PCLDMA synthesis reaction.

PEG with $M_n = 2000$ g mol^{-1} was used as plasticizer and interpenetrated polymer in the CPMs, in order to improve macromolecular mobility, membrane handling, formability and ionic conductivity. PEG chemical structure is shown in Figure 4.14.
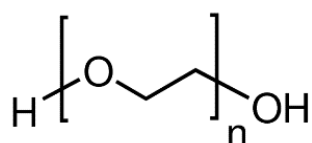
Figure 4.14: PEG chemical structure.

UPy-MA derives from the methacrylation of 6-Methyl isocytosine (MIS), performed by IEM, with dimethyl sulfoxide (DMSO) as solvent [Figure 4.15]. UPy-MA was incorporated in the CPM matrix through UV cross-linking; the UPy addition is due to its ability to form H-bond supramolecular interactions and thus to provide SH properties to the membrane.
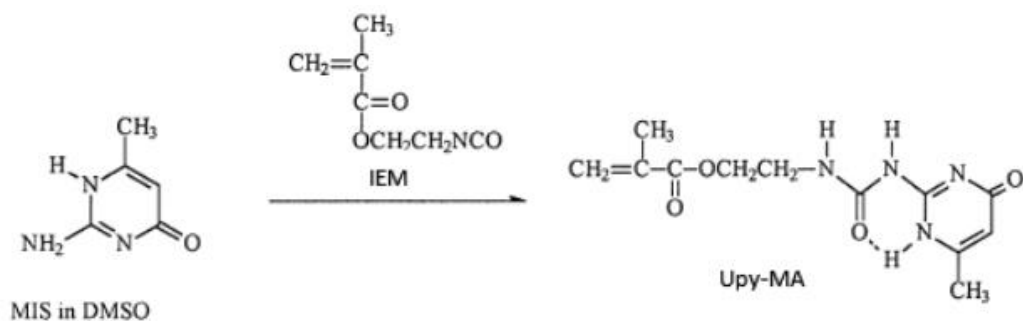
Figure 4.15: UPy-MA synthesis reaction.

Bretax lignin is a lignosulfonate, obtained from lignocellulose through the sulfite extraction process, that has been described in paragraph 3.3. Bretax is a commercial name: this specific lignosulfonate variety is used for chemical applications and it is produced by Burgo Group. Bretax lignosulfonates have a complex poly-electrolytic structure, with anionic functional groups (sulphonic, phenolic), and they show extensive branching of the basic molecular units.

A colloidal dispersion of 200 g L^{-1} of nanolignin in $CHCl_3$ was produced using an ultrasonication probe, starting from a suspension constituted by 4 g of Bretax lignin in 20 mL of $CHCl_3$, previously prepared inside a 25 mL cone-shaped flask. The latter was immersed in an ice bath to avoid excessive heating of the dispersion, due to the exothermicity of the ultrasonication process, which may lead to unwanted evaporation of the solvent. The ultrasonication was carried out for consecutive 6 h, replacing the ice bath with a new one every hour, to maintain low T. The employed device was a Sonics Materials Vibra-Cell VCX130 sonicator tip, working at a frequency of 20 kHz, 130 W power and 95% oscillation amplitude.

Membrane preparation

A known mass amount of UPy-MA (4% m_{UPy-MA}/m_{PCLDMA}) and PEG 2000 (10% m_{PEG}/m_{PCLDMA}) was put in a vial, together with the nanolignin colloidal solution (200 g L^{-1}), the volume of which was determined based on the CPM type. $CHCl_3$ (d=1.49 g mL^{-1}) was added, in order to reach a composition of 120% m_{CHCl3}/m_{PCLDMA}, then the vial was put under magnetic stirring and heated up to 40 °C, to obtain complete solubilization. Subsequently, after the addition and dissolution of a known mass of PCLDMA, the vial was cooled down at room temperature and two pipette drops of ethyl phenyl(2,4,6-trimethylbenzoyl)phosphinate (TPO-L) photo-initiator were added in the solution. The vial was shielded from light with an aluminum foil, to avoid undesired polymerization before the deposition, then stirred to distribute the initiator. The bar coating technique was used to lay membranes with a thickness of 200 μm. After the deposition on a glass surface, the membrane was transferred under the UV-lamp and subject to a 10 min ultraviolet irradiation, which is essential for solid consolidation through cross-linking. The transport of the membrane to the UV-lamp must be as fast as possible, to avoid excessive solvent evaporation, sunlight exposure and foreign particles contact, as they cause cratering phenomena. After 10 min of UV exposure, the cross-linked membrane was air dried for other 10 min, to allow the complete evaporation of the residual $CHCl_3$, that would make the film sticky and difficult to detach. Once dried, the membrane was completely and carefully peeled off the glass surface.

The irradiation process is called UV-curing, as UV radiations provide enough energy to overcome the radical decomposition energy barrier (Gibbs free energy) of the initiator, which allows the cross-linking. The samples were cured in a Helios Quartz UV polymerization equipment (POLIMER 400 W, 230 V - Cod 85L00002), which was set 24 cm away from the sample and it was equipped with high pressure mercury lamps with varied emission windows. The used UV-A lamp has an emission spectrum of 400-315 nm and a radiative power of 36 mW cm^{-2}, when measured with a glass filter.

4.2.4 Coin cell assembly

The coin cell configuration was used in this thesis work to perform galvanostatic cycling tests and interfacial stability tests on the GCPEs. The employed coin cells complied with CR 2032 standard, as they own a 20 mm diameter and a 3.2 mm thickness. The coin cell components and configuration are showed in Figure 4.17.
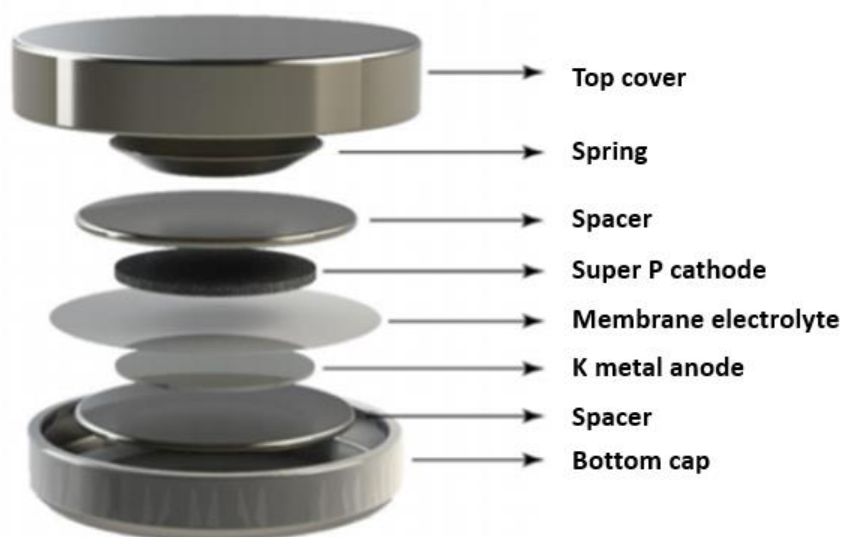
Figure 4.16: Coin cell schematic configuration [62].

The external parts are the top cover and the bottom cap; two stainless steel spacers are placed above the cathode and below the anode, together with a stainless steel spring. In the central part, the cathode, the electrolyte and the anode complete the cell. The coin cells were assembled in the glove box and they generally include:

- a potassium metal anode disc, with a diameter of 16 mm;
- a GCPE disc, with a diameter of 18 mm;
- a Super P carbon cathode casted on a copper collector disc, with a diameter of 15 mm.

The potassium anode was obtained from the pure metal, stored in the glove box: the potassium must be pressed and then cut with a 16 mm punching tool. The Super P cathode was previously produced as described in paragraph 4.2.1 and stored in the glove box; each Super P sample is necessarily weighted to measure its active mass. The membrane disc was cut with a 16 mm punching tool and then it was swollen in the liquid electrolyte described in paragraph 4.2.2. The swelling process increases the membrane diameter, hence it could be necessary to re-cut it with an 18 mm punching tool. The assembled cells were extracted from the glove box and sealed in the crimper with a 6 bar pressure.

4.2.5 EL-cell assembly

The EL-cell configuration was used to perform linear sweep voltammetry (LSV), potentiostatic electrochemical impedance spectroscopy (PEIS), ionic conductivity measurements and plating and stripping tests. EL-cell is a commercial name and the used model was ECC-Std. This configuration maintains the coin cell typical structure, with the potassium metal anode, the GCPE and the Super P cathode; nevertheless, the EL-cell is more suitable for the electrolyte characterization, due to its constant internal pressure, that provides a uniform and better contact between the electrolyte and the electrodes. The EL-cell components and configuration are shown in Figure 4.17.
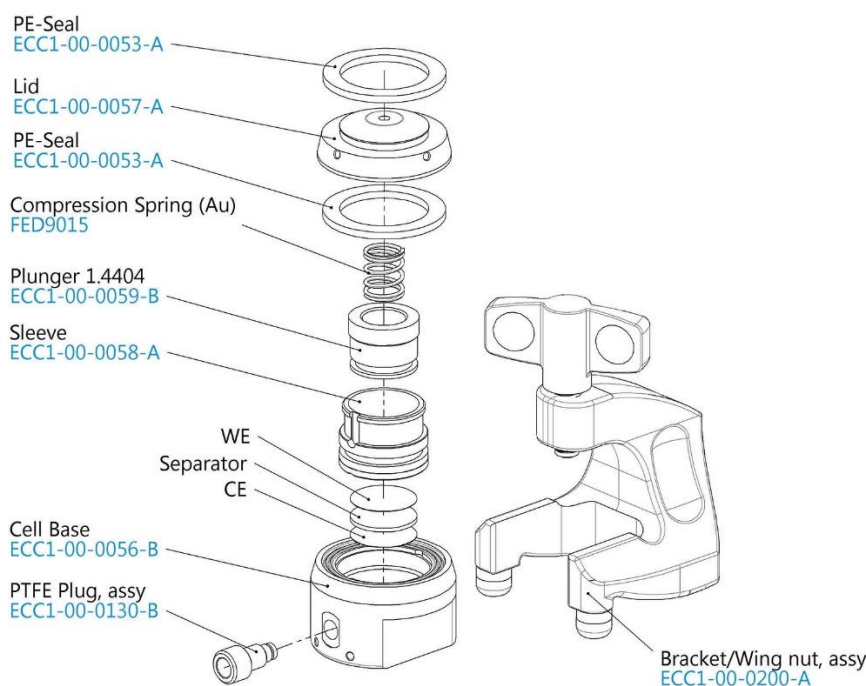
Figure 4.17: EL-cell schematic configuration [63].

The structure, from bottom to top, is made up of a stainless steel base with a poly(tetrafluoroethylene) (PTFE) plug, a poly(ether ether ketone) (PEEK) sleeve, a stainless steel plunger with an 18 mm diameter, a gold plated spring, a polyethylene gasket, a stainless steel cover and an external bracket. The anode, the electrolyte and the cathode are placed between the base and the plunger. The EL-cells were assembled in glove box and closed with the bracket through its wing screw; the spring assures a uniform and constant pressure inside the cell. The base and the top cover own four small holes, that allow the cell connection to the test equipment. The EL-cell is a reusable device and it can be easily opened after the end of the test.

4.3 Morphological and electrochemical characterization techniques

4.3.1 Differential scanning calorimetry (DSC)

DSC is a thermal analysis technique, in which the examined material and a reference one are subject to a controlled temperature variation and the heat flow rate difference between the two samples is measured. In this way it is possible to evaluate the material heat capacity (C_p) variation based on the temperature one. The difference of heat absorbed by the two samples is correlated with the phase transitions of the examined material and they are shown as endothermic or exothermic peaks on a DSC thermogram, where the heat flux (or C_p) is plotted versus the temperature. This analysis allows to identify different materials and their purity by determining their thermal properties, such as the phase transition temperatures and heats. The most relevant temperatures that can be evaluated are the T_g, the crystalline phase formation temperature (T_c), the crystalline phase melting temperature (T_m) and the degradation temperature (T_d).

DSC analysis was performed in Politecnico di Milano to examine the synthesized CPMs, using a DSC823e Mettler Toledo device. Three thermal runs between -100 and 120 °C in an inert N_2 atmosphere, with a heating rate of 20 °C min^{-1}, were performed to assess the T_g (as inflection point of the thermal flux) and the enthalpic heat associated with the crystallinity.

4.3.2 Electrolyte uptake ratio (EUR)

The EUR represents the liquid electrolyte amount that the CPM can absorb and retain during the swelling process. The absorbed liquid quantity depends on the membrane matrix porosity and on the cross-linking degree, hence on the accessible void fraction; it determines the GCPE ionic conductivity, as the ions transport principally takes place in the liquid electrolyte.

This test is performed by swelling the different CPMs in the liquid electrolyte and by measuring the sample mass at 5 min time intervals. The EUR is calculated with the following equation, with the masses expressed in grams:

$$EUR = \frac{m(t) - m_0}{m_0} * 100 \quad (4.1)$$

where m_0 represents the initial dry membrane mass and m(t) is the swollen mass at time t.

4.3.3 Linear sweep voltammetry (LSV)

LSV is an electrochemical analysis method, that allows to evaluate the tested material ESW. The LSV technique involves a three electrodes configuration: a reference electrode (RE), the potential of which is maintained constant, a working electrode (WE) and a counter electrode (CE). During the test, the WE potential is swept at a constant rate [V s^{-1}] in the range of interest, thanks to a potentiostat, and the resulting current is measured at the CE. Redox reactions occur between the WE and the CE, while the RE only acts as a reference for the WE potential

variation. The latter is performed with a positive scanning rate, from the lower up to the maximum potential value of the evaluated range. The obtained data are plotted in a graph, which presents the applied potential as abscissa and the recorded current as ordinate. From the curve analysis, it is possible to acquire information about the electrolyte stability: the presence of a parasitic current at a specific voltage indicates the occurrence of redox reactions and, hence, the possible cell instability.

The LSV analysis was performed by a Biologic VSP3-e potentiostat, in order to evaluate the GCPEs ESW, in the voltage range between 0 and 5 V, with a 0.1 mV s^{-1} scanning rate. The employed configuration was the EL-cell, in which the GCPE was placed between a potassium metal electrode and the stainless steel plunger.

4.3.4 Electrochemical impedance spectroscopy (EIS)

EIS is a simple and fast electrochemical analysis technique, that allows to evaluate the surface properties of different materials. It is mainly used in the characterization of coatings, batteries and fuel cells, but it is also employed to study the mechanisms of electrodeposition, passivation and corrosion. The EIS can be performed under galvanostatic (GEIS) or potentiostatic (PEIS) control; in this thesis work, the potentiostatic mode was chosen. During a PEIS, an AC sinusoidal voltage (E(t)) is applied and it oscillates around the open circuit voltage (OCV) value of the cell; its amplitude (E_0) must be constant and it generally does not exceed 10 mV, while the frequency (f) is usually varied in the range 10 mHz - 100 kHz. Assuming pseudo-linearity, the sinusoidal input leads to a sinusoidal output, which is the measured AC current (I(t)): it differs from the applied AC voltage as it is shifted in phase (φ) and it has a different amplitude (I_0). The AC voltage and the AC current are described by the following equations:

$$E(t) = E_0 \sin(\omega t) \quad (4.2)$$

$$I(t) = I_0 \sin(\omega t + \varphi) \quad (4.3)$$

$$\omega = 2\pi f \quad (4.4)$$

The cell resistance is represented by the impedance Z:

$$Z = \frac{E(t)}{I(t)} = \frac{E_0 \sin(\omega t)}{I_0 \sin(\omega t + \varphi)} = Z_0 \frac{\sin(\omega t)}{\sin(\omega t + \varphi)} \quad (4.5)$$

Considering Euler's relation, the impedance can also be expressed as a complex number:

$$Z(\omega) = \frac{E(t)}{I(t)} = Z_0 e^{j\varphi} = Z_0(\cos\varphi + j\sin\varphi) \quad (4.6)$$

Z(ω) is composed of a real and an imaginary part: the real part can be plotted on the x-axis of the complex Cartesian plane, the imaginary part on the y-axis, obtaining the so-called Nyquist plot. In this plot, each point represents the impedance at a different frequency; the frequency values decrease along the x-axis. A representative Nyquist plot is given in Figure 4.18.
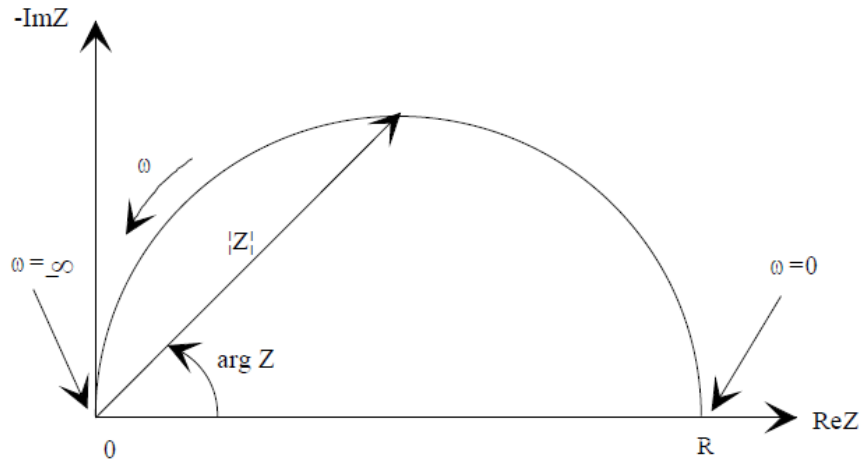
Figure 4.18: Example of Nyquist plot [64].

On the Nyquist plot, the impedance can be represented as a vector of length |Z|; the angle between this vector and the x-axis is φ (argZ), which is usually called phase angle.

In order to interpret the PEIS data, and hence to obtain the Nyquist plot, they have to be modelled by an equivalent circuit, which must fit them properly. Several equivalent circuits are available, with different complexity degrees, but the simplest suitable circuit is made up of a resistor in series with the parallel between a capacitor and another resistor, as shown in Figure 4.19.
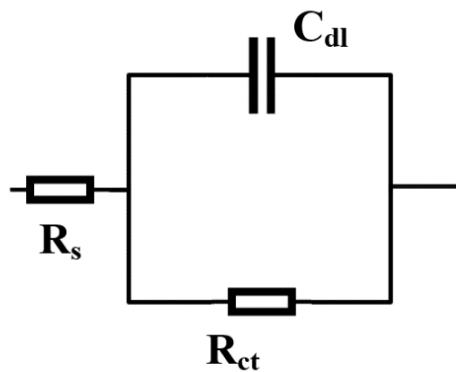
Figure 4.19: Simplest equivalent circuit.

The resistor impedance is defined as $Z = R$, while the capacitor resistance is $Z = \frac{1}{j\omega C}$.

In the equivalent circuit, R_s represents the electrolyte resistance; C_{dl} is the double-layer capacitance, due to the double-layer formation on the electrode surface in contact with the electrolyte; R_{ct} is the charge transfer resistance, which is referred to interfaces, such as the SEI layer. The presence of diffusive phenomena into the cell corresponds to a straight line, with a usual 45° slope, located at low frequencies. In the equivalent circuit, the diffusion resistance

(W) is represented by the Warburg element. R_s, R_{ct} and the diffusion line are shown in Figure 4.20.

Figure 4.20: Example of EIS Nyquist plot.

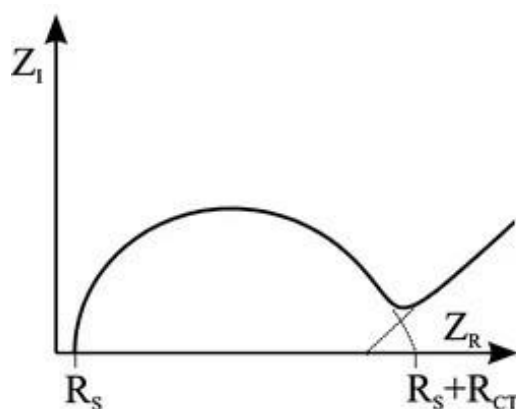## 4.3.5 Ionic conductivity

Ionic conductivity represents the material ability in ions transport. The electrolyte conductivity can be evaluated through a PEIS analysis: in this thesis work, the employed cell configuration was the EL-cell, that was assembled in glove box and in which the GCPE was placed between two stainless steel components. The PEIS was performed by the Biologic VSP3-e potentiostat, with a frequency range between 100 kHz and 1 Hz. The connected EL-cell was placed in a climate chamber, in order to evaluate the conductivity dependence on the temperature; hence, six different PEIS tests were performed, at constant temperatures (10, 20, 30, 40, 50, 60 °C).

The resulting Nyquist plots consist of only the Warburg line: in this configuration, the active material electrodes are not present, hence only ions diffusion happens. The line intersection point with the x-axis represents R_w [Ω], which is the electrolyte diffusion resistance; it is used to evaluate the conductivity value with the following equation:

$$\sigma = \frac{s}{AR_w} \quad (4.7)$$

where σ is the ionic conductivity [S cm^{-1}], s is the GCPE thickness [cm] and A is the contact area [cm^2] between the electrode and the electrolyte.

4.3.6 Interfacial stability

The interfacial stability analysis is performed through repeated PEIS tests and it allows to evaluate the electrolyte compatibility towards the electrodes. In this work, a symmetric coin cell configuration was employed, with the GCPE placed between two potassium metal discs. The cell was assembled in glove box and it was tested with the Biologic VSP3-e potentiostat, by performing a PEIS analysis with a frequency variation between 100 kHz and 10 mHz. The coin cell was then stored with a protective film layer and the test was repeated every 3/8 days.

Considering the obtained Nyquist plots, R_s and R_{ct} may vary between the different measurements. An increase in R_s represents the electrolyte degradation, which is preferable not to occur at the cell working conditions, hence the R_s value should be constant in time. The increment of R_{ct} depends on the SEI layer characteristics and dynamics: an initial increase is inevitable, as it is linked with the SEI formation; a further increment would be caused by the layer instability, therefore a protective and stable SEI results in a constant R_{ct} value.

4.3.7 Plating and stripping test

The plating and stripping test is performed to evaluate the electrolyte and the formed SEI layer ability to guarantee an even cations motion through the electrolyte. The latter results in uniform potassium deposition, which leads to a stable SEI, able to withstand and suppress the dendrites growth. The experiment consists in the galvanostatic polarization of a symmetric cell: a constant current density is applied for 1 h, then it is reversed and applied for another hour; the resulting polarization voltage is constantly measured. The cycle is repeated for a predetermined number of times and at the end of the analysis a PEIS measurement is performed, in order to assess the cell conditions. A high increase in the overpotential represents a non-uniform interface, with possible dendrites nucleation and growth, while a sudden voltage drop could indicate a short-circuit, that usually derives from the membrane perforation caused by dendrites.

In this thesis work, the plating and stripping test was operated by the Biologic VSP3-e potentiostat, that applied to the cell a 0.1 mA cm^{-2} current density for 70 cycles. The employed configuration was the symmetric EL-cell, that was assembled in glove box and in which the GCPE was placed among two potassium metal discs.

4.3.8 Galvanostatic cycling

The galvanostatic cycling is a charge/discharge test performed by a cycler: it can apply currents to the cell, increasing or decreasing the cell potential. The positive current defines the cell charge process, during which the K$^+$ ions move from the positive Super P carbon electrode to the negative potassium metal electrode. The discharge process is the opposite one, caused by the negative current. The resulting potential is constantly detected and its variation is allowed in a specific range; when the voltage range limits are reached, the cycler inverts the current. The charge (CC) and discharge (DC) capacities are also measured, as they are representative of the cell electrochemical performances. Over the cycles, the capacities inevitably decrease because of the cell degradation, that affects both the electrodes and the electrolyte.

In this thesis work, the galvanostatic cycling was performed by the Arbin cycler and the data were elaborated by the MITS Pro software. The employed cell configuration was the coin cell, assembled in glove box. The cycling was usually performed with a 0.05 Ah g^{-1} specific current for the first ten cycles, while for the following ones the current value was increased to 0.1 Ah g^{-1}. Different values can also be employed, considering that the increase in the specific current determines a faster charge/discharge process, but also a faster cell degradation. The voltage range was set between 0.01 and 3 V.

The applied specific current is referred to the effective active mass (m_a) of the Super P carbon cathode, which can be evaluated with the following equation:

$$m_a = 0{,}8 * (m_e - m_{Cu}) \quad (4.8)$$

where m_e is total electrode mass and m_{Cu} is the copper collector mass. The active mass of the electrode is equal to 80% (percentage of Super P carbon in the mixture with the PVDF) of the total mass of the electrode minus the mass of the copper collector.

The charge and discharge capacities are usually referred to the active mass with the following equations:

$$CC_{spec} = 1000 * \frac{CC}{m_a} \quad (4.9)$$

$$DC_{spec} = 1000 * \frac{DC}{m_a} \quad (4.10)$$

where CC_{spec} is the specific charge capacity and DC_{spec} is the specific discharge capacity.

5 Morphological and electrochemical characterization results

5.1 Differential scanning calorimetry

The DSC analysis was performed to evaluate the CPMs thermal properties, such as the T_g and the enthalpy of crystallization. Three thermal runs between -100 and 120 °C, with a heating rate of 20 °C min^{-1}, were performed for each CPM. The first two were required to remove residual solvent and internal stresses; the third run is analyzed and shown in Figure 5.1.
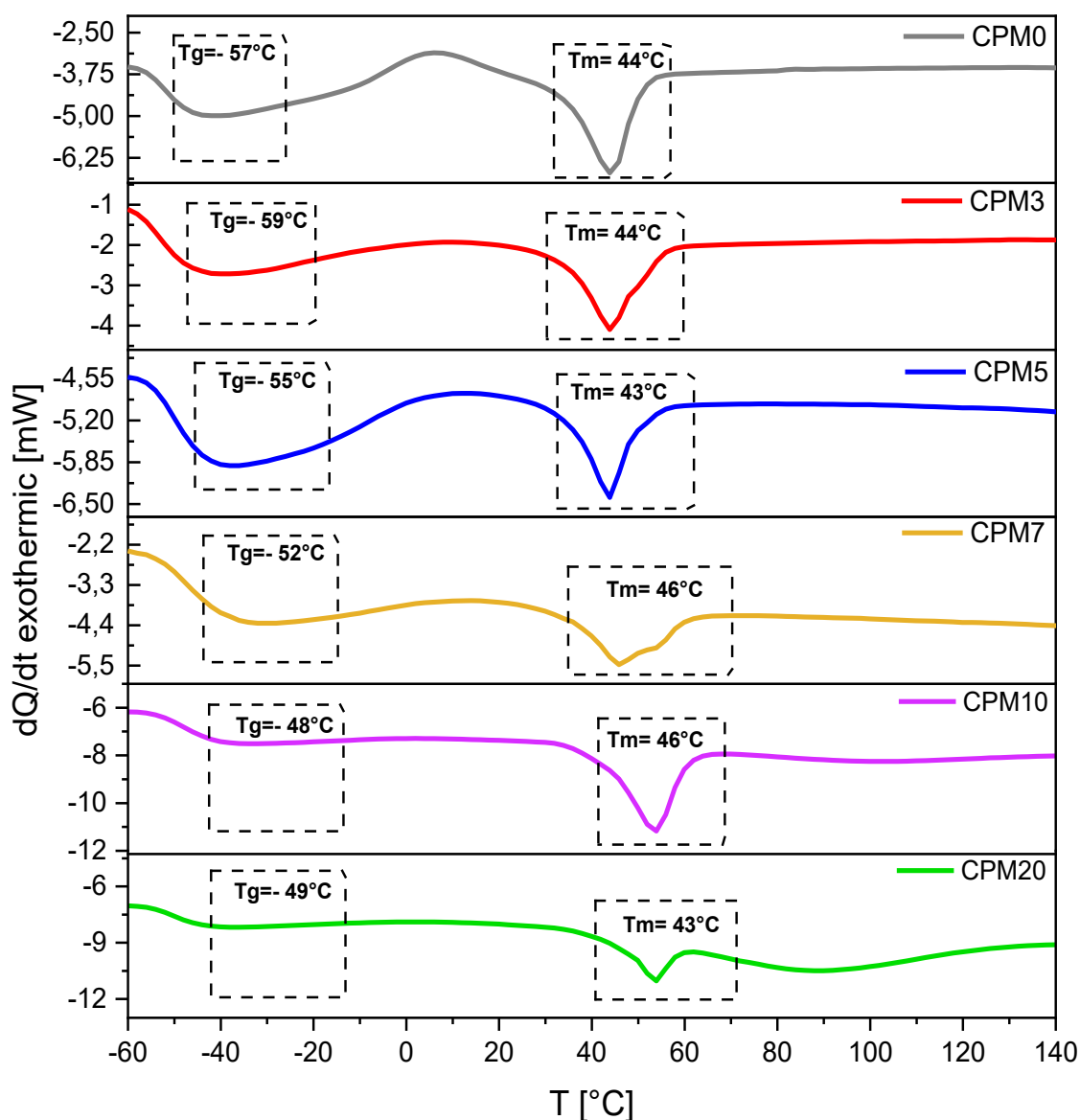

Figure 5.1: DSC plots of the six CPMs (third thermal run).

As displayed in the image, the lignin concentration increment causes a slight increase in the T_g, since high amounts of filler nanoparticles can reduce and partially hinder the polymer chains mobility. Nevertheless, a reduction in the crystallization enthalpy is displayed: this trend suggests that the presence of nanolignin increases the matrix amorphous fraction, as the filler perturbs the crystalline arrangement, typical of some polymer chains. The values of T_g and of the specific enthalpy of crystallization ($\Delta H/m_{sample}$) for the analyzed CPMs are shown in Table 5.1.

Table 5.1: T_g and $\Delta H/m_{sample}$ values for the six CPMs.

Acronym	T_g [°C]	$\Delta H/m_{sample}$ [J/g]
CPM0	-57	-18
CPM3	-59	-10
CPM5	-55	-6
CPM7	-52	-7
CPM10	-48	-7
CPM20	-49	-3

5.2 Electrolyte uptake ratio

The EUR was evaluated for the CPMs employing the organic liquid electrolyte KPF_6 0.8 M in 1:1 EC:DEC. They were swollen in the liquid solution in glove box and their mass change was evaluated every 5 min intervals.

The obtained data are reported in Figure 5.2, in which the EUR [%] is plotted vs. time [s]. The six membranes reach a barely constant EUR value after 30 min of soaking. CPM0 shows the highest uptake rate and a plateau value of ≈125%, due to its homogeneous and dynamic structure, which allows it to take in and host a large amount of liquid. Conversely, when the nanolignin filler is added, the membrane ability to uptake liquid is a tradeoff between the positive effect of a reduced crystalline fraction and the negative effect of a limited polymer chain motion along with the decrease of free volume, already occupied by the composite particles. CPM3 is characterized by the worse behavior, with a EUR plateau value of ≈94%; CPM7 represents the best compromise with higher values; all other membranes exhibit a similar plateau value, which is intermediate between CPM0 and CPM3. CPM10 and CPM20 plots display a lower slope if compared to CPM5 and CPM7, as the higher lignin content reduces the macromolecular mobility due to the formation of intermolecular interaction and, as a result, the liquid uptake rate is reduced too.
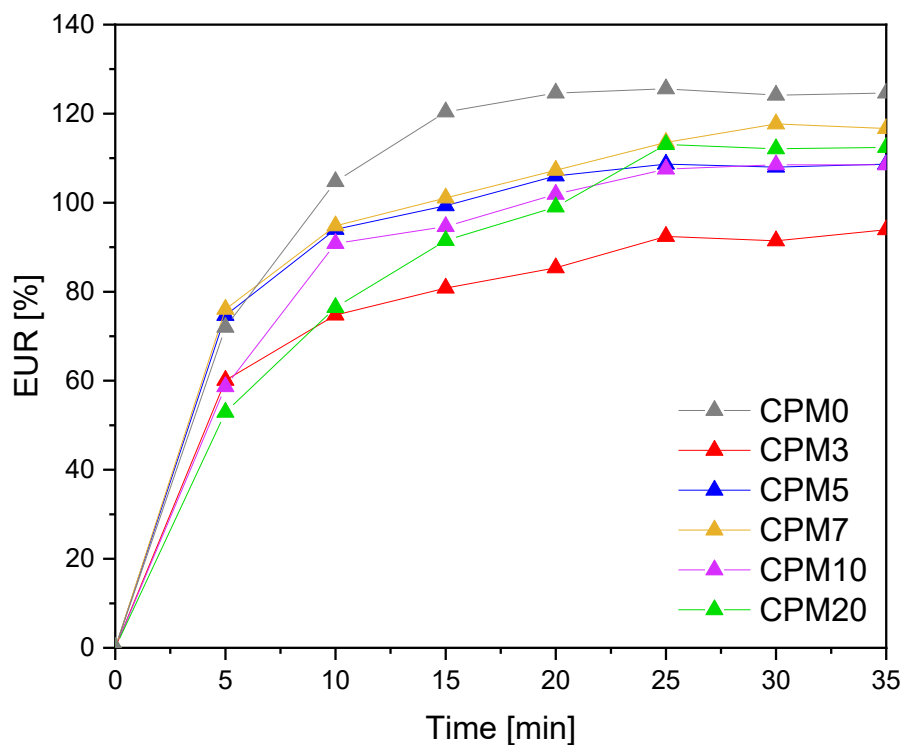
Figure 5.2: EUR vs. time comparison for the six CPMs.

5.3 Linear sweep voltammetry

The LSV tests were performed in the range between 0 and 5 V, with a scanning rate of 0.1 mV s^{-1}, and they allowed to evaluate the GCPEs stability in the cell working range (between 0.01 and 3 V) and their ESWs. The employed configuration was the EL-cell, with a potassium metal electrode, a stainless steel electrode and the GCPE; the swelling with KPF_6 0.8 M in 1:1 EC:DEC and the cell assembly were performed in glove box.

GCPE0 is stable in the whole LSV analysis range, as shown in Figure 5.3: the current is almost null in the entire investigated range. The five lignin-containing GCPEs are mostly stable in the cell working range, as shown in Figure 5.4, Figure 5.5, Figure 5.6, Figure 5.7 and Figure 5.8, but their LSV plots show a non-zero current around and below 0.5 V. GPCE5, GPCE7, GPCE10 and GPCE20 are characterized by a current peak at a voltage of ≈4.5 V: it represents the occurrence of side reactions, that could be due to the presence of lignin, as the peak is not present in GCPE0 plot.
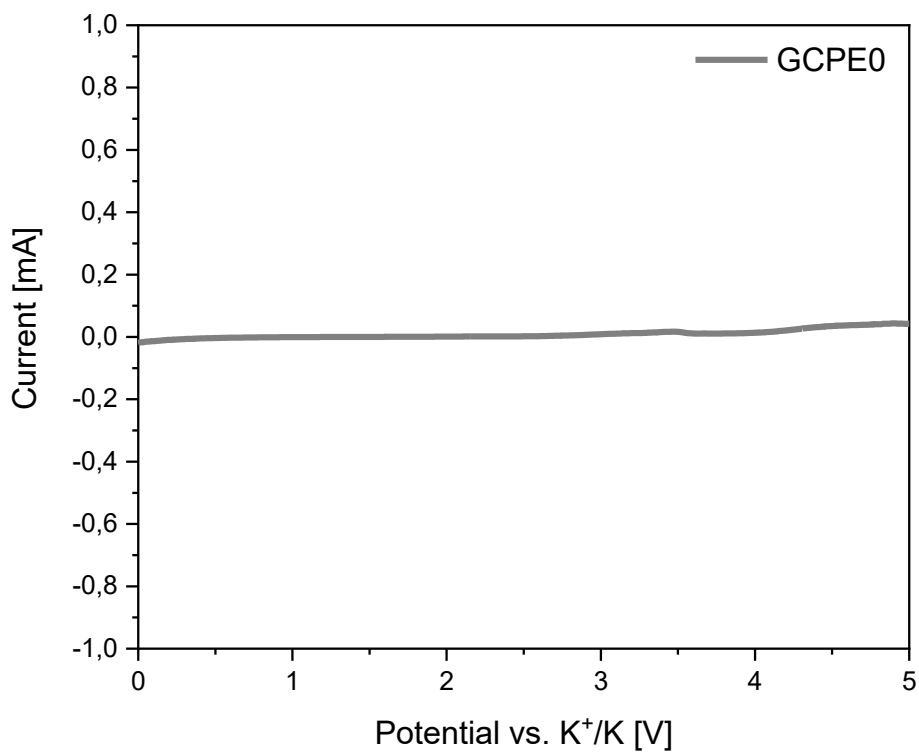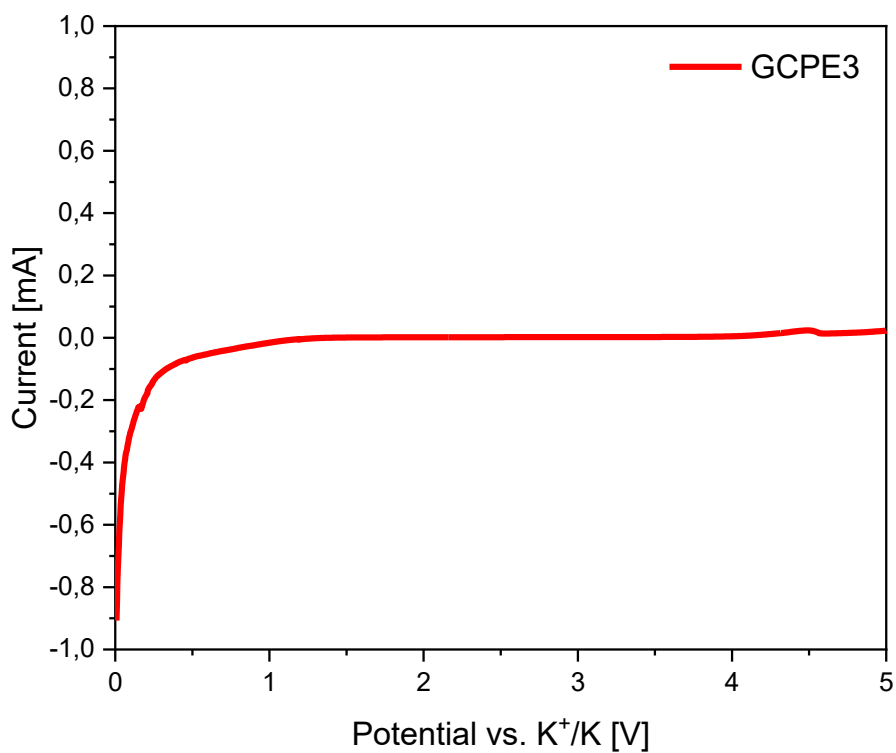
Figure 5.3: LSV voltammogram for GCPE0.

Figure 5.4: LSV voltammogram for GCPE3.
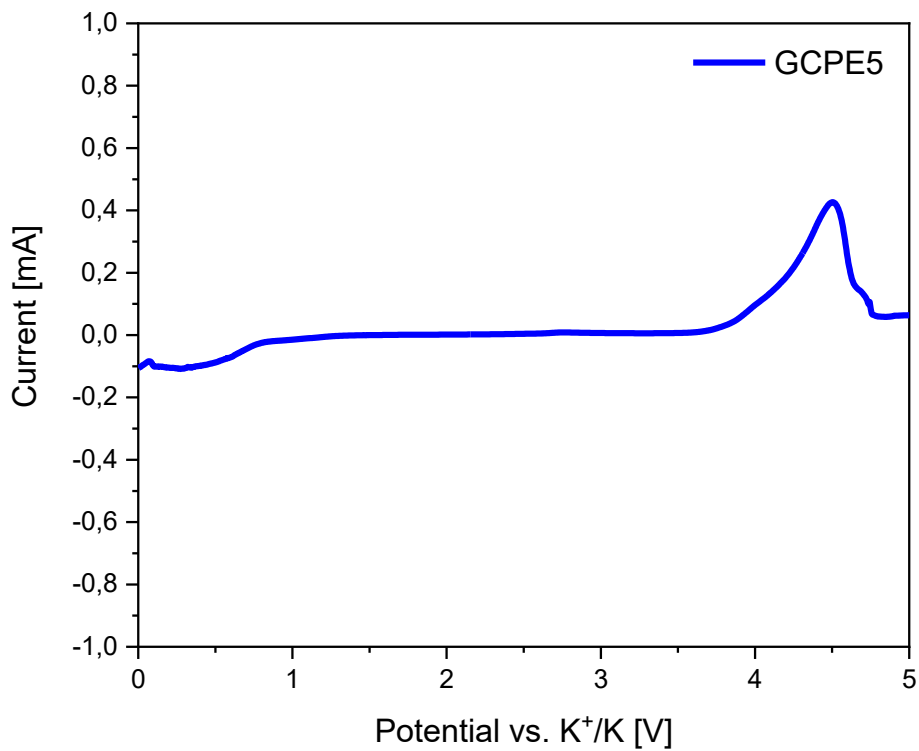
Figure 5.5: LSV voltammogram for GCPE5.
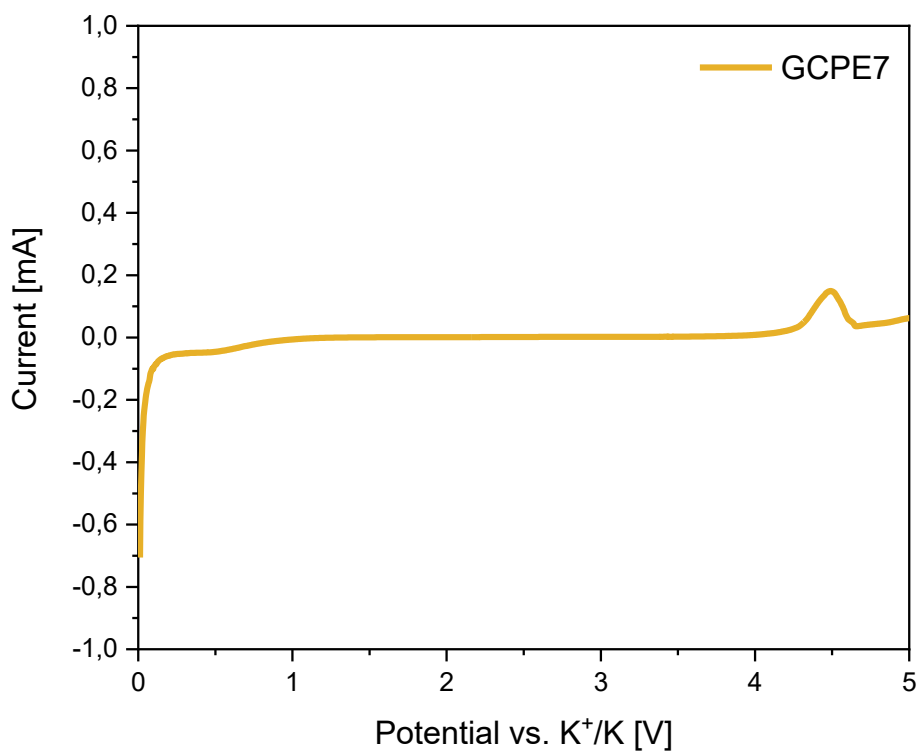
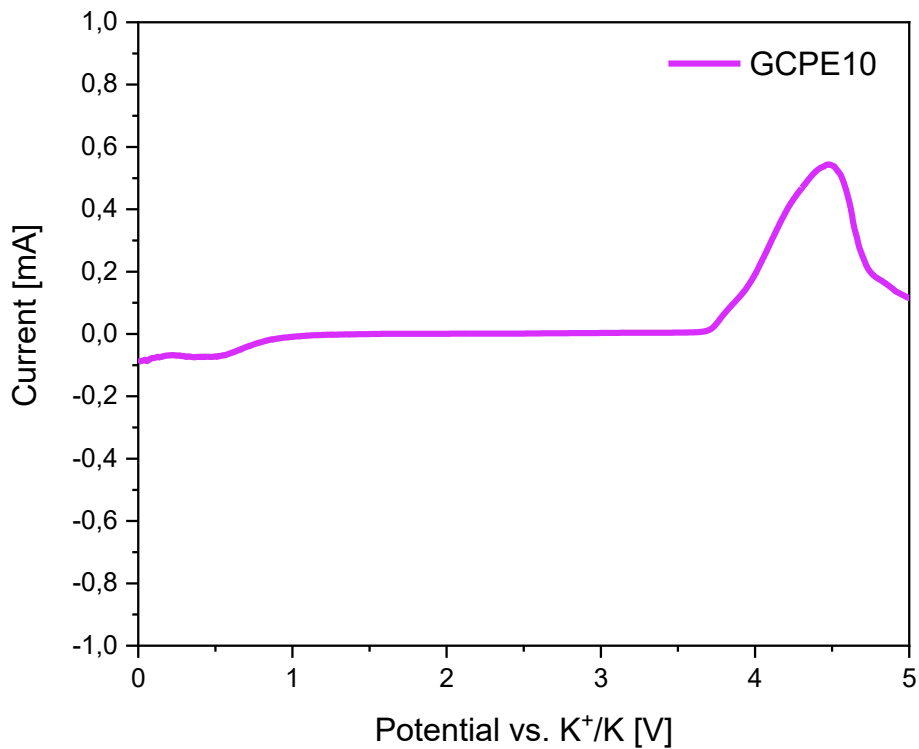**Figure 5.6**: LSV voltammogram for GCPE7.
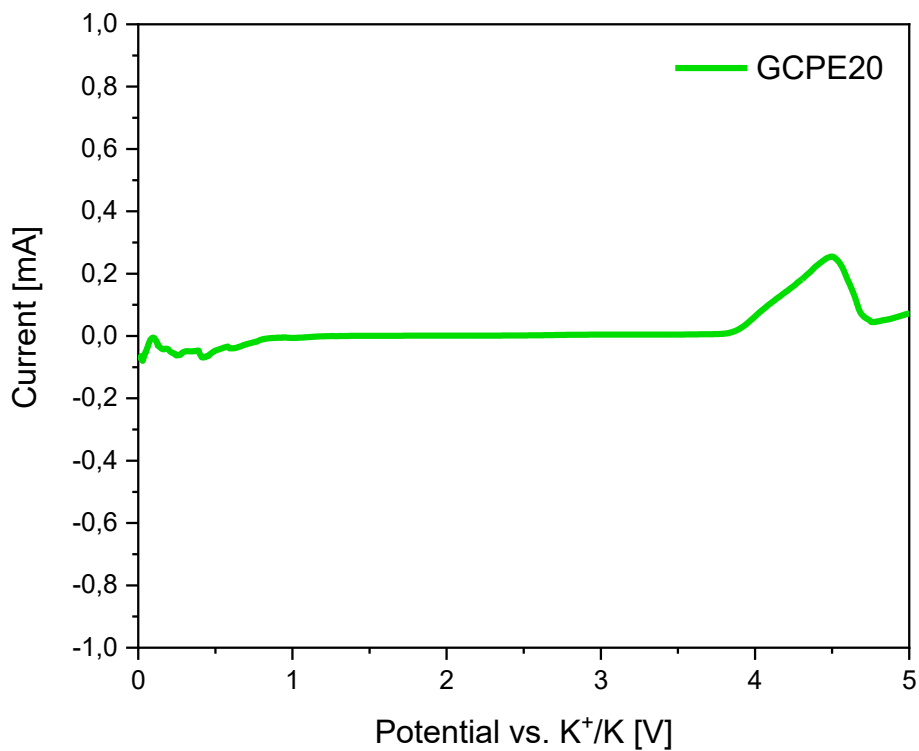
Figure 5.7: LSV voltammogram for GCPE10.

Figure 5.8: LSV voltammogram for GCPE20.

5.4 Ionic conductivity

The GCPEs ionic conductivity was evaluated as reported in paragraph 4.4.3, with the combined application of the potentiostat and the climate chamber. The electrolyte was placed between two stainless steel electrodes and the EL-cell assembly was performed in glove box. The GCPE discs were punched with a diameter of 18 mm and their thickness was measured with a micrometer at the end of the test, after the opening of the EL-cell.

The six electrolytes exhibit similar ionic conductivity trends with the temperature, as showed in Figure 5.9, in which the conductivity [S cm^{-1}] is represented vs. 1000/T [K^{-1}]. As expected, GCPE0 displays the highest conductivity in the whole temperature range, reaching the value of $1.59 \cdot 10^{-3}$ S cm^{-1} at 60 °C, thanks to its high EUR and polymer chain mobility. As a matter of fact, the worst ion conductor is represented by GCPE3, characterized by the lowest EUR; indeed, the behavior improves with the increase of the lignin content and, thus, GCPE20 reaches a conductivity value of $1.32 \cdot 10^{-3}$ S cm^{-1} at 60 °C. The increase in nanolignin concentration decreases the polymer matrix crystallinity and increases the EUR; both these variations improve the ionic conductivity, which mainly happens in the amorphous regions and in the liquid fraction.
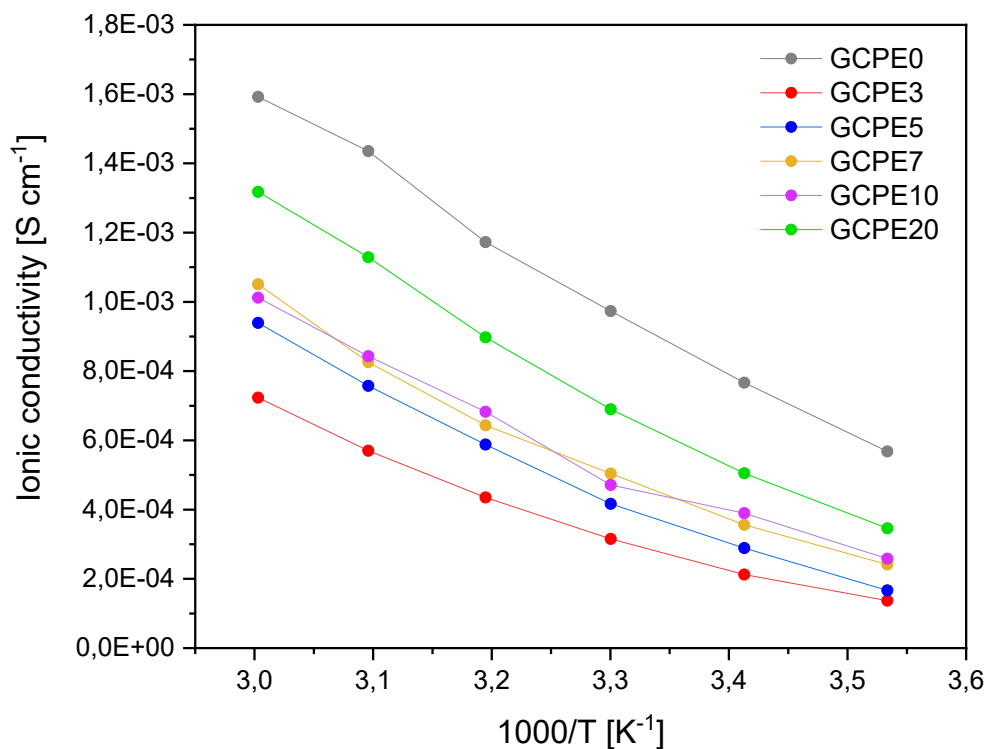

Figure 5.9: Ionic conductivity vs. 1000/T comparison for the six GCPEs.

5.5 Interfacial stability

The interfacial stability analysis was performed to evaluate the electrolyte stability toward the potassium metal electrode, considering a long period of time and maintaining the cell at its

OCV. The repeated PEIS tests were performed on the GCPEs, as described in paragraph 4.4.4; the employed configuration was the coin cell, assembled in glove box, in which the electrolyte was placed between two potassium metal discs. The GCPEs Nyquist plots are shown in Figure 5.10, Figure 5.11, Figure 5.12, Figure 5.13, Figure 5.14 and Figure 5.15. Several tests were performed on GCPE3, but the coin cells were always subject to short-circuit; this behavior could be explained by the side reactions recorded by the LSV of the GCPE3 near zero V. Indeed, being this kind of cell architecture symmetric, its OCV is always equal to zero, at which, probably, the GCPE3 is reacting with the potassium.

R_s is the curve intersection with the x-axis at high frequencies and it represents the bulk electrolyte resistance. The analyzed GCPEs show an initial slight increase in the Rs value, representing the occurrence of undesired reactions involving the liquid electrolyte; nevertheless, R_s becomes stable approximately after 20 days for all the samples.

R_{ct} can be evaluated as the semicircle curve diameter and it represents the electrode/electrolyte interface resistance. Each GCPE displays a continuous increase of the R_{ct} value over time: this trend illustrates a deterioration of the potassium metal surface, which - being very reactive - may continuously incur in redox balanced reactions at the equilibrium.

The Rs and Rct trends suggest that reactions between the potassium metal and the electrolyte occur (if so, only at the interface) and they do not take place in the electrolyte bulk.
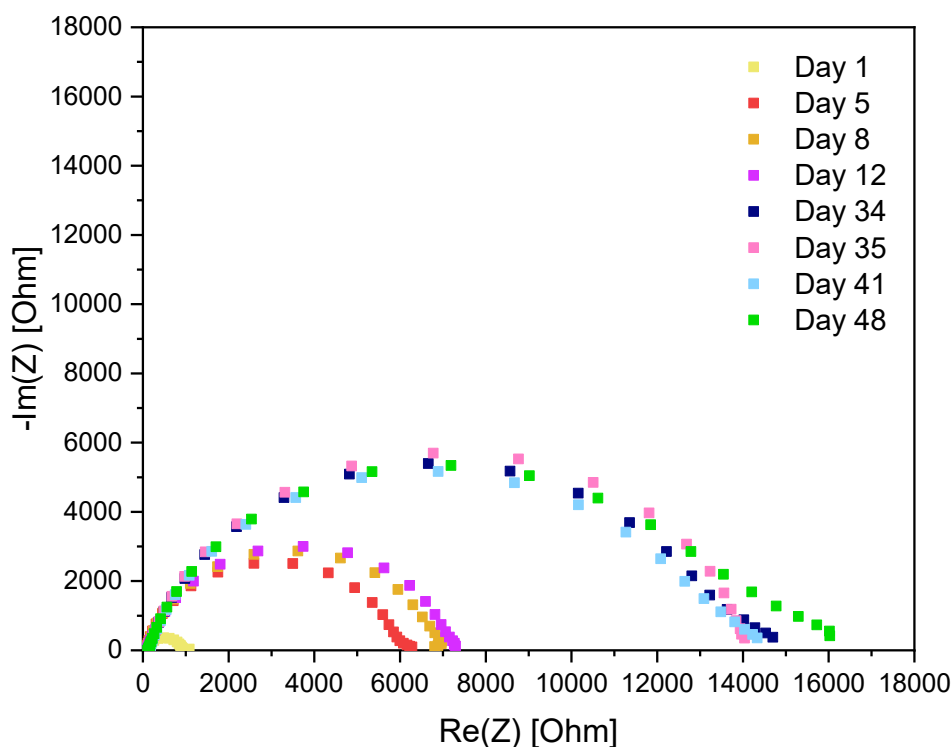
Figure 5.10: Interfacial stability Nyquist plots for GCPE0.

Figure 5.11: Interfacial stability Nyquist plots for GCPE3.
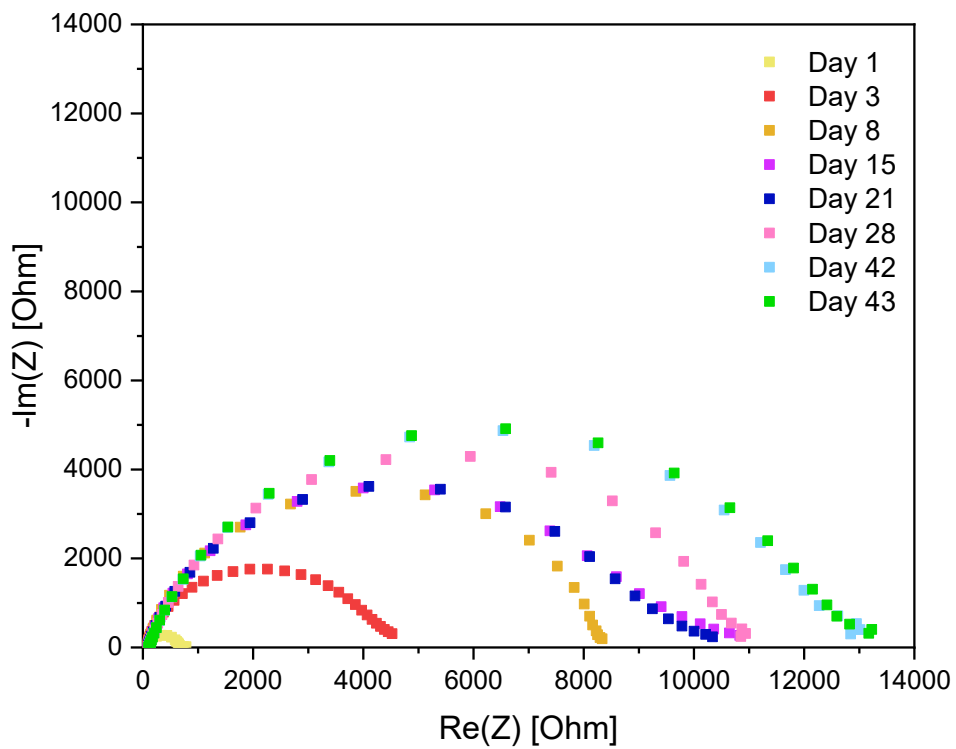
Figure 5.12: Interfacial stability Nyquist plots for GCPE5.

Figure 5.13: Interfacial stability Nyquist plots for GCPE7.

Figure 5.14: Interfacial stability Nyquist plots for GCPE10.

Figure 5.15: Interfacial stability Nyquist plots for GCPE20.

5.6 Plating and stripping

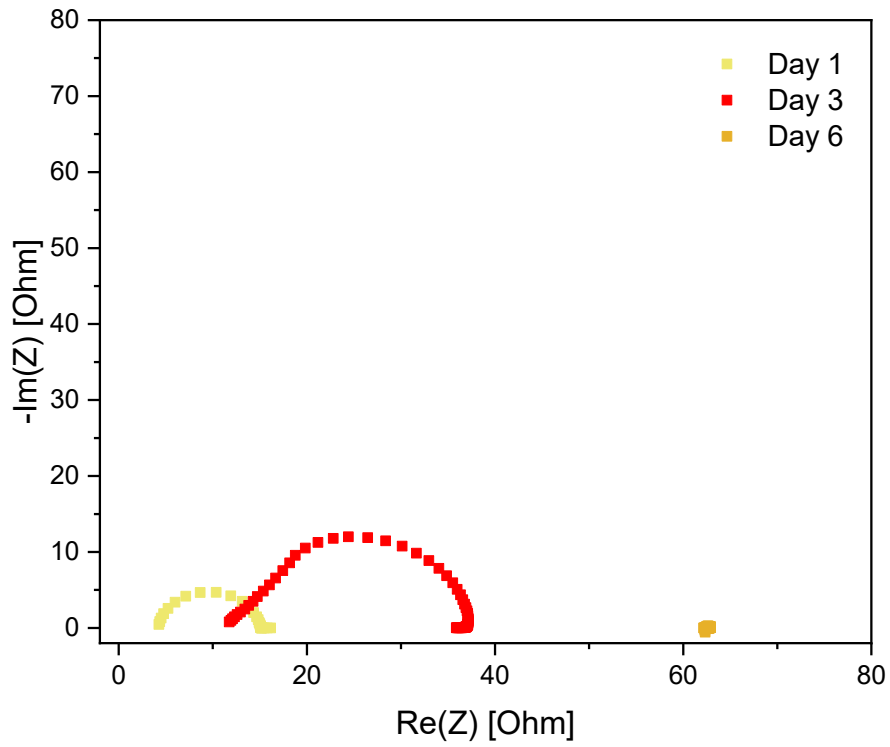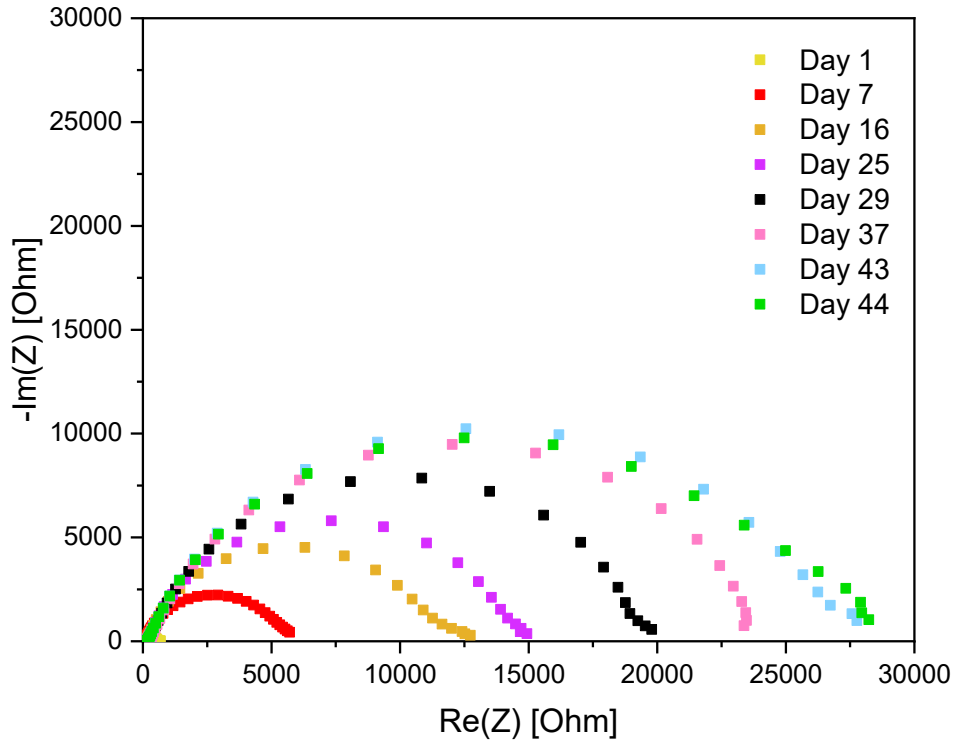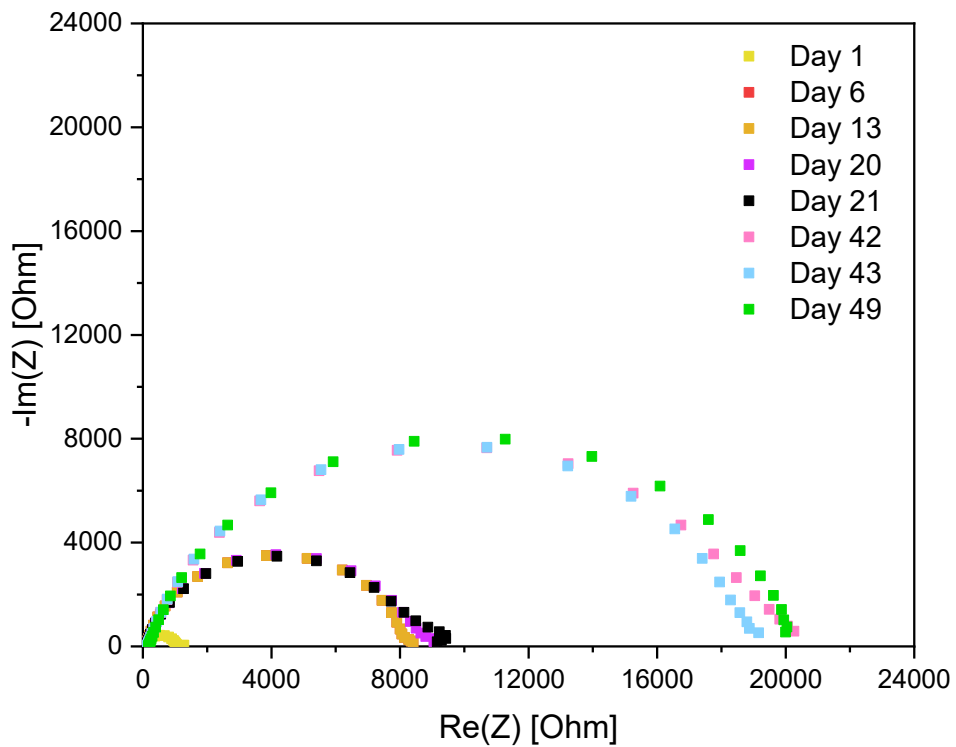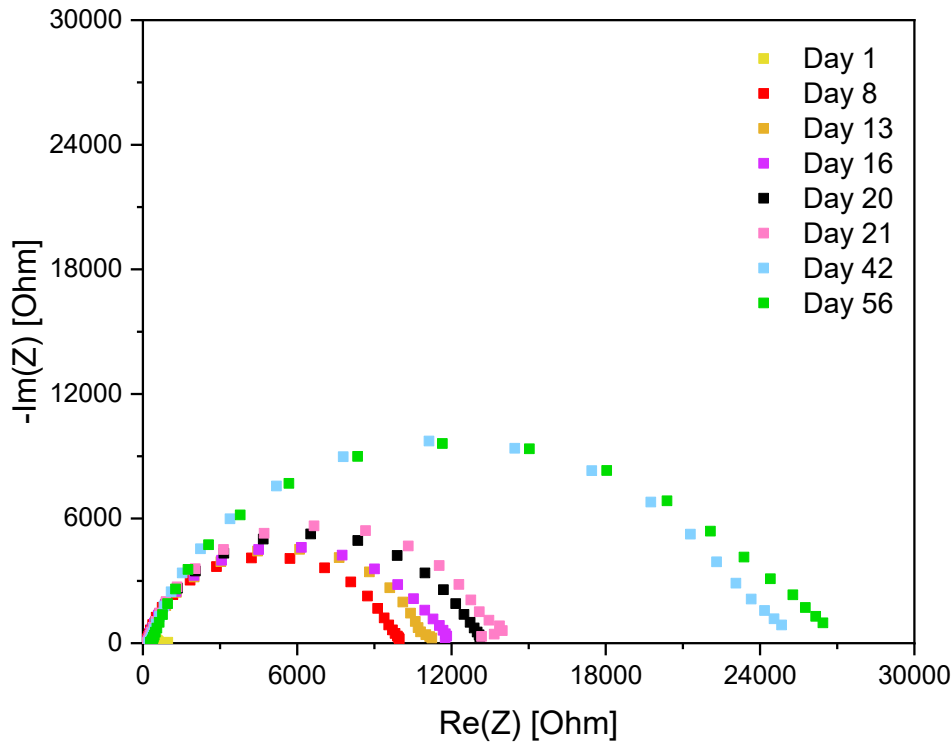The plating and stripping test allows to evaluate the electrolyte-potassium interface ability to conduct K-ions, homogenously. The method is reported in paragraph 4.4.5; the used EL-cell configuration includes the GCPE placed between two potassium metal discs and it was assembled in glove box. The plating and stripping tests were realized on GCPE7, GCPE10 and GCPE20, as they show the better overall performances, with the application of a 0.1 mA cm^{-2} current density for 70 cycles. The resulting voltage curves describe the potassium stripping and plating, when a positive and a negative current are applied, respectively.

Results of GCPE7 galvanostatic charge and discharge measurements show a moderate overpotential increase over the cycles [Figure 5.16]; the absence of peaks excludes the nucleation and growth of dendrites on the potassium metal surfaces. A PEIS was performed previously to the galvanostatic cycling and enlarged in the inset of Figure 5.17. In here, the second performed PEIS is plotted as well. Conversely to the first one, the latter results in a deformed semicircle: this shape indicates that the two electrode/electrolyte interfaces are no longer identical after the polarization, and it is confirmed by the asymmetrical plating and stripping overvoltages.

Figure 5.16: Plating and stripping test plot for GCPE7.
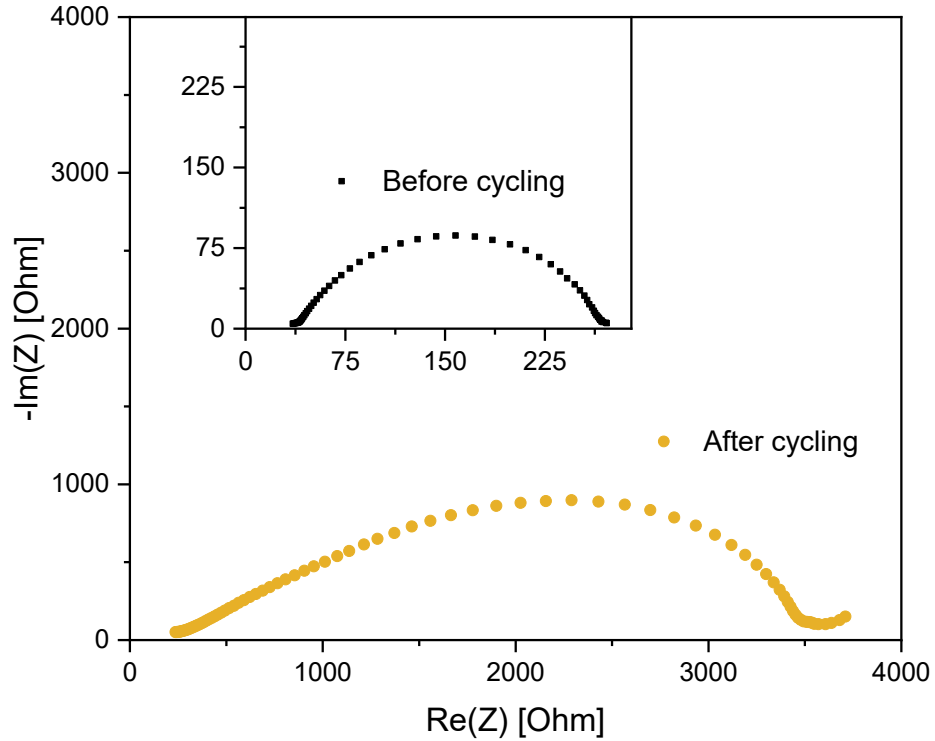
Figure 5.17: GCPE7 PEIS tests, before and after the plating and stripping test.

As shown in Figure 5.18, GCPE10 required a higher and increasing overpotential during the first cycles, followed by a sudden decrease, occurred at cycle 8: this trend could be due to the formation of an extremely thick SEI layer, which prevents ions to flow through it and reach the electrode. So, even if ions keep being conducted through the electrolyte, the thick SEI does not allow them to plate on and strip from the electrode surfaces. The rectangular shaped plot represents the absence of K^+ ions plating and stripping, and the very high R_{ct} value reached in the second PEIS measurement [Figure 5.19] confirms the high SEI layer resistance. The peaks observed between cycles 17 and 21 represent the possible nucleation of dendrites; nevertheless, they do not perforate the membrane and cause any short-circuit. This is proved by the second PEIS plot and by the overpotential values, which remain different from 0 until the end of the test.
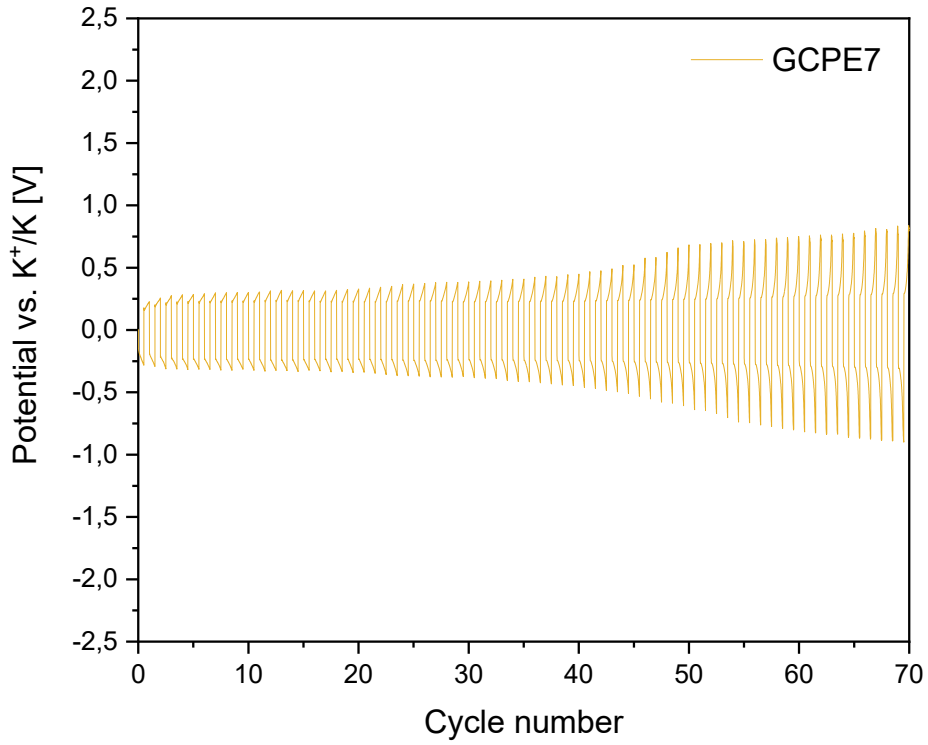

Figure 5.18: Plating and stripping test plot for GCPE10.
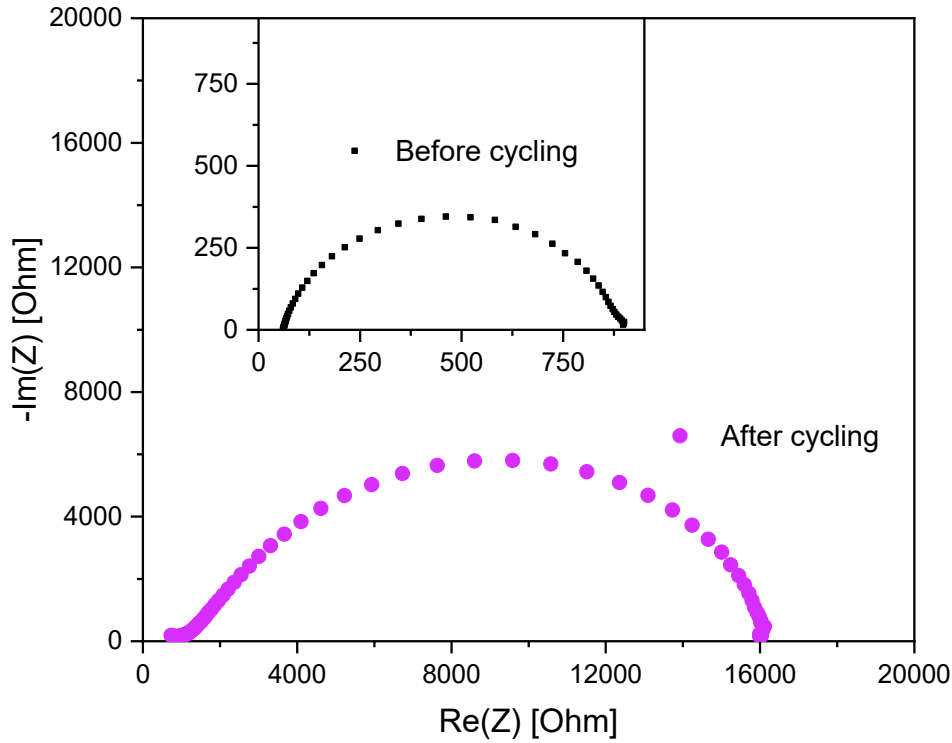
Figure 5.19: GCPE10 PEIS tests, before and after the plating and stripping test.

GPCE20 displays the best overpotential response [Figure 5.20], which is characterized by a very low initial value and by a limited increase over the whole test; therefore, the two SEI layers are homogeneous and stable and they assure an excellent ions conduction. This is confirmed by the second PEIS measurement, which shows a low R_{ct} value [Figure 5.21]. The almost symmetric plating and stripping plot indicates that the two electrolyte/electrode interfaces are almost identical. Such good performing interfaces can guarantee a long and safe from short-circuit cycling, as proven in the following paragraph.
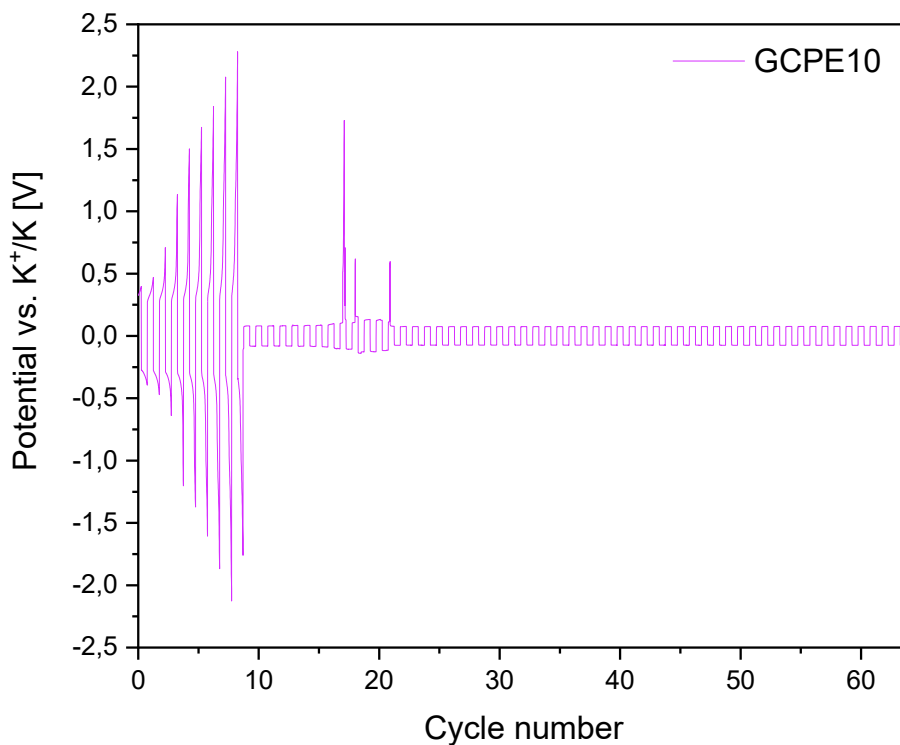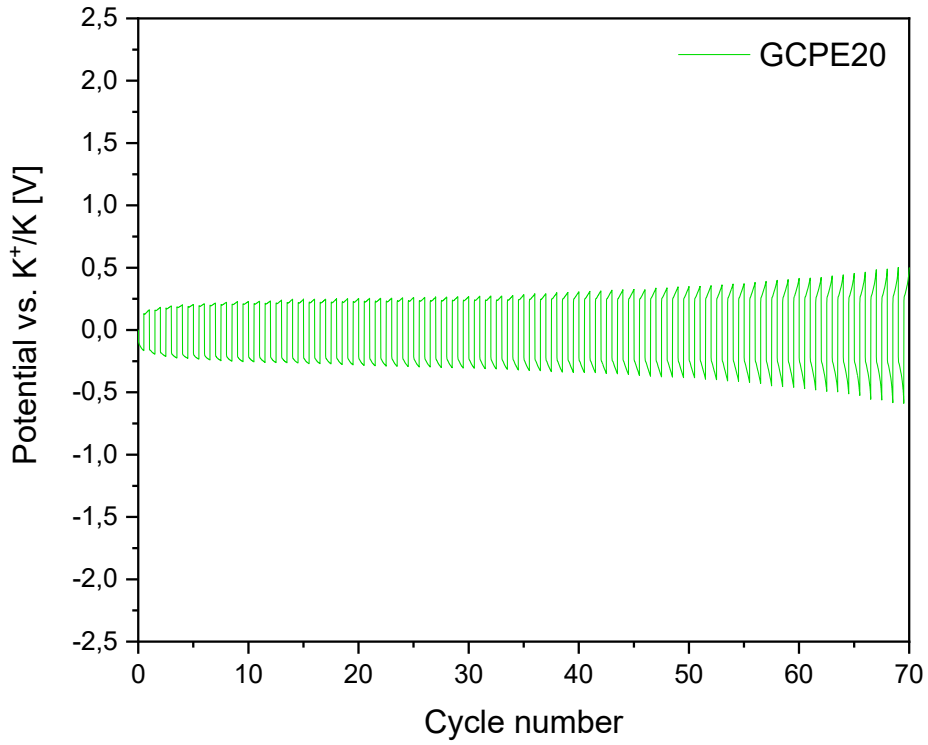
Figure 5.20: Plating and stripping test plot for GCPE20.
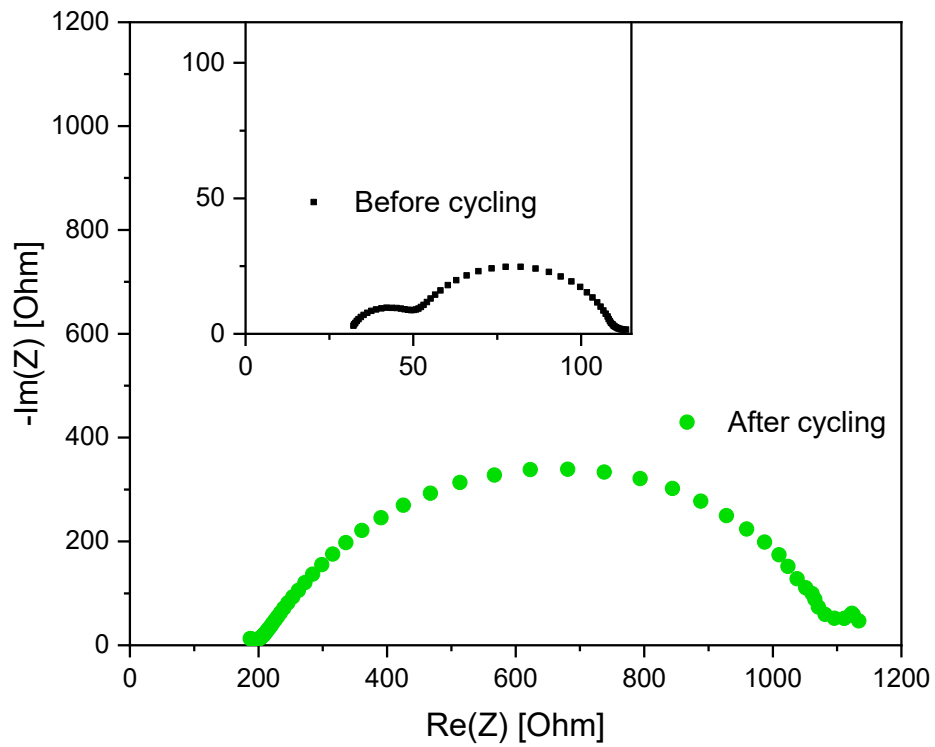
Figure 5.21: GCPE20 PEIS tests, before and after the plating and stripping test.

5.7 Galvanostatic cycling

The galvanostatic cycling is usually performed as the electrochemical characterization conclusive test. The employed coin cells were assembled in glove box and sealed with the crimper; they were composed of a Super P carbon cathode, a potassium metal anode and the GCPE. The charge/discharge tests were performed for many cycles, as described in paragraph 4.4.6. A specific current of ±0.05 A g^{-1} was applied for the first 10 cycles, then it was increased up to ±0.1 A g^{-1} and maintained constant.

The GCPEs show a high decrease in the specific capacities during the first $\approx$10 cycles: this behavior is always exhibited if Super P carbon is used as electrode. The irreversible capacity is due to the very high Super P superficial area that reacts to form the SEI. GCPE0 displays irregular plots of the charge and discharge capacities [Figure 5.22] and this behavior could be due to its poor mechanical properties: as a consequence, it does not adequately withstand the electrode volume changes and the ions flow through its structure. This hypothesis was further supported by the occurrence of short-circuit after $\approx$600 cycles.
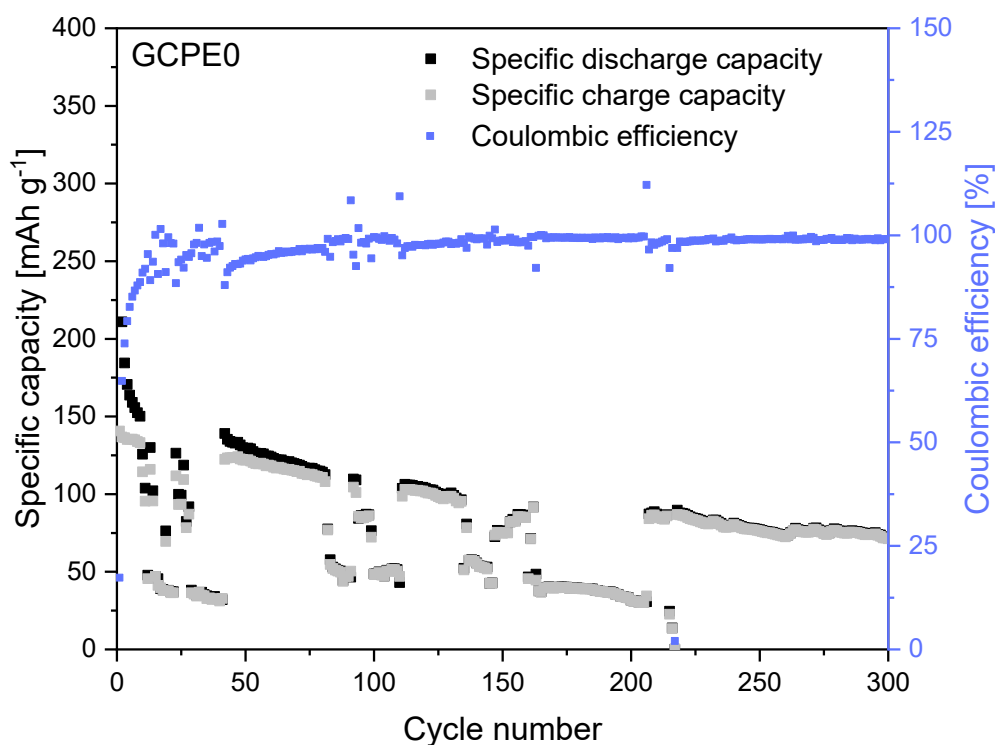
Figure 5.22: Specific charge and discharge capacities and Coulombic efficiency vs. cycle number for GCPE0.

The charge and discharge specific capacities exhibit an initial irregular trend for GCPE3, GCPE5 and GCPE7, while they stabilize after $\approx$50 cycles, when also the Coulombic efficiency reaches the constant and optimal value of $\approx$99-100% [Figure 5.23, Figure 5.24, Figure 5.25]. The previous fluctuations could be due to the relatively poor GCPEs mechanical properties, which are subsequently counterbalanced by the formation of stable SEI layers. GCPE3 and

GCPE5 display low values of charge and discharge specific capacities over the whole test, with low retentions at cycle 300 (*i.e.*, 33% for GCPE3 and 13% for GCPE5). The latter were evaluated considering the specific charge capacities of the first stable cycle and of the 300th. GCPE7 exhibits high specific capacity values, but unfortunately it was subject to short-circuit at cycle 160.

Figure 5.23 Specific charge and discharge capacities and Coulombic efficiency vs. cycle number for GCPE3.

Figure 5.24 Specific charge and discharge capacities and Coulombic efficiency vs. cycle number for GCPE5.
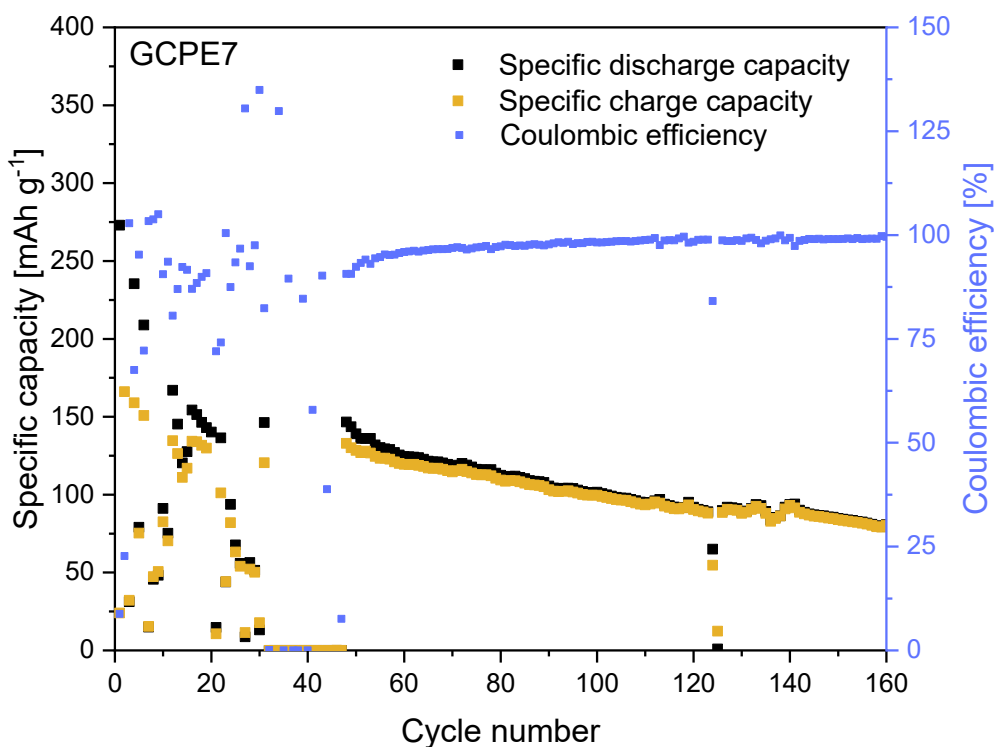
Figure 5.25: Specific charge and discharge capacities and Coulombic efficiency vs. cycle number for GCPE7.

GCPE10 and GCPE20 display the best performances [Figure 5.26, Figure 5.27], due to the high lignin content, which improves the membranes mechanical properties, the ionic conductivity and the SEI layers stability. The specific capacity trend becomes stable at the 25th cycle for GCPE10; the cell shows relatively high capacity values and the highest retention at the 300th cycle (*i.e.*, 53%). GCPE20 displays a lower retention after 300 cycles (*i.e.,* 44%), but it reaches the highest specific capacity values and it exhibits an excellent stability since the very first cycles. Optimal Coulombic efficiency values are shown by both cells (≈100%).

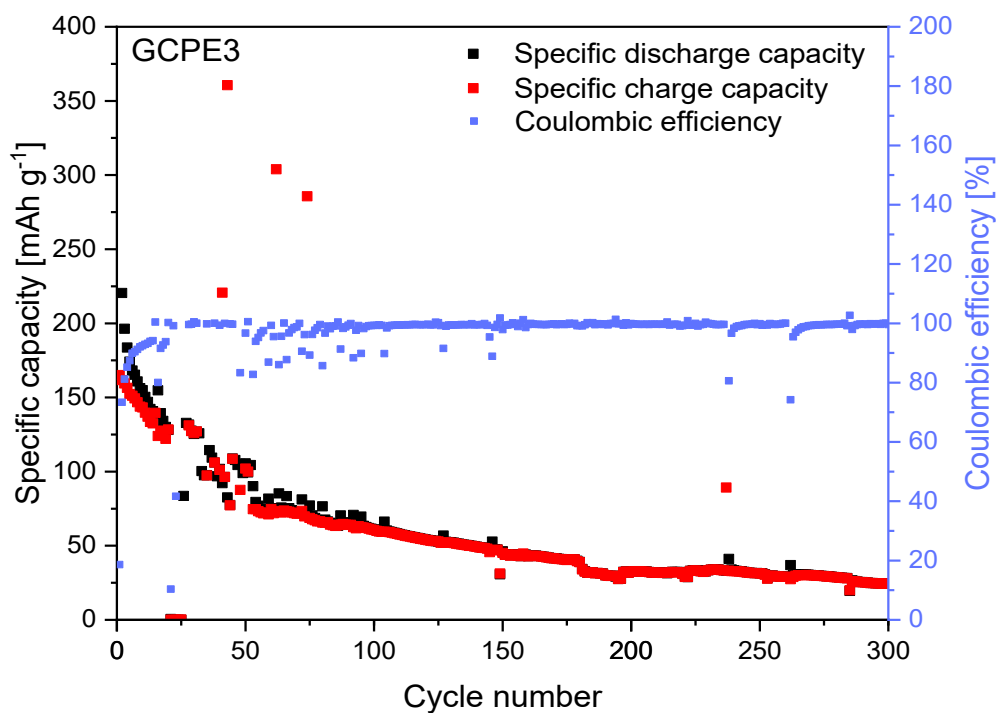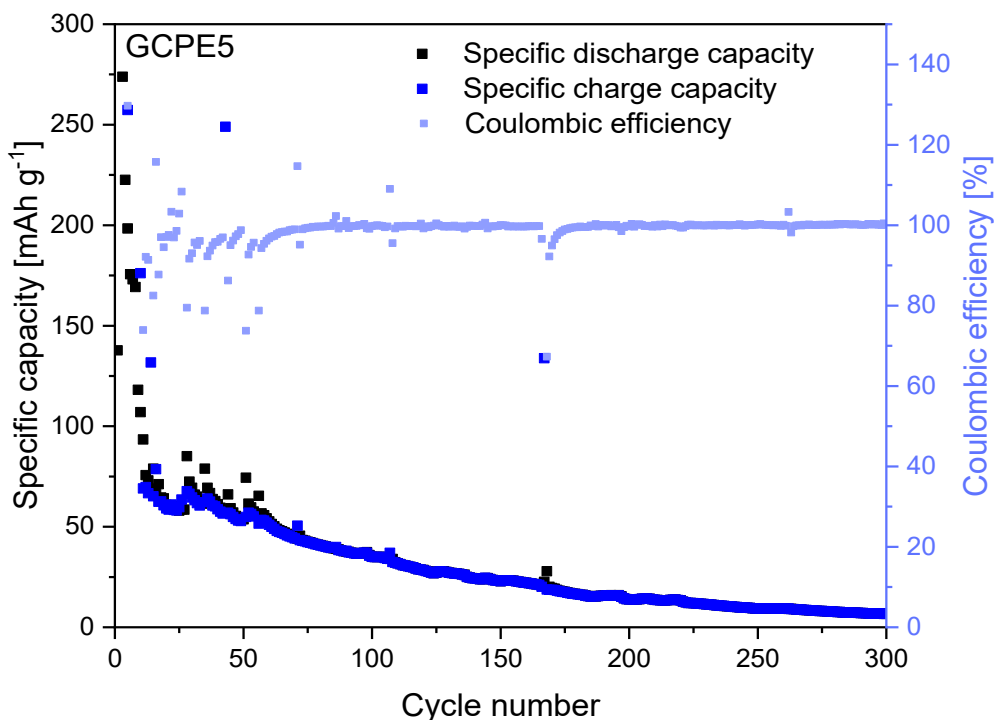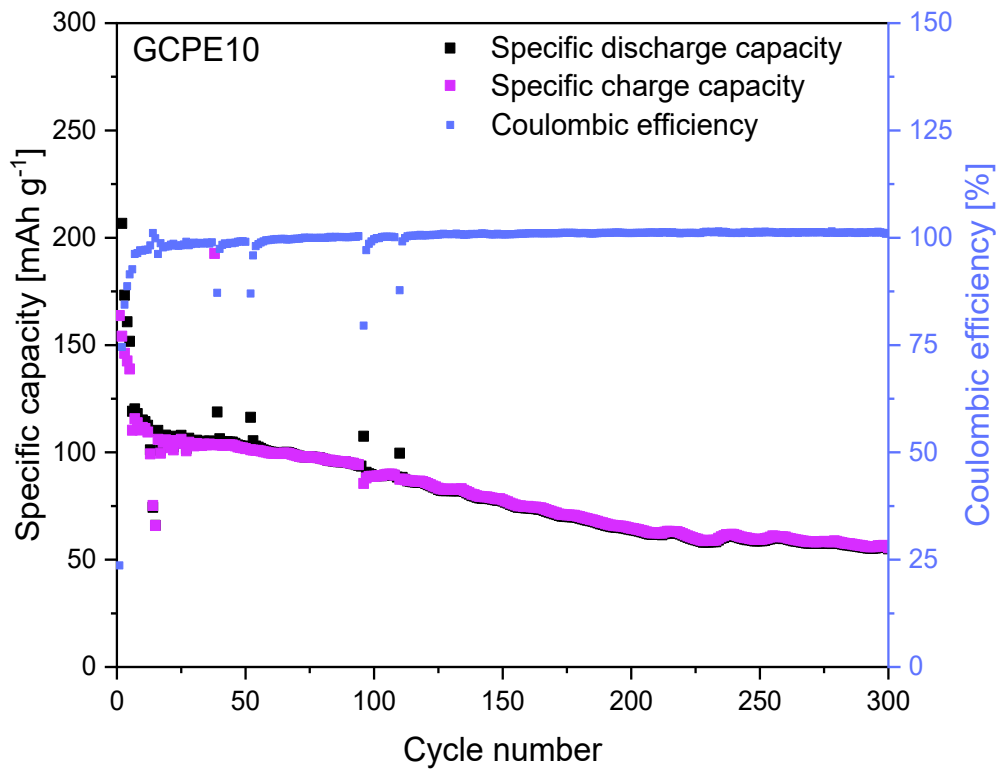**Figure 5.26**: Specific charge and discharge capacities and Coulombic efficiency vs. cycle number for GCPE10.
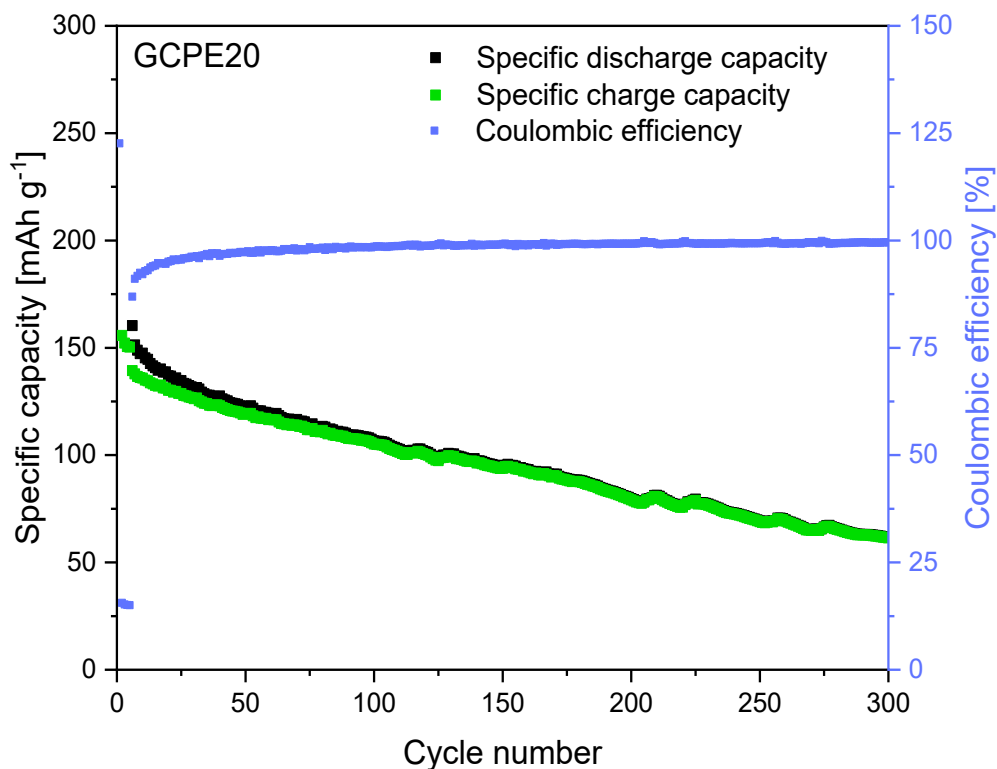
Figure 5.27: Specific charge and discharge capacities and Coulombic efficiency vs. cycle number for GCPE20.

Table 5.2 displays - for each GCPE - the first stable cycle and its specific charge capacity, the specific charge capacity of the 300th cycle and the relative capacity retention.

Table 5.2: GCPEs capacity retention data.

Acronym	First stable cycle	Specific charge capacity of the first stable cycle [mAh g^{-1}]	Specific charge capacity of the 300th cycle [mAh g^{-1}]	Capacity retention at the 300th cycle [%]
GCPE3	51	74.61	24.52	≈33
GCPE5	57	53.41	6.64	≈13
GCPE7	52	127.96	(80.38 at cycle 160)	(≈63 at cycle 160)
GCPE10	28	104.66	55.57	≈53
GCPE20	6	139.36	61.41	≈44

GPCE10 was further analyzed through galvanostatic cycling, in order to evaluate its self-healing properties. The EL-cell configuration, including a potassium metal anode, the electrolyte and a Super P carbon cathode, was assembled in glove box. The cell was connected to the Arbin cycler and 10 charge/discharge cycles were performed with a specific current density of ± 0.05 A g^{-1}; then, it was brought again in the glove box and, thanks to the chosen configuration, it was possible to open it and to subsequently perform a small cut on the membrane [Figure 5.28]. The cell was then reclosed and reconnected to the cycler, where the same specific current was applied.
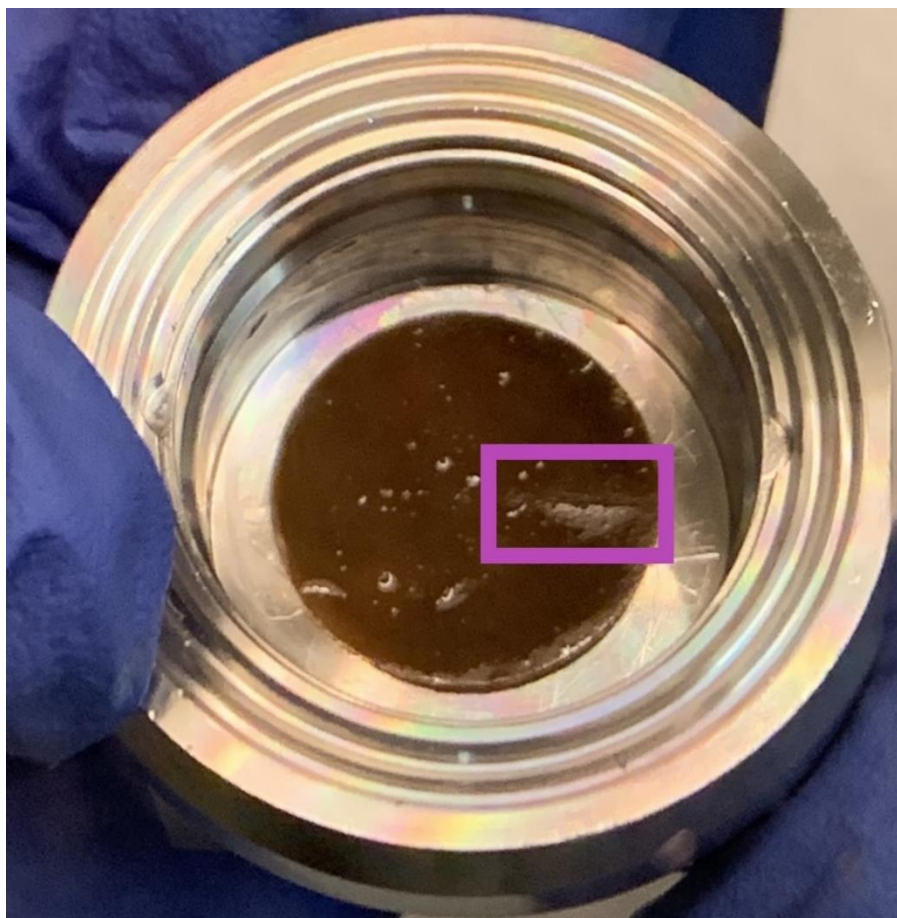
Figure 5.28: Picture of the cut performed on GCPE10, after the EL-cell opening.

The specific charge and discharge capacities over the cycles are displayed in Figure 5.29. A net specific capacity decrease is reported between cycle 10 and 11, corresponding to the cell opening and to the cutting. Despite the damage, the cell did not experience any short-circuit; the occurrence of the latter would not have surprised, as the ions preferentially move through the pathways characterized by a lower resistance, such as the cut area. A feasible hypothesis concerns the UPy-MA self-healing ability: the formation of multiple hydrogen bonds could have reduced the damage extent and partially restored the membrane stability.
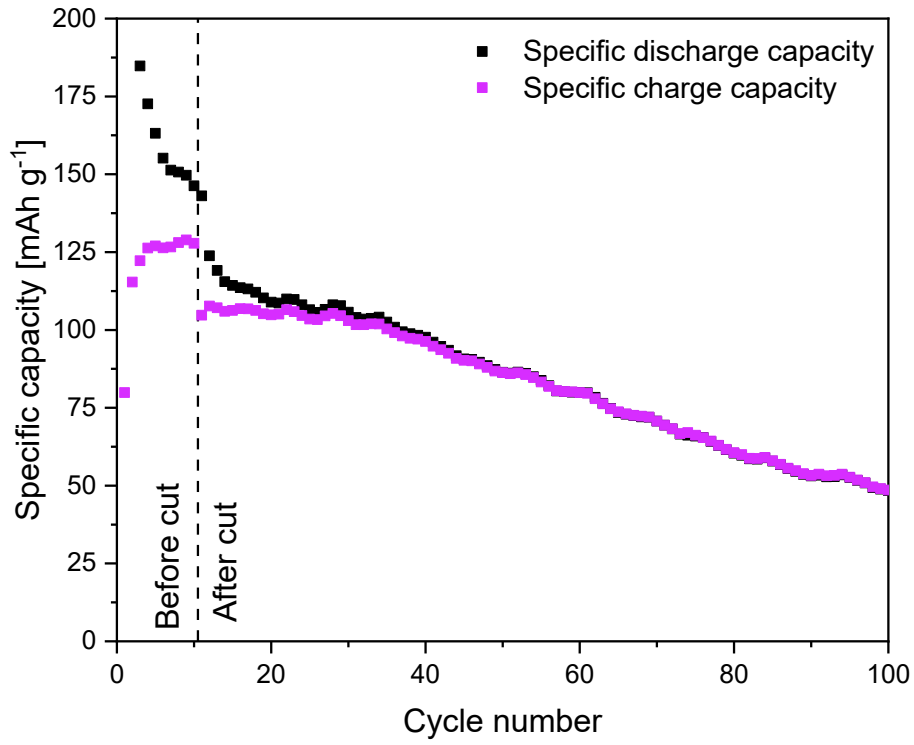
Figure 5.29: Specific charge and discharge capacities vs. cycle number for GCPE10 – SH test.

6 Conclusions

In this thesis work, some novel lignin-based gel-composite polymer electrolytes were analyzed and tested in potassium-ion batteries, using the coin cell and the EL-cell configurations.

The electrolytes are initially in the form of composite polymer membranes, which are subsequently swollen in the organic liquid electrolyte KPF_6 0.8 M in 1:1 EC:DEC, obtaining the gel form. The membranes matrix consists of cross-linked and interpenetrated polymer chains, with a fixed composition of polycaprolactone di-methacrylate (PCLDMA), polyethylene glycol (PEG) and ureido-pyrimidinone methacrylate (UPy-MA). Bretax nanolignin is present in the matrix as organic filler: it is a lignosulfonate, obtained from biomass through the sulfite extraction process, and its dimensions are reduced to nanoscale by ultrasonication. The membranes lignin concentration is varied among the values of 0, 3, 5, 7, 10, 20% by weight, referred to the mass of PCLDMA.

The interest towards these novel electrolytes arises from their several positive aspects: the quasi-solid state, which increases the battery safety; the gel form, that improves the solid electrolyte flexibility and the contact with the electrode surfaces; the filler presence, which allows to obtain better mechanical properties, lower crystallinity and higher ionic conductivity; the lignin low cost and bio-derivation, which improves the battery recyclability and its eco-friendliness. Furthermore, the polymer UPy-MA provides self-healing properties, through the formation of multiple hydrogen bonds in the membrane damaged areas.

As analyzed by differential scanning calorimetry, the increase in the amount of lignin causes a decrease in the polymer chains mobility and determines an increase in the glass transition temperature; at the same time, the degree of crystallinity is decreased, and with it the crystallization enthalpy. As a result, there is an increase in the amount of liquid electrolyte that the membrane is able to absorb.

The electrochemical tests are performed on the GCPEs and they include linear sweep voltammetry, interfacial stability tests, ionic conductivity measurements, plating and stripping tests, galvanostatic cycling and self-healing tests. A metal potassium anode and a Super P carbon cathode were used for the galvanostatic cycling.

The linear sweep voltammetry tests demonstrate that the GCPEs are mostly stable in the working potential range (between 0.01 and 3 V), with a slight variation around 0.5 V. The ionic conductivity, obtained through electrochemical impedance spectroscopy measurements, increases with the increase in the nanolignin content, as it decreases the matrix crystallinity and increases the EUR; GCPE20 reaches a value of $1.32 \cdot 10^{-3}$ S cm^{-1} at the temperature of 60 °C. The plating and stripping tests allowed to evaluate the stability of the SEI layer; the best results were obtained with GCPE20, and they suggest the formation of a homogeneous, conductive and stable SEI layer. As a matter of fact, the galvanostatic cycling shows an increase in cycling stability, specific capacity values and capacity retention as the amount of nanolignin increases. The charge/discharge performances of the five GCPEs are shown in Figure 6.1, in which the specific charge capacity of each is reported vs. the number of cycles. Galvanostatic cycling was further employed to evaluate GCPE10 self-healing properties. Despite the intentionally performed damage, the cell did not undergo any short-circuit: a feasible hypothesis concerns

the UPy-MA self-healing ability, with the formation of multiple hydrogen bonds that could have reduced the damage extent and partially restored the membrane stability.
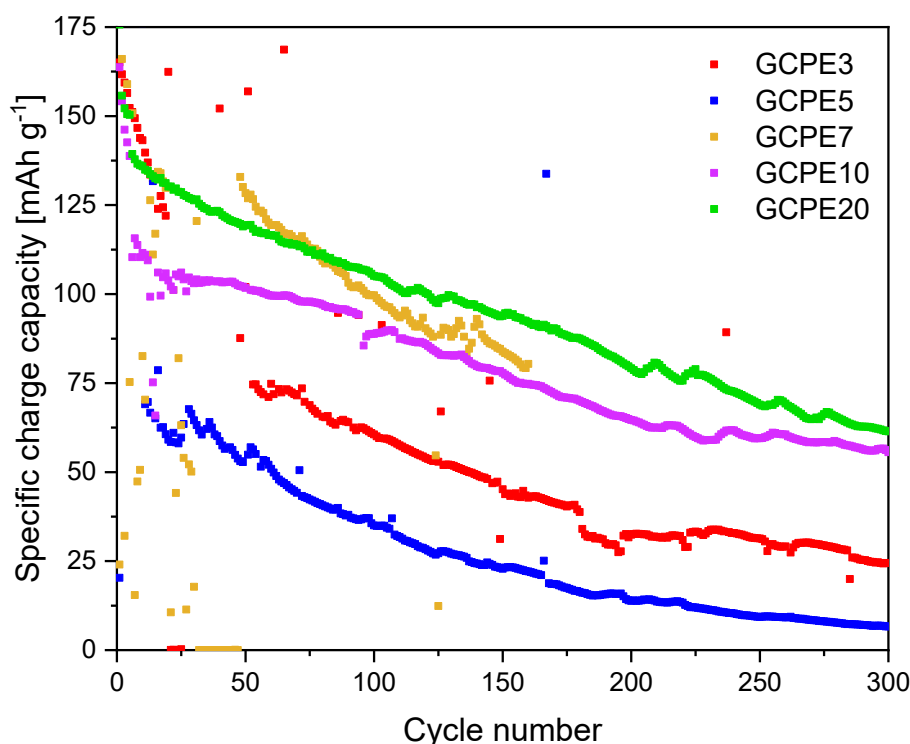
Figure 6.1: Specific charge capacity vs. cycle number comparison for the five GCPEs.

To conclude, considering the general GCPEs properties improvement as the nanolignin content is increased, the analysis of membranes with higher filler concentrations will allow to identify the value that determines the maximum performances. In this perspective, it is necessary to improve the membrane production techniques, as the increase in the lignin concentration worsens the components mixing and dissolution, the cross-linking and the membrane laying. However, a maximum nanolignin amount will surely be identified, beyond which the cross-linking would be hindered and that would cause excessive membrane rigidity and fragility.

Bibliography

[1] (2022), [Online]. Available: https://www.epa.gov/ghgemissions/global-greenhouse-gas-emissions-data (accessed: 10/01/2022).

[2] (2022), [Online]. Available: https://gml.noaa.gov/ccgg/trends/data.html (accessed: 10/01/2022).

[3] (2022) [Online]. Available: https://www.climate.gov/ (accessed: 10/01/2022).

[4] (2022) [Online] Available: https://climate.nasa.gov/effects/ (accessed: 10/01/2022).

[5] (2022) [Online] Available: https://ec.europa.eu/info/strategy/priorities-2019-2024/european-green-deal_en (accessed: 10/01/2022).

[6] R. Amirante, E. Cassone, E. Distaso, P. Tamburrano, Overview on recent developments in energy storage: mechanical, electrochemical and hydrogen technologies, *Energy Conversion and Management*, **132** (2017) 372–387.

[7] E. Reihani, S. Sepasi, L. R. Roose, M. Matsuura, Energy management at the distribution grid using a battery energy storage system (BESS), *International Journal of Electrical Power & Energy Systems* **77** (2016) 337–344.

[8] S. Loznen, C. Bolintineanu, J. Swart, *Electrical Product Compliance and Safety Engineering*. Artech House, 2017.

[9] H. Berg, *Batteries for Electric Vehicles - Materials and Electrochemistry*. Cambridge University Press, 2015.

[10] G. Zubi, R. Dufo-López, M. Carvalho, G. Pasaoglu, The lithium-ion battery: state of the art and future perspectives, *Renewable and Sustainable Energy Reviews* **89** (2018) 292–308.

[11] Y. Miao, L. Liu, Y. Zhang, Q. Tan, J. Li, An overview of global power lithium-ion batteries and associated critical metal recycling, *Journal of Hazardous Materials* **425** (2022) 127900.

[12] V. Anoopkumar, J. Bibin, T.D. Mercy, Potassium-ion batteries: key to future large-scale energy storage?, *ACS Applied Energy Materials* **3** (2020) 9478–9492.

[13] Y. Chen, Y. Kang, Y. Zhao, L. Wang, J. Liu, Y. Li, Z. Liang, X. He, X. Li, N. Tavajohi, B. Li, A review of lithium-ion battery safety concerns: the issues, strategies, and testing standards, *Journal of Energy Chemistry* **59** (2021) 83–99.

[14] R. Borah, F. Hughson, J. Johnston, T. Nann, On battery materials and methods, *Materials Today Advances* **6** (2020) 100046.

[15] W. Zhang, J. Yin, W. Wang, Z. Bayhan, H. N. Alshareef, Status of rechargeable potassium batteries, *Nano Energy* **83** (2021) 105792.

[16] A. Eftekhari, Potassium secondary cell based on Prussian blue cathode, *Journal of Power Sources* **126** (2004) 221–228.

[17] R. Rajagopalan, Y. Tang, X. Ji, C. Jia, H. Wang, Advancements and challenges in potassium ion batteries: a comprehensive review, *Advanced Functional Materials* **30** (2020) 1909486.

[18] S. Komaba, T. Hasegawa, M. Dahbi, K. Kubota, Potassium intercalation into graphite to realize high-voltage/high-power potassium-ion batteries and potassium-ion capacitors, *Electrochemistry Communications* **60** (2015) 172–175.

[19] Z. Jian, W. Luo, X. Ji, Carbon electrodes for K-ion batteries, *Journal of the American Chemical Society* **137** (2015) 11566–11569.

[20] X. Zhang, J. Meng, X. Wang, Z. Xiao, P. Wu, L. Mai, Comprehensive insights into electrolytes and solid electrolyte interfaces in potassium-ion batteries, *Energy Storage Materials* **38** (2021) 30–49.

[21] J. Hwang, S. Myung, Y. Sun, Recent progress in rechargeable potassium batteries, *Advanced functional materials* **28** (2018) 1802938.

[22] X. Wu, Y. Chen, Z. Xing, C. W. K. Lam, S. Pang, W. Zhang, Z. Ju, Advanced carbon-based anodes for potassium-ion batteries, *Advanced Energy Materials* **9** (2019) 1900343.

[23] J. C. Pramudita, D. Sehrawat, D. Goonetilleke, N. Sharma, An initial review of the status of electrode materials for potassium-ion batteries, *Advanced Energy Materials* **7** (2017) 1602911.

[24] X. Min, J. Xiao, M. Fang, W. Wang, Y. Zhao, Y. Liu, A. M. Abdelkader, K. Xi, R. V. Kumar, Z. Huang, Potassium-ion batteries: outlook on present and future technologies, *Energy & Environmental Science* **14** (2021) 2186.

[25] S. M. Ahmed, G. Suo, W. A. Wang, K. Xi, S. B. Iqbal, Improvement in potassium ion batteries electrodes: recent developments and efficient approaches, *Journal of Energy Chemistry* **62** (2021) 307–337.

[26] B. Wang, E. H. Ang, Y. Yang, Y. Zhang, M. Ye, Q. Liu, C. C. Li, Post-Lithium Ion Battery Era: Recent Advances in Rechargeable Potassium-Ion Batteries, *Chemistry : a European Journal* **27** (2021) 512-536.

[27] X. Zhang, Z. Wei, K. N. Dinh, N. Chen, G. Chen, F. Du, Q. Yan, Layered oxide cathode for potassium-ion battery: recent progress and prospective, *Small* **16** (2020) 2002700.

[28] Y. Xu, S. Guo, X. Tao, Y. Sun, J. Ma, C. Liu, A. Cao, High-performance cathode materials for potassium-ion batteries: structural design and electrochemical properties, *Advanced Materials* **33** (2021) 2100409.

[29] S. Liu, L. Kang, S. C. Jun, Challenges and Strategies toward Cathode Materials for Rechargeable Potassium-Ion Batteries, *Advanced Materials* **33** (2021) 2004689.

[30] C. Zhang, Y. Xu, M. Zhou, L. Liang, H. Dong, M. Wu, Y. Yang, Y. Lei, Potassium Prussian Blue Nanoparticles: A Low-Cost Cathode Material for Potassium-Ion Batteries, *Advanced Functional Materials* **27** (2017) 1604307.

[31] R. Verma, P. Didwal, J. Hwang, C. Park, Recent progress in electrolyte development and design strategies for next-generation potassium-ion batteries, *Batteries & Supercaps* **4** (2021) 1-24.

[32] M. Zhou, P. Bai, X. Ji, J. Yang, C. Wang, Y. Xu, Electrolytes and interphases in potassium ion batteries, *Advanced Materials* **33** (2021) 2003741.

[33] X. Bie, K. Kubota, T. Hosaka, K. Chiharab, S. Komaba, A novel K-ion battery: hexacyanoferrate(II)/graphite cell, *Journal of Materials Chemistry A* **5** (2017) 4325.

[34] D. Zhou, D. Shanmukaraj, A. Tkacheva, M. Armand, G. Wang, Polymer electrolytes for lithium-based batteries: advances and prospects, *Chem* **5** (2019) 2326-2352.

[35] D. Fenton, J. Parker, P. Wright, Complexes of alkali metal ions with poly(ethylene oxide), *Polymer* **14** (1973) 589.

[36] G. Feuillade, P. Perche, Ion-conductive macromolecular gels and membranes for solid lithium cells, *Journal of Applied Electrochemistry* **5** (1975) 63–69.

[37] S. Skaarup, K. West, B. Zachau-Christiansen, Mixed phase solid electrolytes, *Solid State Ionics* **28–30** (1988) 975-978.

[38] W. Wieczorek, K. Such, H. Wyciślik, J. Płocharski, Modifications of crystalline structure of PEO polymer electrolytes with ceramic additives, *Solid State Ionics* **36** (1989) 255-257.

[39] F. Wu, K. Zhang, Y. Liu, H. Gao, Y. Bai, X. Wang, C. Wu, Polymer electrolytes and interfaces toward solid-state batteries: Recent advances and prospects, *Energy Storage Materials* **33** (2020) 26-54.

[40] M. Dirican, C. Yan, P. Zhu, X. Zhang, Composite solid electrolytes for all-solid-state lithium batteries, *Materials Science & Engineering* **136** (2019) 27–46.

[41] C. Angell, C. Liu, E. Sanchez, Rubbery solid electrolytes with dominant cationic transport and high ambient conductivity, *Nature* **362** (1993) 137–139.

[42] A. Arya1, A. Sharma, Polymer electrolytes for lithium ion batteries: a critical study, *Ionics* **23** (2017) 497–540.

[43] W. Li, Y. Wu, J. Wang, D. Huang, L. Chen, G. Yang, Hybrid gel polymer electrolyte fabricated by electrospinning technology for polymer lithium-ion battery, *European Polymer Journal* **67** (2015) 365-372.

[44] P. Kuo, C. Wu, C. Lu, C. Tsao, C. Hsu, S. Hou, High performance of transferring lithium ion for polyacrylonitrile-interpenetrating crosslinked polyoxyethylene network as gel polymer electrolyte, *ACS Applied Materials & Interfaces* **6** (2014) 3156-3162.

[45] S. Sharma, D. Pathak, N. Dhiman, R. Kumar, M. Kumar, FTIR, thermal and ionic conductivity studies of nanocomposite polymer electrolytes. *Surface Innovations* **7** (2019) 51–58.

[46] M. Zhu, J. Wu, Y. Wang, M. Song, L. Long, S. Siyal , X. Yang , G. Sui, Recent advances in gel polymer electrolyte for high-performance lithium batteries, *Journal of energy chemistry* **37** (2019) 126-142.

[47] E. Lizundia, D. Kundu, Advances in natural biopolymer-based electrolytes and separators for battery applications, *Advanced Functional Materials* **31** (2020).

[48] N. Boaretto, L. Meabe, M. Martinez-Ibañez, M. Armand, H. Zhang, Polymer Electrolytes for Rechargeable Batteries: From Nanocomposite to Nanohybrid, *Journal of The Electrochemical Society* **167** (2020) 070524.

[49] D. Kai, M. Tan1, P. Chee1, Y. Chua, Y. Yap, X. Loh, Towards lignin-based functional materials in a sustainable world, *Green Chemistry* **18** (2016) 1175-1200.

[50] C. Chioa, M. Sainb, W. Qina, Lignin utilization: A review of lignin depolymerization from various aspects, *Renewable and Sustainable Energy Reviews* **107** (2019) 232–249.

[51] F. Vásquez-Garay, I. Carrillo-Varela, C. Vidal, P. Reyes-Contreras, M. Faccini, R. Mendonça, A Review on the Lignin Biopolymer and Its Integration in the Elaboration of Sustainable Materials, *Sustainability* **13** (2021) 2697.

[52] M. Baloch, J. Labidi, Lignin biopolymer: the material of choice for advanced lithium-based batteries, *RSC Advances* **11** (2021) 23644–23653.

[53] S. Gong, Y. Huang, H. Cao, Y. Lin, Y. Li, S. Tang, M. Wang, X. Li, A green and environment-friendly gel polymer electrolyte with higher performances based on the natural matrix of lignin, *Journal of Power Sources* **307** (2016) 624-633.

[54] B. Liu, Y. Huang, H. Cao, A. Song, Y. Lin, M. Wang, X. Li, A high-performance and environment-friendly gel polymer electrolyte for lithium ion battery based on composited lignin membrane, *Journal of Solid State Electrochemistry* **22** (2018) 807–816.

[55] D. Chen, D. Wang, Y. Yang, Q. Huang, S. Zhu, Z. Zheng, Self-Healing Materials for Next-Generation Energy Harvesting and Storage Devices, *Advanced Energy Materials* **7** (2017) 1700890.

[56] W. Mai, Q. Yu, C. Han, F. Kang, B. Li, Self-Healing Materials for Energy-Storage Devices, *Advanced Energy Materials* **30** (2020) 1909912.

[57] B. Zhou, D. He, J. Hu, Y. Ye, H. Peng, X. Zhou, X. Xie, Z. Xue, A flexible, self-healing and highly stretchable polymer electrolyte via quadruple hydrogen bonding for lithium-ion batteries, *Journal of Materials Chemistry A* **6** (2018) 11725-11733.

[58] R. Suriano, L. Brambilla, M. Tommasini, S. Turri, A deep insight into the intrinsic healing mechanism in ureido pyrimidinone copolymers, *Polymers for Advanced Technologies* **29** (2018) 2899-2908.

[59] H. Wang, D. Zhai, F. Kang, Solid electrolyte interphase (SEI) in potassium ion batteries, *Energy & Environmental Science* **13** (2020) 4583-4608.

[60] M. Moshkovich, Y. Gofer, D. Aurbach, Investigation of the electrochemical windows of aprotic alkali metal (Li, Na, K) salt solutions, *Journal of The Electrochemical Society* **148** (2001) E155–E167.

[61] L. Zhou, Z. Cao, W. Wahyudi, J. Zhang, J. Hwang, Y. Cheng, L. Wang, L. Cavallo, T. Anthopoulos, Y. Sun, Electrolyte engineering enables high stability and capacity alloying anodes for sodium and potassium ion batteries, *ACS Energy Letters* **5** (2020) 766–776.

[62] Y. Chao, Molybdenum Disulfide/Carbon Composites for Lithium Ion Batteries, Doctor of Philosophy thesis, Intelligent Polymer Research Institute, University of Wollongong, 2020.

[63] (2022) [Online]. Available: https://el-cell.com/products/test-cells/standard-test-cells/ecc-std/#1488984333852-c659124b-90a6 (accessed: 15/02/2022).

[64] (2022) [Online]. Available: https://www.gamry.com/application-notes/EIS/basics-of-electrochemical-impedance-spectroscopy/ (accessed: 16/02/2022).